Wind Speed and Direction Changes due to Terrain Effects Revealed by Climatological Data from two Sites in Jutland

Hedegaard, K.; Larsen, Søren Ejling

Publication date:
1983

Document Version
Publisher's PDF, also known as Version of record

Risø-R-434

RISØ

Risø-R-434

Wind Speed and Direction Changes due to Terrain Effects revealed by Climatological Data from two Sites in Jutland

Klaus Hedegaard and Søren E. Larsen

Risø National Laboratory, DK-4000 Roskilde, Denmark

May 1983

RISØ-R-434

WIND SPEED AND DIRECTION CHANGES DUE TO TERRAIN EFFECTS REVEALED BY CLIMATOLOGICAL DATA FROM TWO SITES IN JUTLAND

Klaus Hedegaard[+] and Søren E. Larsen
Meteorology Section, Physics Department

Abstract. The report discusses the influence of inhomogeneous surface conditions on meteorological data from two neighbouring sites in Jutland.

The difference in the averages of the wind speed at the two stations is attributed to dissimilarities in roughness in the area and is described by the use of similarity laws for the neutral planetary boundary layers and for the neutral surface boundary layer.

(Continue on next page)

[+] Danish Meteorological Institute
Lyngbyvej 100, DK-2100 Copenhagen Ø.

May 1983
Risø National Laboratory, DK 4000 Roskilde, Denmark

In contrast, the difference in the averages of the wind direction is attributed to both momentum balance requirements with changing topographical height, and the differential heating and/or cooling within the area.

INIS-descriptors: BOUNDARY LAYERS; CLIMATES; DENMARK; GROUND LEVEL; METEOROLOGY; REACTOR SITES; ROUGHNESS; VELOCITY; WIND

UDC 551.55

ISBN 87-550-0861-5
ISSN 0106-2840

Risø Repro 1983

CONTENTS

Page

1. INTRODUCTION

In the late fall of 1974 two automatic meteorological stations were installed in the Horsens fjord region in Jutland. The stations were separated by 10 km, the one at the island of Alrø, the other at the Gylling Næs peninsula.

The data-gathering project was directed by the Meteorology Section of Risø National Laboratory and financed by one of the Danish electricity boards, ELSAM. The primary purpose of the measurements was to obtain dispersion meteorological statistics for the area as it was considered a possible site for a nuclear power plant.

During the analysis of the data we discovered striking differences between the data from the two stations, when they were discriminated against wind direction. We therefore decided to look further into possible causes of these differences in the climatology of the wind. Our data derive from the period November 74 to May 76, and the basic data analysis was carried out shortly after.

It is our hope that the results of this report can find use in more comprehensive treatments of terrain inhomogeneities. We anticipate that it will illustrate the need for detailed wind forecasts for special purposes, and especially, the need for very careful consideration of terrain, instrumentation etc. when a wind-measuring network is established.

2. SITES AND DATA RECORDS

2.1. Description of area and sites

In Fig. 2.1 a map is shown of the Horsens fjord area. The fjord has an irregular shape, especially on its northern side. This, together with several islands in the fjord make a simple geometrical description of the area impossible. The land bounding it

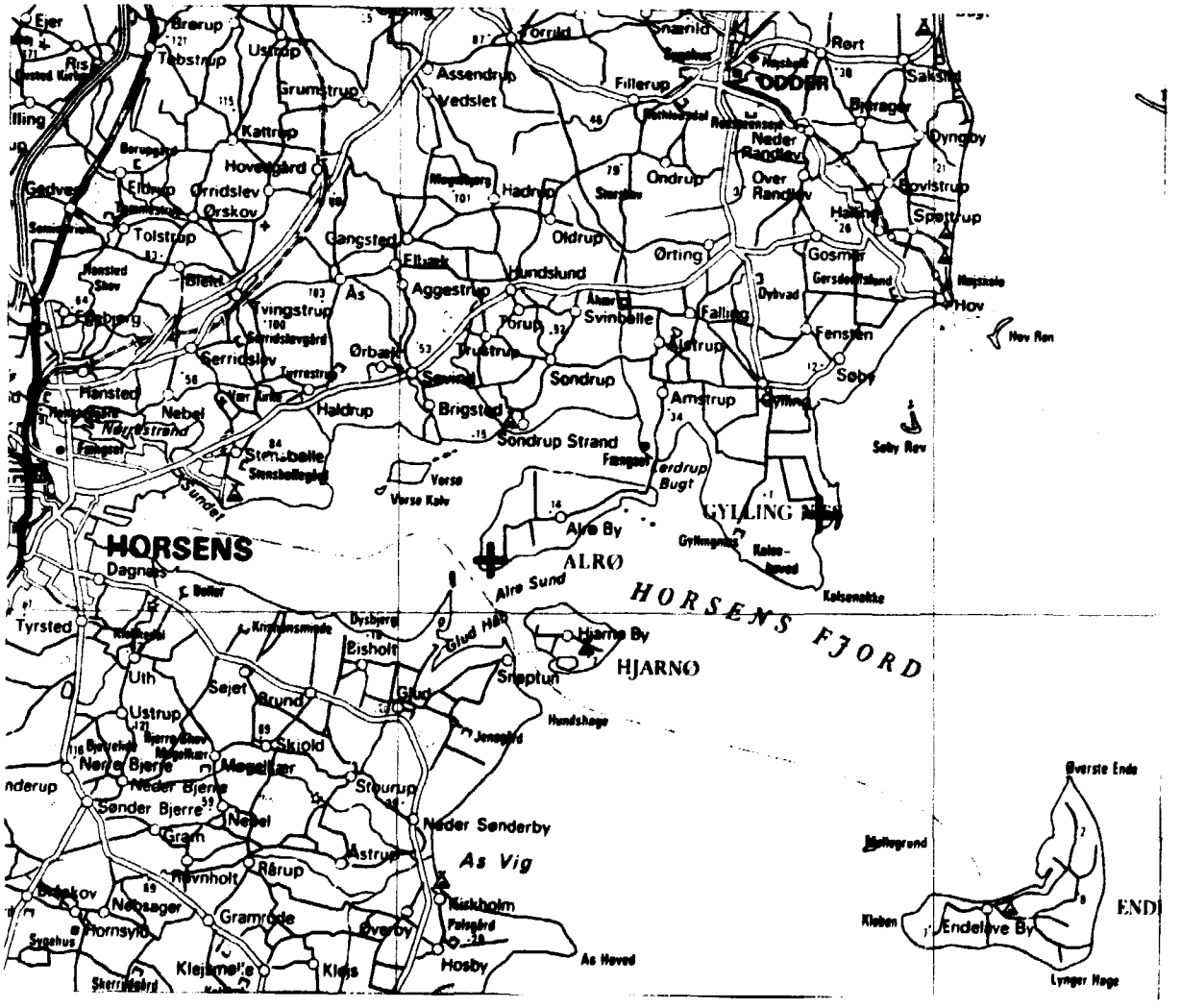

Fig. 2.1. Map of the Horsens Fjord area in the scale 1:200.000. The two stations are marked with crosses.

is a combination of farmland and woods, with the former predominant; altitudes above mean sea level range up to some 80 m.

More detailed maps of the immediate surroundings to the two sites appear in Fig. 2.2.a and b.

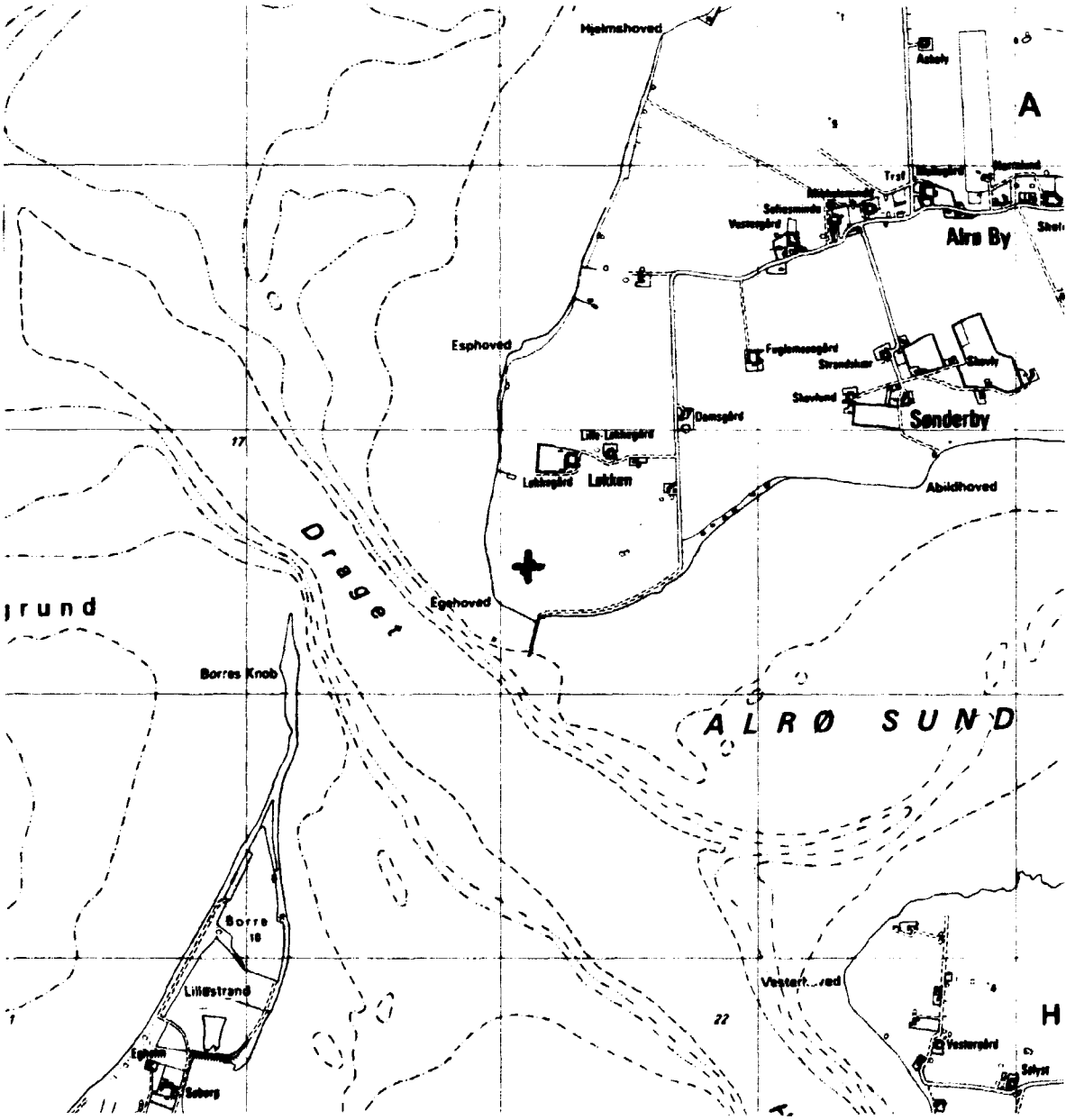

Fig. 2.2.a-b. Maps of the surroundings to the stations in the scale 1:25.000. The stations are marked with crosses. Isolines for height above mean sea level are separated by 2.5 m.
a) Alrø, b) Gylling Næs.

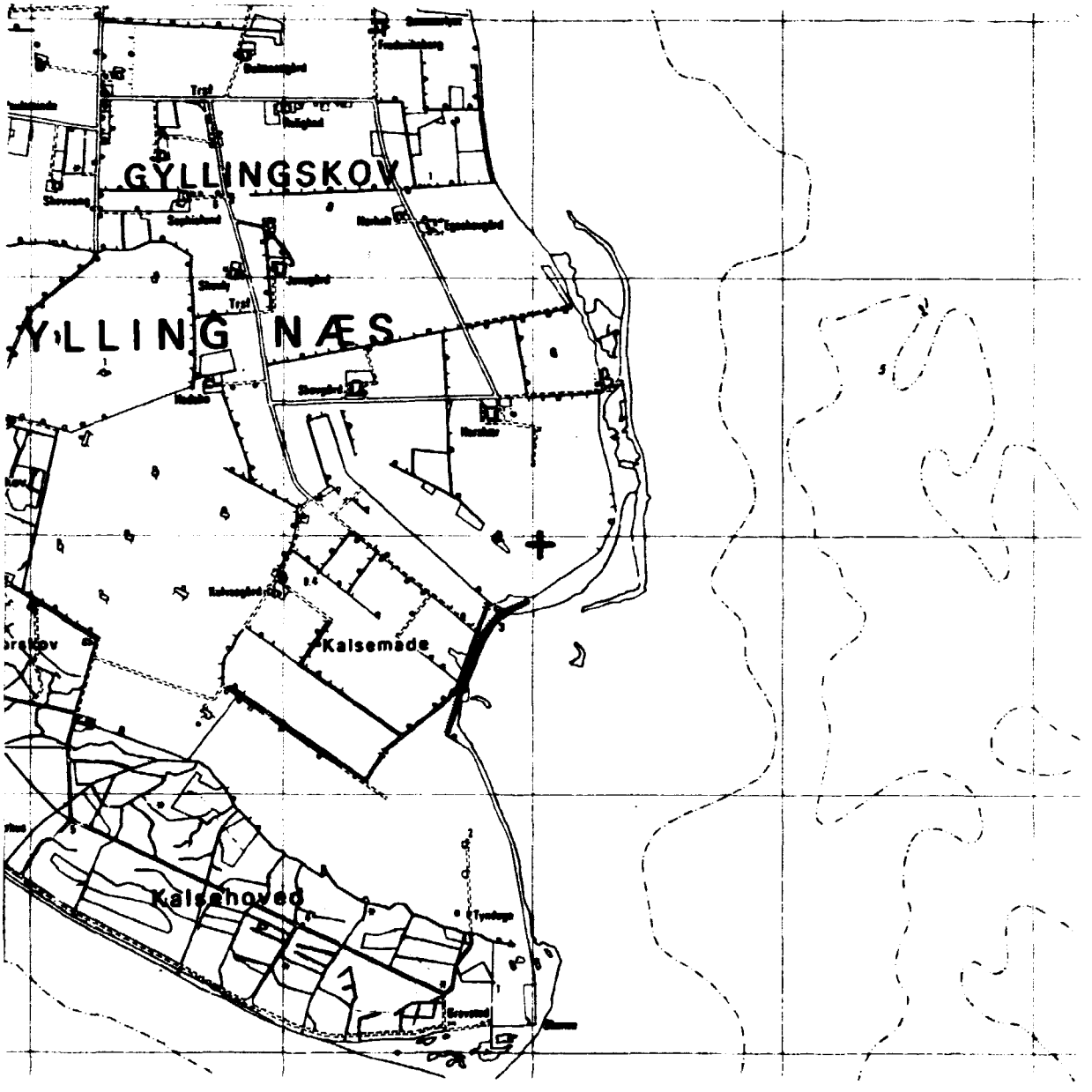

B

2.2. Measuring system and data records

Each of the two meteorological stations incorporates a 17.5 m high mast, instrumented at heights of 2, 10, and 17.5 m above the ground. The wind speed is measured at all levels, while wind direction is measured only at the 17.5 m height; temperature is measured at 2 and 17.5 m. Figure 2.3 displays the buildup of the two identical measuring stations.

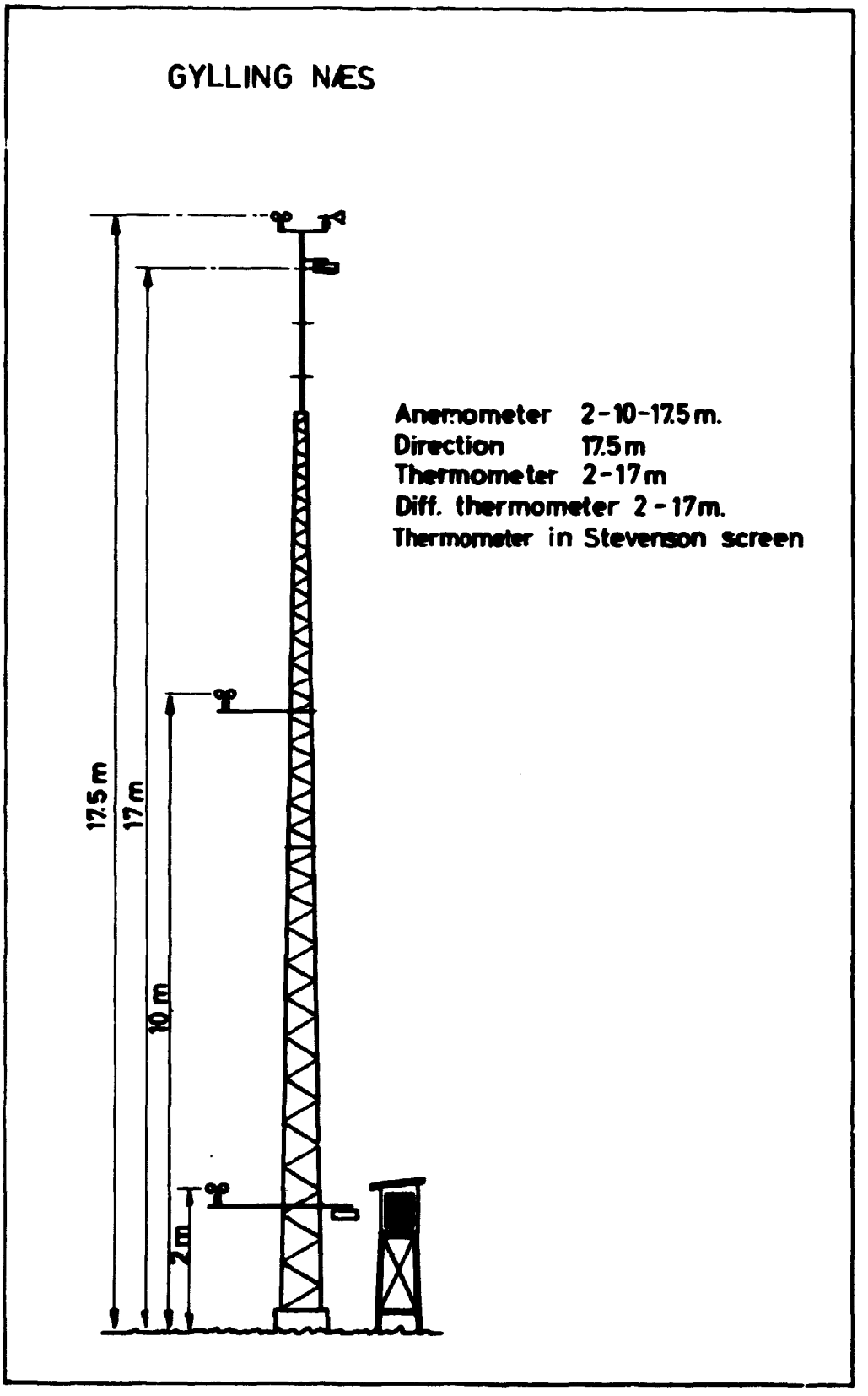

Fig. 2.3. Schematic of the station at Gylling Næs, identical to that at Alrø except for the position of the Stevenson screen.

The recording device is a digital tape recorder, which scans the instruments every ten minutes. The recorded values are ten-minute averages of the wind speed, while values of wind direction and temperature are instantaneous.

As seen from Fig. 2.3 the dew point was measured as well. However, due to difficulties in calibrating this instrument, of a new design, these measurements failed to produce reliable results.

Temperature measurements were performed both as absolute and difference temperatures, between 17.5 m and 2 m, for the purpose of improved resolution.

The data were recorded as 10-bit words and the resulting resolutions for the different sensors were: Absolute temperature: 0.1°C, difference temperature: 0.05°C, velocity: 0.03 m/s, and wind direction: 0.4°.

The overall accuracies for the different sensors were: Wind direction: ± 2° (line-up accuracy plus nonlinearity in the characteristic), velocity: 0-1% overspeeding, ± 1% calibration accuracy and a starting velocity around 30 cm/s (the 1% reflects the maximum overspeeding for these cup anemometers), absolute temperature: -1°C to + 6°C, difference temperature: - 0.2°C to + 0.3°C.

The low accuracies for the temperature sensors were due to radiation errors caused by the non-ventilated radiation shields used at the measuring stations.

At the time of the data analysis on which this report is based, these errors and the problems with their corrections were considered serious enough for us to decide to neglect the temperature measurements in the present analysis. Consequently, we do not use a stability index for the purpose of grouping the data in this report. Later studies by Larsen and Kristensen (1980) showed, however, that the temperature can be satisfactorily corrected for stability calculations, and these were applied in Chapter 4.

The errors in the difference temperatures are less than for the absolute temperature because the difference between the radiation errors, at the two sensors involved in the difference, is much less than the error on each sensor individually.

The measuring period recorded in this report lasted from 25 November 74 to 21 May 76. Due to failures both in instruments and power supply, there are periods of missing data in both records. For the purpose of comparison, the data analyses are based on simultaneous data. The simultaneous sampling efficiency was 78%.

3. INTEGRAL STATISTICS

3.1. Gross statistics

When dealing with meteorology in an inhomogeneous region like Horsens fjord we have some preconcieved ideas as to the qualitative effects of inhomogeneity, such as turning of the wind due to changing surface roughness and channelling of the flow along the fjord. Dynamic effects, like those mentioned, are expected to be incorporated in time-averaged data, but perhaps are concealed in data averaged over directions or wind speeds. Thermal effects due to differences in surface heating and heat capacity could partially be concealed by time averaging.

Figure 3.1 shows the frequency of wind directions and the mean wind speed as functions of direction for the two sites. The direction is standard meteorological with north equal to 0^{o} and positive clockwise. To facilitate computations, the directions are truncated into intervals of 6^{o}. The frequency of directions is somewhat different, especially for westerly directions, and for identical directions there are also significant differences in mean wind speed. We need simultaneous data confined to direction and wind speed intervals to undertake a more detailed analysis. Analyses of this kind will be presented in Chapter 6.

For the sake of completeness, mean wind direction, mean wind speed, and wind speed variance for the two sites are listed in Table 3.1.

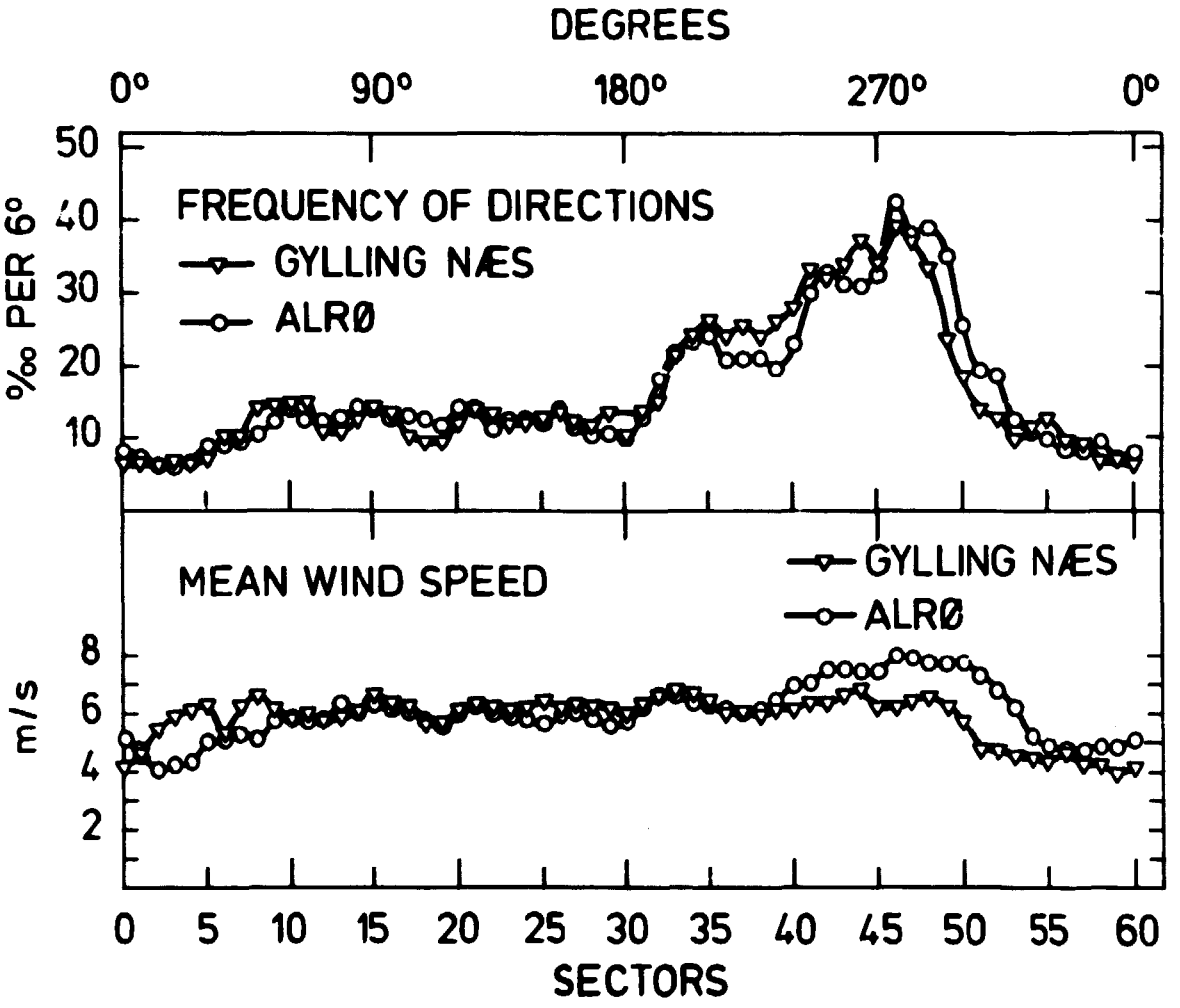

Fig. 3.1. Frequency of wind directions and the variation of mean wind speed with direction, both measured at 17.5 m.

Table 3.1. Mean properties of the wind, measured at 17.5 m.

	Alrø	Gyllingnæs
Mean wind direction	250°	244°
Mean wind speed	6.5 m/s	6.1 m/s
Wind speed variance	11.4 m^2/s^2	8.5 m^2/s^2

3.2. Wind speed probability distributions

For several reasons it is of interest to know the probability distribution of wind speed, independent of direction. We have chosen to compute those statistics based on data from a single year, 1975. It would be preferable to have a multitude of years, but lack of data prohibits that. The probability distributions are based on simultaneous data. The simultaneous data sampling efficiency for that year was 74%.

In Fig. 3.2 the computed probability distributions are shown. The Weibull probability distribution is also given with the scale and shape factors determined from the mean and variance of the wind speeds in 1975.

Justus et al. (1976) showed that the Weibull distribution fits climatological data better than any other distribution. The analytical expression of the Weibull probability distribution is

$$p(V)dV = (k/c)\cdot(V/c)^{k-1}\exp(-(V/c)^k)dV, \qquad (3.1)$$

where c is the scale factor and k the shape factor. The mean and variance in the Weibull distribution is

$$\bar{V} = c\cdot\Gamma(1 + 1/k) \qquad (3.2)$$

$$\overline{V'^2} = c^2\cdot(\Gamma(1 + 2/k) - \Gamma^2(1 + 1/k)), \qquad (3.3)$$

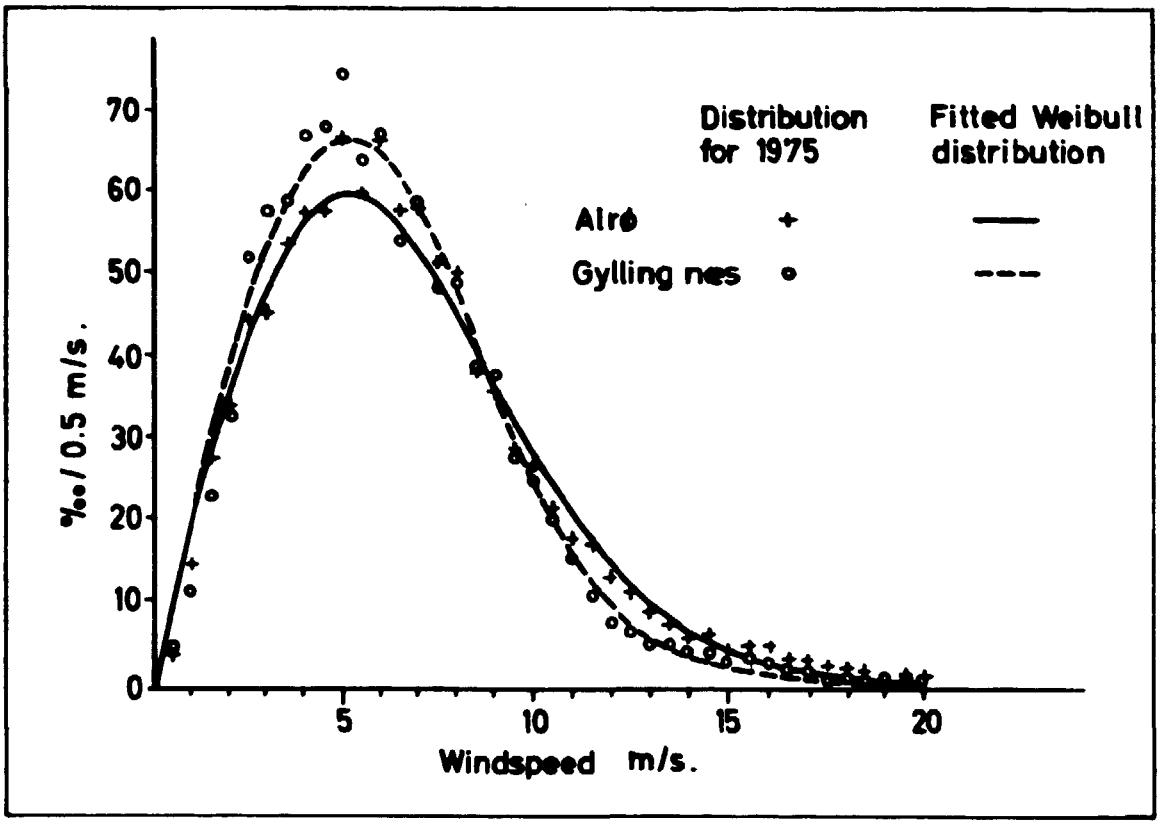

Fig. 3.2. Distribution of wind speed at 17.5 m for the two stations. The curves are the corresponding Weibull distributions (see text).

where Γ is the gamma function. Equations (3.2) and (3.3) may be combined into

$$\frac{\Gamma(1 + 2/k)}{\Gamma^2(1 + 1/k)} = 1 + \frac{\overline{v'^2}}{\bar{v}^2}$$

and

$$c = \bar{v}/\Gamma(1 + 1/k),$$

from which c and k may be determined from the mean and variance of the wind speed distribution. The means and variances of the wind speed distribution for the year 1975, and the determined scale- and shape factors of the Weibull distribution are shown in Table 3.2.

Table 3.2. Data for wind speed distributions for 1975 measured at 17.5 m.

	Alrø	Gylling Næs
$\overline{V}$	6.4 m/s	6.0 m/s
$\overline{v'^2}$	11.1 m^2/s^2	8.6 m^2/s^2
c	7.27	6.82
k	2.02	2.17

The data in Fig. 3.2 show minor deviations from the Weibull distribution. Part of the scatter is due to scarcity of data, but no matter how large a data record is available, natural wind speed distributions will always show departures from a theoretical distribution. The general agreement is good, however, and the Weibull distribution will suffice for most practical applications. It has lately been applied to determine the most probable wind speed distribution at an arbitrary site in Denmark, Petersen et al. (1980). This has been possible by using suitable time series of geostrophic wind and thermal stability.

3.3. Wind vector distributions

Plots of the 2-dimensional probability distribution of the wind vector are very useful for showing the distributions of speed and direction. They can also often reveal directional preferences of the wind, especially if they are marked, such as in mountainous terrain. In lowland regions the directional preferences are often so weak that more detailed analyses are required. Figure 3.3. a-b shows the 2-dimensional probability distribution for the wind vector at the two stations. The wind vector $\vec{V} = (u,v)$, where u is directed towards the east and v towards the north.

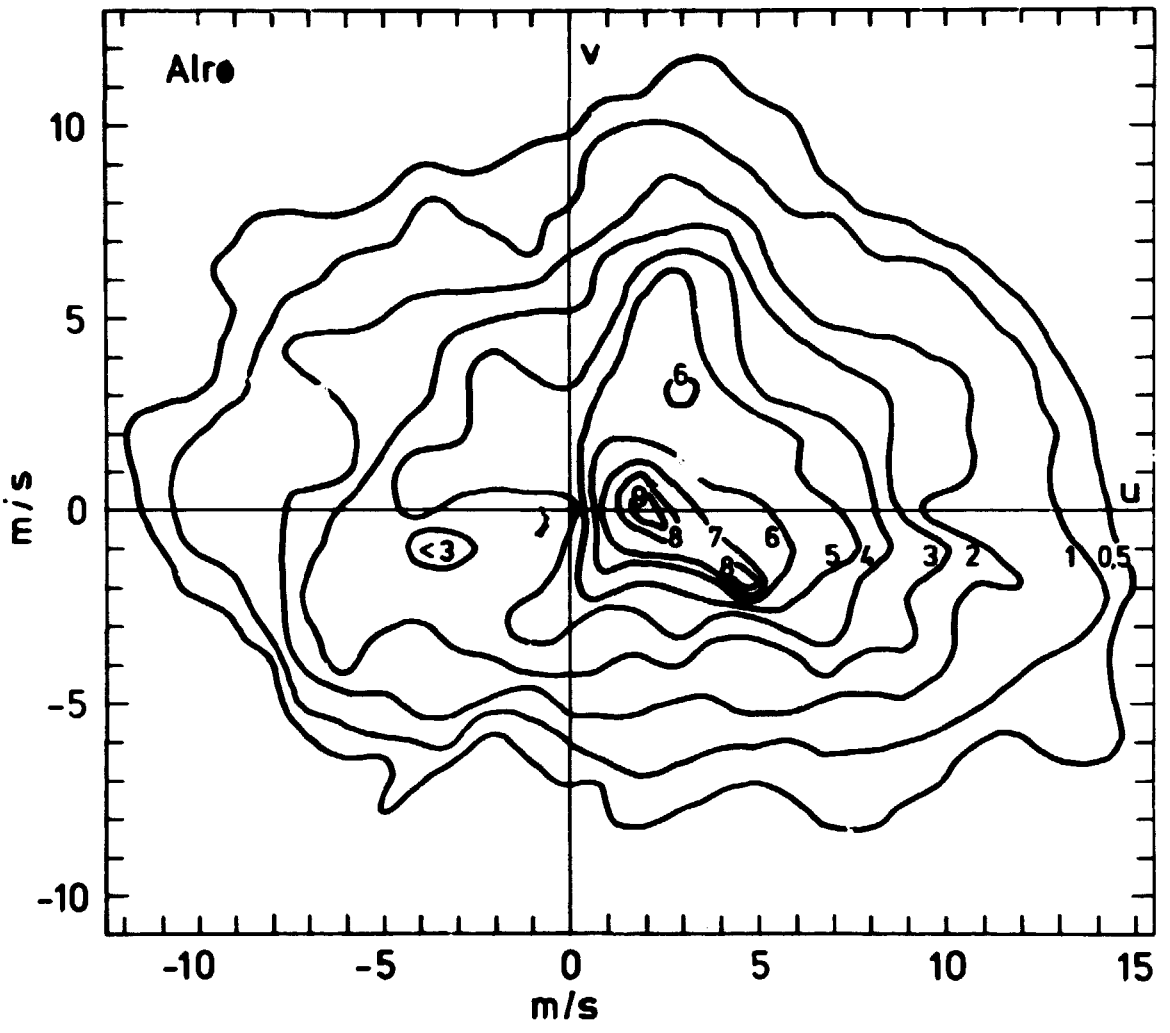

Fig. 3.3.a-b. 2-dimensional probability distributions of the wind vector at 17.5 m. The units are 0/00 per m^2/s^2.

The distributions are not significantly different except for wind speeds less than 5 m/s. At Gylling Næs there is a sharp maximum for westerly winds at ~ 3 m/s. This maximum is somewhat reduced at Alrø and the probability gradients are not so sharp for the smaller speeds. Low wind speeds, therefore, have a slightly more preferred direction at Gylling Næs than at Alrø.

The integral properties of the distributions are shown in Table 3.3 a-b. From the table we see that the magnitude of the mean wind vector at Alrø is 21% greater than that at Gylling Næs. The eddy kinetic energy ($\overline{u'^2} + \overline{v'^2}$) is 16% greater at Alrø. The most striking difference appears in momentum fluxes ($\overline{uv}$ and

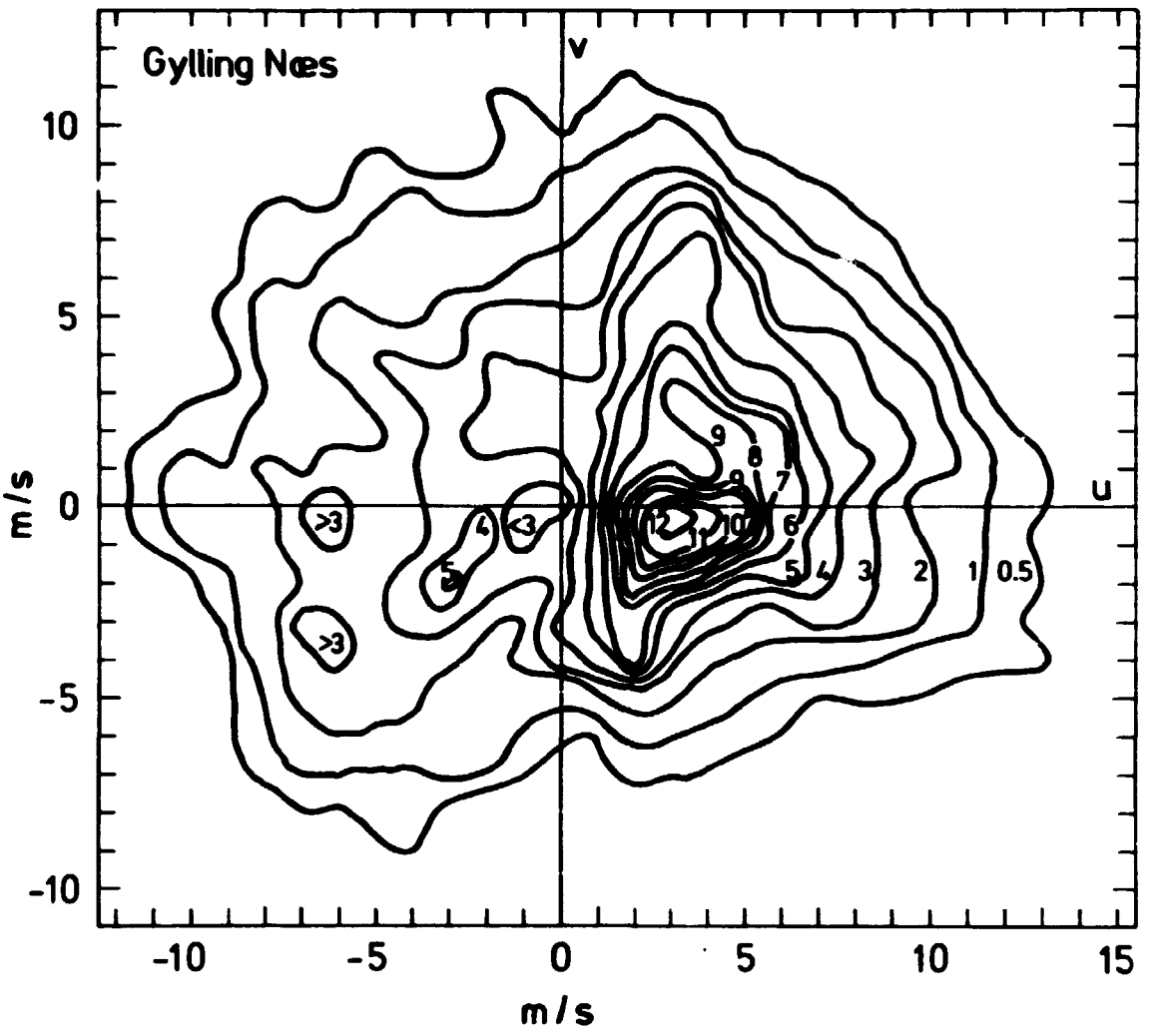

$\overline{u'v'}$). While the flux of total u-momentum is northward at Gylling Næs it is southward at Alrø. This is also the case for the eddy momentum flux ($\overline{u'v'}$). As the data are derived from the same synoptic situations, their differences are the result of local effects. In later chapters we will discuss the processes which are responsible for these differences.

Table 3.3 a-b. a). Values of the mean wind vector at 17.5 m. b) Eddy kinetic energies of the wind vector, eddy momentum flux, and total momentum flux.

a)	$\bar{u}$	$\bar{v}$	Magnitude	Direction
Alrø	2.2 m/s	0.7 m/s	2.3 m/s	253°
Gylling	1.6 -	1.0 -	1.9 -	238°
b)	$\overline{u'^2}$	$\overline{v'^2}$	$\overline{u'v'}$	$\overline{uv}$
Alrø	31.6 m^2/s^2	17.2 m^2/s^2	-2.1 m^2/s^2	-0.6 m^2/s^2
Gylling	25.7 -	16.5 -	1.0 -	2.6 -

In the annex general methods are developed to analyze a wind vector distribution by rotating the coordinate system, particularly for determining the directional preference of the wind vector. In Table 3.4 the results of the analysis are listed.

Table 3.4. Characteristics of the directional analysis. Subscript t refers to total values and e to the eddy part. (For explanation, see text).

	A_t	ϕ_{ot}	P_t	A_e	ϕ_{oe}	P_e
Alrø	9.4 m^2/s^2	-2°	0.17	7.5 m^2/s^2	-8°	0.15
Gylling	6.0 -	13°	0.13	4.7 -	6°	0.11

In the table subscript t refers to the total amount of kinetic energy or momentum flux while the subscript e refers to the eddy portions of the same quantities. A is the amplitude in the sine variation of kinetic energy and momentum flux caused by the rotation of the coordinate system (Eqs. A.2-3 a-c). ϕ_o is the counterclockwise rotation angle of the coordinate system for which the momentum flux across the axis is zero. The direction specified by ϕ_o is also the one which contains a maximum

of kinetic energy. P is the ratio of A to the sum of the component kinetic energies and is a measure of the directional preference of the wind, in that (0.5+P) is the largest fraction of the kinetic energy (either the total or the eddy part) which can be explained by motion along one direction (the direction specified by ϕ_o). For greater detail we refer to the annex.

Figure 3.4.a shows the sine variations in $\overline{u_r v_r}$ and $\overline{u'_r v'_r}$ where the subscript indicates a rotated component (Eqs. A.2-3 c). Also, the variation of the mean northward flux of u momentum as a function of rotation angle is shown. Figure 3.4.b shows the variations in $\overline{u'^2_r}$ (Eq. A.3 a) and the variation of mean kinetic energy $\bar{u}^2_r$.

Of the total eddy kinetic energy at Alrø, 65% at most can be associated with variations in a specific direction, $(0.5+P_e)$ (Table 3.4). The percentage for Gylling Næs is slightly less, 61%. The integral directional preference at Alrø is thus slightly greater. This is true in spite of the apparently greater directional preference for small wind speeds at Gylling Næs (Fig. 3.3 a-b). Petersen (1975) reports a value of eddy directional preference for a Danish 10-year time series at 57% for a 7-m height. A directional preference close to 60% thus seems to be typical of low land stations in temperate latitudes. They are low compared with mountainous regions, which cannot be surprising. Hedegaard (1982) found an eddy directional preference $(0.5 + P_e)$ as high as 94% for a Greenlandic site.

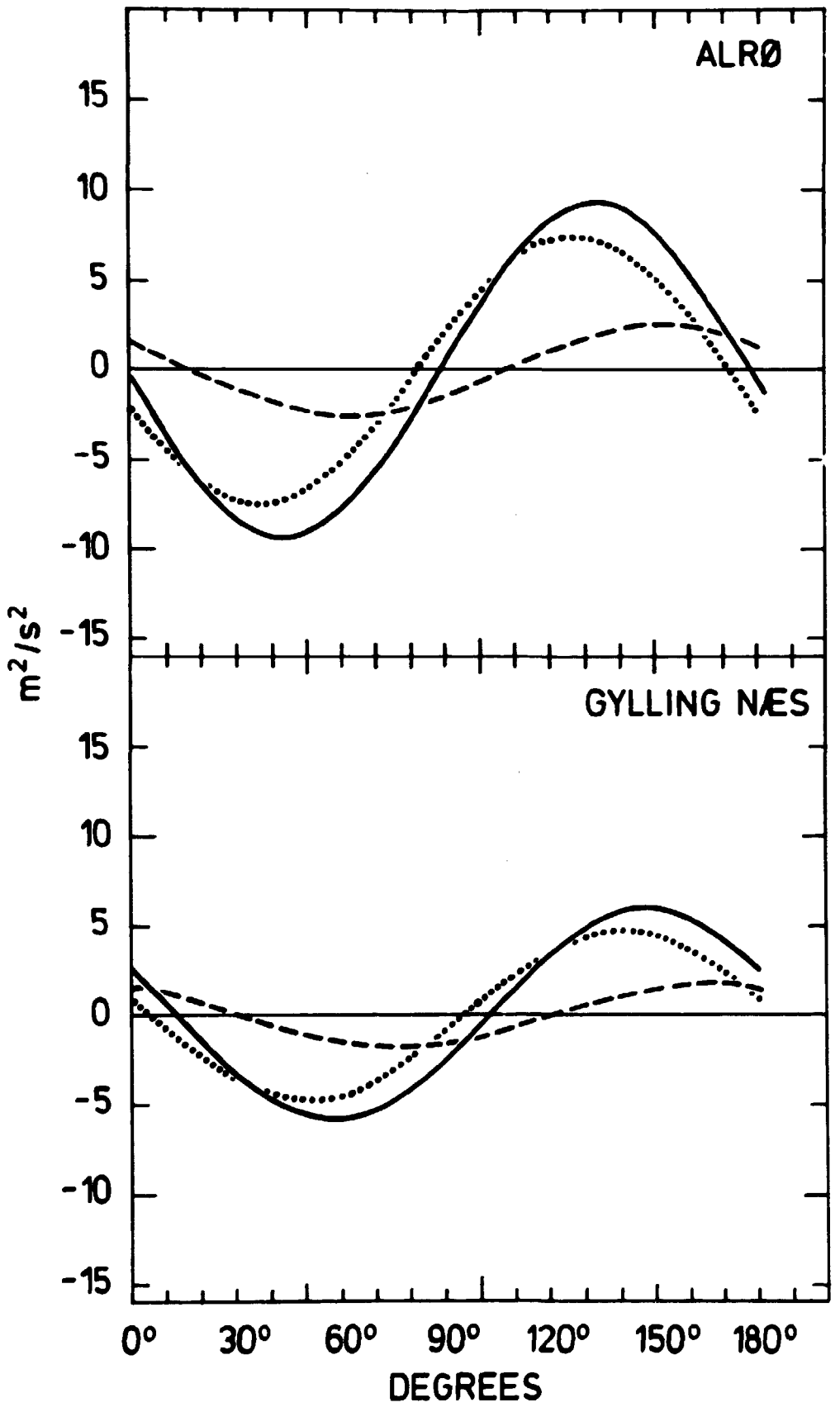

Fig. 3.4.a-b. Variation with rotation angle of statistical properties of the wind vector distribution. a) ——: $\overline{u_r v_r}$, ...: $\overline{u_r' v_r'}$, ---: $\bar{u}_r \cdot \bar{v}_r$. b) ....: $\overline{u_r'^2}$, ---: $\bar{u}_r^2$.

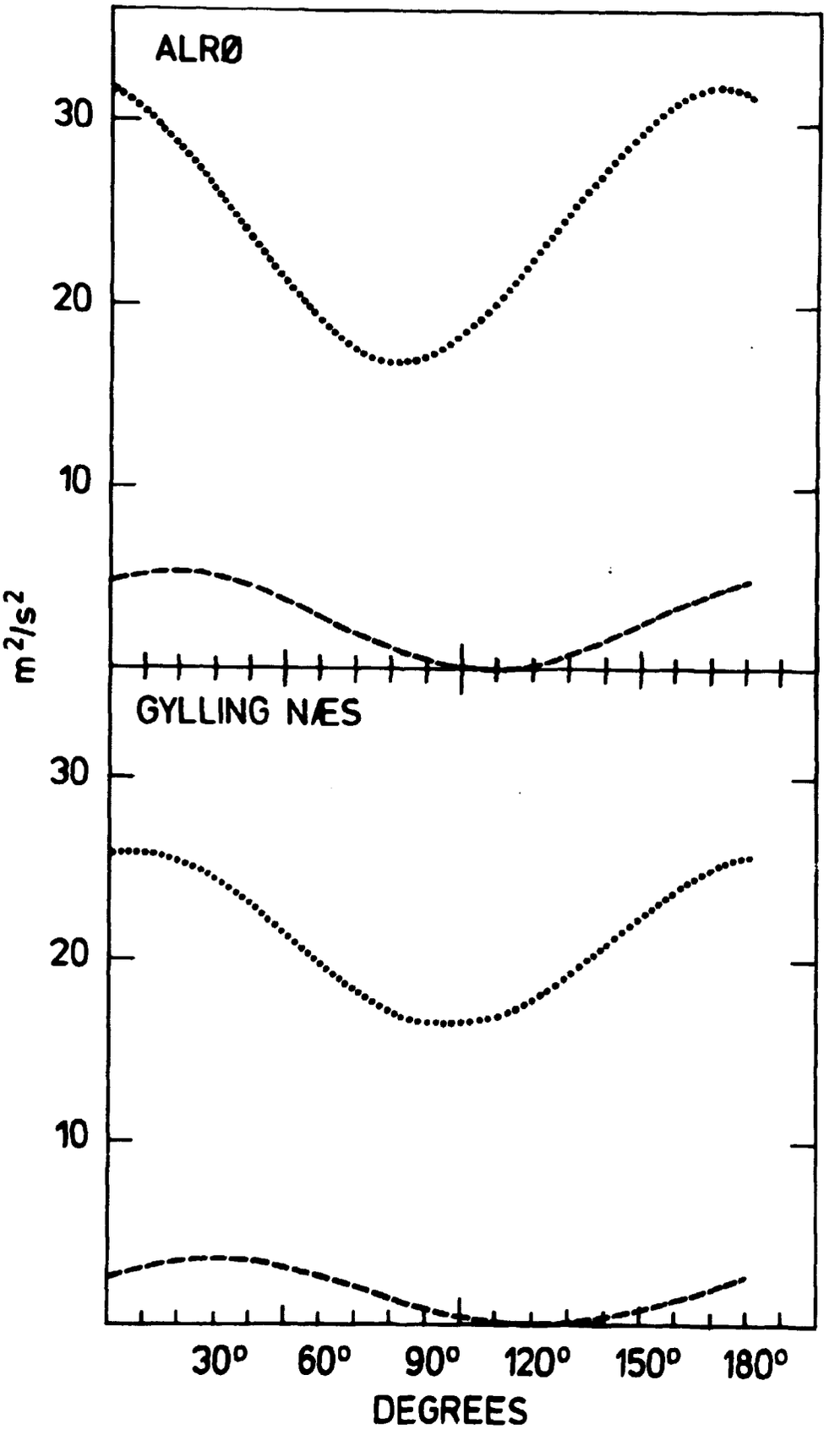
ALRØ
30
20
10
m²/s²
GYLLING NÆS
30
20
10
30°
60°
90°
120°
150°
180°
DEGREES

3.4. Estimate of the net forcing due to inhomogeneity

We have seen that the average momentum fluxes vary between Alrø and Gylling Næs (Table 3.3). As the transport of momentum is of great importance in climatological studies we will try to obtain an estimate of the climatological forcing responsible for the reversal of sign of the momentum transport.

The equations of motion for a two-dimensional flow may be written as

$$\frac{du_i}{dt} = \frac{1}{\rho} F_i \ , \tag{3.4}$$

where F_i is the forcing per unit mass including friction. As

$$\frac{du_i}{dt} = \frac{\partial u_i}{\partial t} + u_j \frac{\partial u_i}{\partial x_j} \ ,$$

and assuming the air to be incompressible, we may write (3.4) as

$$\frac{\partial u_i}{\partial t} + \frac{\partial}{\partial x_j} u_i u_j = \frac{1}{\rho} F_i \ . \tag{3.5}$$

If we neglect time variations in specific gravity, the time average of (3.5) is

$$\frac{1}{\bar{\rho}} \bar{F}_i = \frac{\partial}{\partial x_j} \overline{u_i u_j} \ . \tag{3.6}$$

In usual coordinate form this is written as

$$\frac{1}{\bar{\rho}} \bar{F}_u = \frac{\partial}{\partial x} \overline{u^2} + \frac{\partial}{\partial y} \overline{uv} \ , \tag{3.7a}$$

$$\frac{1}{\bar{\rho}} \bar{F}_v = \frac{\partial}{\partial x} \overline{uv} + \frac{\partial}{\partial y} \overline{v^2} \tag{3.7b}$$

Deviations in the momentum fluxes between nearby sites imply flux divergence for each term. This could add up to a climatological forcing $(\overline{F}_u, \overline{F}_v)$ or only be a redistribution among the fluxes. In order to establish the climatological forcing function, a dense net of stations is necessary. With no more than two stations in operation we can expect only an order of magnitude estimate.

In Fig. 3.5 the locations of the sites in a usual coordinate system is shown. The site at Alrø is chosen as origin, and the point C is the point to which the calculations refer.

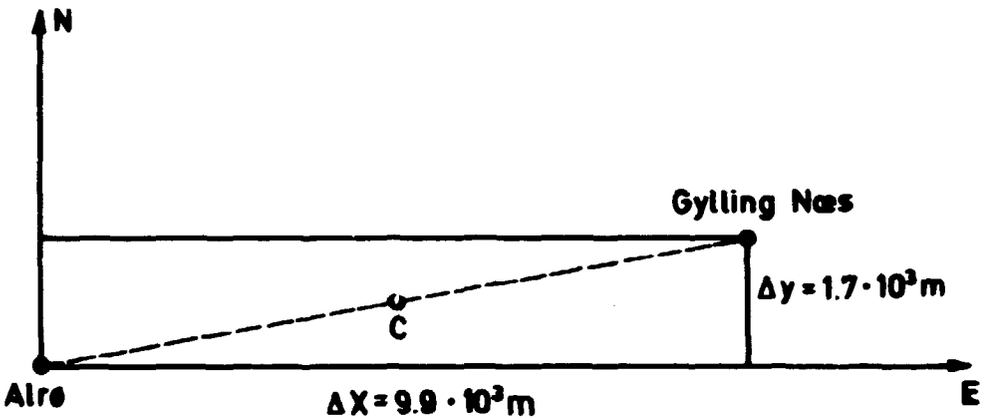

Fig. 3.5. Position of the stations in a coordinate system with Alrø at the origin. The point C is at half the distance between the stations. The gradient computations with finite differences refer to point C.

As $\overline{u^2} = \overline{u}^2 + \overline{u'^2}$, etc. we find from Table 3.3,

$$\frac{1}{\overline{\rho}}(\overline{F}_u, \overline{F}_v) = (-0.16, 0.32)\cdot 10^{-3} + (1.19, -0.12)\cdot 10^{-3} [m/s^2]$$

$$= \frac{1}{\overline{\rho}}(\vec{F}_C + \vec{F}_C') = \frac{1}{\overline{\rho}}\vec{F}_C \quad ,$$

where $\bar{\vec{F}}_c$ is the forcing, which is observed as a divergence of flux of mean momentum, while $\vec{F}'_c$ is the forcing observed as a divergence of flux of eddy momentum. The vectors are plotted in Fig. 3.6 with proper relative magnitude and direction.

As we will see in later chapters, there are different processes affecting the wind field due to the inhomogeneity of the area. Figure 3.6 shows the net result of these processes, but based on this alone it is impossible to deduce anything as to the nature

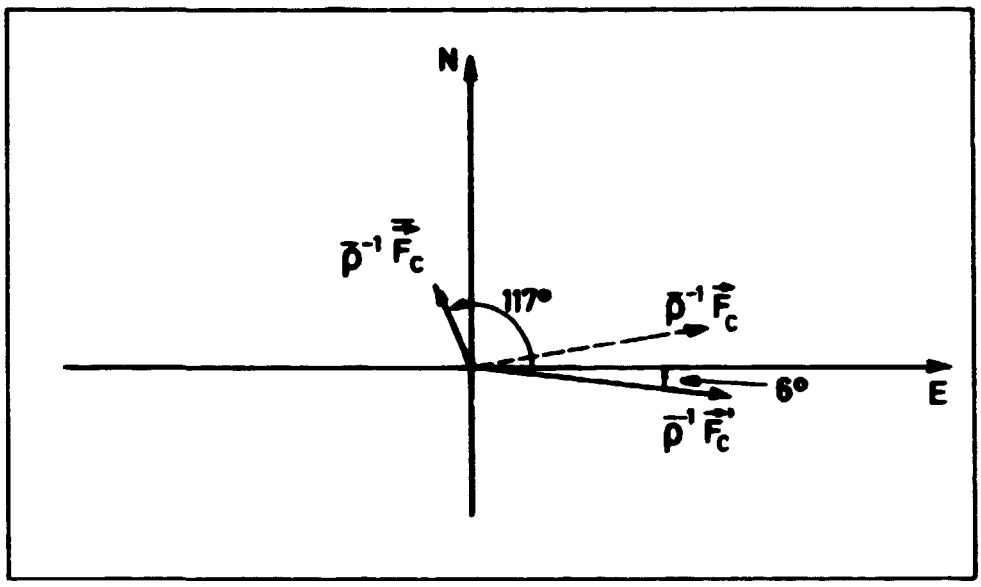

Fig. 3.6. Direction and magnitude of the forcing. $\vec{F}_c$ is the total forcing, $\bar{\vec{F}}_c$ the part caused by divergence of mean momentum flux, and $\vec{F}'_c$ the part caused by divergence of eddy momentum flux.

of the forcing. In the extremes a net forcing could result from a directionally independent forcing acting upon an anisotropic wind vector probability distribution, or from one varying with direction acting upon an isotropic distribution. As the wind vector probability distribution is anisotropic and the terrain too complicated to allow a forcing independent of direction, this case is somewhere in between the extremes.

It is interesting to compare the net forcing with ordinary meteorological forces, such as the pressure gradient or Coriolis force. The magnitude of $(1/\bar{\rho})\vec{F}_c$ is $1.1 \cdot 10^{-3}$ m/s^2. This is equivalent to the Coriolis force acting on an air mass with a speed at 9 m/s (at 56° N), or to the pressure gradient force from a gradient at 1.3 mb per 100 km. The net forcing caused by the inhomogeneous terrain is therefore by no means negligible.

4. WIND PROFILES IN HOMOGENEOUS TERRAIN

Under the usual idealized conditions (i.e. horizontal homogeneity and stationarity) the wind shear in the surface boundary layer (abb. SBL) is given by

$$\frac{\partial \bar{u}}{\partial z} = \frac{u_{*o}}{kz} \phi_m(\xi) \quad , \tag{4.1}$$

where z is the measuring height, k (=0.4) is the von Karman constant, u_{*o} the friction velocity (defined below), and $\xi \equiv z/L$ a non-dimensional stability parameter, where L is the Monin-Obukhov length defined by

$$L \equiv - \frac{T}{gk} \frac{u_{*o}^3}{\overline{w'T'}} \quad .$$

Here T is temperature, g gravity, $\overline{w'T'}$ the vertical heat flux, and $u_{*o}^2 \equiv - \overline{u'w'}$, where $\overline{u'w'}$ is the vertical flux of momentum. ϕ_m is an empirically determined function and according to Businger (1973), it has the form

$$\phi_m = (1-15\ \xi)^{-1/4} \quad \text{for } \xi < 0 \quad , \tag{4.2a}$$

$$\phi_m = 1 + 4.7\ \xi \quad \text{for } \xi \geq 0 \quad . \tag{4.2b}$$

Integrating (4.1), with the boundary condition $\bar{u}(z_o) = 0$ defining the roughness length z_o, gives the following, Businger (1973),

$$u(z) = \frac{u_{*o}}{k} \left(\ln \frac{z}{z_o} - \psi(\xi)\right), \tag{4.3}$$

where

$$\psi(\xi) = 2 \cdot \ln[(1+x)/2] + \ln[(1+x^2)/2] - 2 \arctan(x) + \frac{\pi}{2}$$

$$\text{for } \xi < 0 \text{ with } x \equiv (1-15\,\xi)^{1/4} \tag{4.4a}$$

and

$$\psi(\xi) = -4.7\,\xi \quad \text{for } \xi \geq 0\ . \tag{4.4b}$$

Expressions equivalent to (4.1) and (4.3) exist for the potential temperature profile (see Businger (1973)).

From Eq. (4.3) we see that the wind speed is proportional to u_{*o}, and further that $\bar{u}$ decreases for increasing z_o. The variation with ξ is more complicated, but considering Eq. (4.4a-b) we find that $\bar{u}(z)$ increases for decreasing ξ. However, u_{*o}, z_o, and ξ are not independent and this makes matters somewhat more complicated.

The friction velocity, u_{*o}, is determined partly by local effects such as z_o, partly by larger-scale effects, such as the geostrophic wind, G, and the height, λ, of the planetary boundary layer (abb. PBL). This relation may be expressed in dimensionless form as

$$\frac{u_{*o}}{G} = F(Ro, \mu)\ , \tag{4.5}$$

where F is a universal function of the dimensionless variables, Ro and μ, $Ro \equiv G/fz_o$ being the surface Rossby number (f, the Coriolis parameter, is $1.21 \cdot 10^{-4} s^{-1}$ at 56^oN) and $\mu \equiv \frac{\lambda}{L}$ a non-

dimensional thermal stability measure, where λ is a characteristic height of the PBL. u_{*o}/G is usually called the geostrophic drag coefficient, not to be confused with the ordinary drag coefficient, $c_D \equiv (u_{*o}/\bar{u}_{10})^2$. At present we will be concerned with the SBL, but will later return to Eq. (4.5).

As we are discussing averaged data the problem of instationarity is eliminated. The effect of terrain inhomogeneities, however, is still present in averaged data. We will see later that even small inhomogeneities and slopes in the terrain have a profound effect in obtaining reasonable values of, e.g., the momentum flux from the measured wind profiles. Instead, we will use SBL theory partially to eliminate the effect of thermal stratification upon averaged profiles in order to determine the effect of terrain inhomogeneities. Furthermore, we will use the theory to establish equilibrium conditions for the different types of terrain.

4.1. Stability effects in climatologically averaged profiles

On the average, the atmosphere is stratified in a slightly stable manner, i.e. $\partial\tilde{\theta}/\partial z$ is small but positive. Here θ is the potential temperature and the tilde refers to climatological average.

In order to detect topographical effects from averaged profiles, it is convenient, at first, to eliminate the effects of thermal stratification. From Eq. (4.3) the climatological averaged wind profiles are

$$\tilde{u}(z) = \frac{\ln\frac{z}{z_o}}{k} \int_{-\infty}^{\infty} u_{*o}\, n(\xi)d\xi - \frac{1}{k}\int_{-\infty}^{\infty} u_{*o}\psi(\xi)n(\xi)d\xi \tag{4.6}$$

$$= \frac{\ln\frac{z}{z_o}}{k} \cdot \tilde{u}_{*o} - \frac{1}{k}\widetilde{u_{*o}\psi},$$

where $n(\xi)$ is the normalized distribution function for stability. We have used ξ as an independent variable because ψ is a unique function of ξ, but we could equally well have used any other distribution, for example $n(G)$.

In order to facilitate our computations we assumed $n(\xi)$ to be independent of direction. This is not strictly valid, but we consider it to be a reasonable first-order approximation, which suffices for this purpose.

There exists a unique relationship between the stability parameter, ξ, and the more easily determined quantity Ri, the gradient Richardson number, defined by

$$Ri \equiv \frac{g}{T} \frac{\partial \bar{\theta}/\partial z}{(\partial u/\partial z)^2} .$$

According to Golder (1972), ξ can be substituted for by Ri when $Ri < 0$. For $Ri \geq 0$, the ϕ_m and ψ functions have the following forms with Ri as independent variable.

$$\phi_m(Ri) = \frac{1}{(1-\beta Ri)} \qquad (4.7)$$

$$\psi(Ri) = - \frac{\beta Ri}{(1-\beta Ri)} , \qquad (4.8)$$

where $\beta = 7$.

Using temperature and wind speed from $z_1 = 2$ and $z_2 = 17.5$ m, we were able to determine Ri by approximating the gradients by finite differences. Assuming the profiles to be approximately log linear, the Ri determined in this way refer to the height $z_a \equiv (z_2-z_1)/\ln(z_2/z_1)$. With the present values of z_1 and z_2, $z_a = 7$ m.

By using the appropriate ϕ_m function, we could find u_{*o} from each profile. From this we were able to determine $\tilde{u}_{*o}$ and $\widetilde{u_{*o}\psi}$. While the former is independent of height, the latter was computed for each measuring height, i.e. for 2, 10, and 17.5 m.

The computed $\tilde{u}_{*o}$ values are apparent only, because they are determined on the assumption of horizontal homogeneity. In spite of this we consider the $\tilde{u}_{*o}$ and $\widetilde{u_{*o}\psi}$ values to be good approximations to the stability effect in inhomogenous terrain.

In Table 4.1 the values of $\tilde{u}_{*o}$ and $\widetilde{u_{*o}\psi}$ for the two sites are shown.

Table 4.1. Characteristics of the averaged wind profiles. (For explanation, see text).

	Gyllingnæs			Alrø		
z(m)	2	10	17.5	2	10	17.5
u(m/s)	4.83	5.87	6.17	4.96	6.29	6.59
$\tilde{u}_{*o}$(m/s)	0.21	0.21	0.21	0.25	0.25	0.25
$\widetilde{u_{*o}\psi}$(m/s)	0.00	- 0.04	- 0.08	- 0.01	- 0.06	- 0.13

We see that the stability effect, i.e. $\widetilde{u_{*o}\psi}$, is slightly greater at Alrø than at Gyllingnæs. A possible explanation for that is the bias of the measuring period (Nov 74 - May 76) towards spring. The cold water in spring and the proximity of the measuring site at Alrø to the shoreline would cause the thermal stratification at this site to be biased towards stable conditions.

The stability effect upon the averaged profiles may be appreciated by rewriting Eq. (4.6) as

$$\tilde{\bar{u}}(z) = \frac{\tilde{u}_{*o}}{k} \ln \frac{z}{c(z) \cdot z_o} \quad , \tag{4.9}$$

where

$$c(z) = \exp \frac{\widetilde{u_{*o}\psi_z}}{\widetilde{u_{*o}}} \quad .$$

The value of c for the two sites ranges from close to 1 for z = 2 m down to ~ 0.6 for z = 17.5 m. The assumption that climatologically averaged profiles are logarithmic in determining z_o may lead to a 40% underestimate in z_o. As we will see later, this error is negligible in the z_o determination compared with errors introduced by terrain inhomogeneities.

5. EFFECTS OF TERRAIN INHOMOGENEITIES

The ideal situation of horizontal homogeneous terrain is seldom encountered in nature, and in applications of micrometeorology to fields such as site evaluation one usually has to work with heterogeneous terrain.

Heterogeneities may be present in such characteristics as albedo, heat capacity, or roughness of the surface. Changes in any of these properties alter the boundary layer, whereby both speed and direction of the surface wind are changed. Heterogeneity may also be present in topography strongly enough to change the wind field.

In the chapter on integral statistics (Chap. 3), we mentioned the horizontal shear in momentum fluxes in the area, but were unable to give any description of its causes. In this chapter we look further into the boundary layer equations, especially the effects of terrain inhomogeneities.

5.1. Development of the internal boundary layer

The data from our two masts are influenced by different changes in the surface conditions near the masts: a) step changes in surface roughness, b) step changes in surface elevation, c) sloping terrain, and d) step changes in surface heat flux. Below we shall briefly summarize important aspects of the flow response to such changes.

When a uniform flow encounters a step change in surface roughness, an internal boundary layer (abb. IBL) is created. In recent times much work has been done to determine the structure and rate of growth of the IBL (see, e.g. Bradley (1968), Rao et al. (1974), and Rao (1975)). Figure 5.1, which is taken from Rao et al. (1974), shows a schematic model of the flow in the case of a roughness change. The magnitude of the roughness change, m, is usually defined as $m = z_{02}/z_{01}$, where index 2 refers to downstream and 1 to upstream conditions.

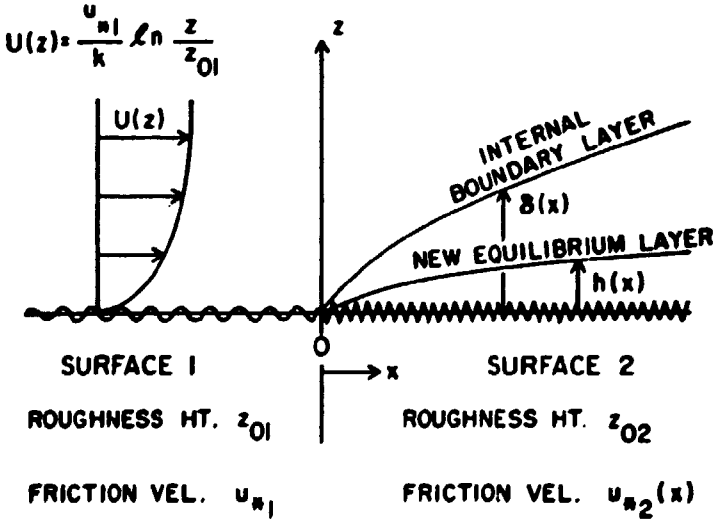

Fig. 5.1. Diagram of the internal boundary layer (IBL) over a step change of surface roughness (From Rao et al., 1974).

The IBL can be defined as the layer in which roughness change affects the velocity. It is customary to define the depth,

δ, of the IBL as the height where the velocity is within 1% of its upstream value. For neutral stratification, Rao et al. (1974) found, based on a 2-dimensional model with second-order closure, that $\delta/z_o = 0.4 \cdot (x/z_o)^{0.8}$, where x is the distance downstream of the roughness change, and z_o is the roughness of the rougher of the two surfaces. The growth of δ is slightly, but insignificantly, dependent upon the sign of the roughness change. This result agrees well with field experiments (see, for example, Bradley (1968)).

In a manner similar to that found for the layer of altered velocity (the IBL), a layer of equilibrium stress can be defined. Its layer depth is defined as the height where the stress is within 90% of the surfacs stress. Rao et al. (1974) found that the depth of the stress layer is ~ $0.1 \cdot \delta$. However, the new surface stress is not in accordance with that predicted by the geostrophic drag law. We shall return to this point in Section 5.2.

The development of the IBL in the case of non-neutral stratification has not been investigated as thoroughly as the neutral case. Rao (1975) found that in unstable stratification, $\delta = x^n$, where n increases with increasing instability. For strongly unstable strafification, $n = 1.4$ is found. For stable stratification, we qualitatively expect the IBL to grow more slowly than in the neutral case.

Flow over low 2-dimensional hills has recently been studied by various authors, notably Jackson and Hunt (1975) and Jensen and Peterson (1978). Their results pertain to neutral situations only at the moment, and the extension to diabatic cases must be made in qualitative terms. We summarize their results here on the upstream side of the hill only. In this case, the pressure perturbations will influence the velocity profile up to a height, L, where L is the horizontal length scale of the hill. Up to a height, δ_p, the velocity and the stress will increase with a constant factor $(1+s)$ and $(1+s)^2$, respectively. The fractional overspeeding, s, is constant with height but increases as one moves uphill until it reaches its maximum value approximately at the top of the hill.

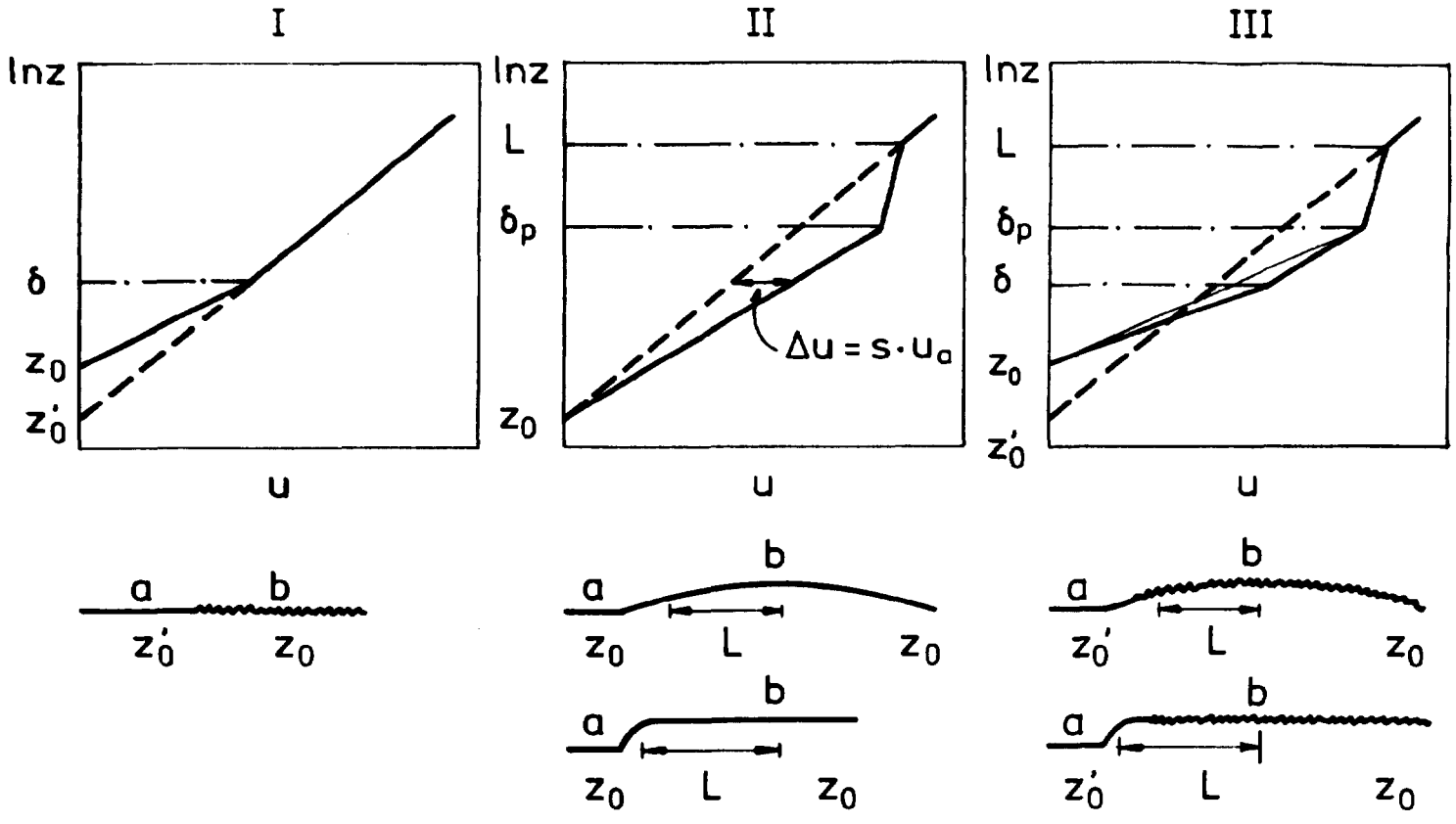

Fig. 5.2. I-III. Schematics of three different types of internal boundary layers, with examples of possible surface configurations. The solid line shows the profile at position b, while the dashed line illustrates the upstream profile at position a. Notice that if the distance between b and the change of roughness equals L then $\delta = \delta_p$ in III and the resulting profile is indicated by the thin solid line. (The figure is based on discussions with N.O. Jensen, Risø).

The height, δ_p, is described by a formula similar to that describing the height of the internal boundary layer for a step change in roughness: $\delta_p/z_o \approx 0.4\ (L/z_o)^{0.8}$ while the maximum fractional speed up, s, is given by $s \approx c\ h/L$, where h is the height of the hill and c a coefficient of order 1; this coefficient is dependent mainly on the shape factor of the hill (see Jensen and Peterson (1978)). For a low hill Jackson and Hunt (1975) found $c \approx 2$.

Based on data obtained at Risø, Jensen and Peterson (1978) conclude that the formula for the hill-boundary layer can be extended to describe the behaviour of the boundary layer behind an escarpment, provided the distance to the escarpment, x, is substituted for L, where now h is the height of the escarpment. For such cases they find $s \approx 2h/x$, meaning that the coefficient $c \approx 2$. Notice that the height, δ_p, of the internal boundary layer after an escarpment corresponds exactly to the height, δ, of a roughness change-induced internal boundary layer.

Jensen and Peterson (1978) suggest that the combined effect of a roughness change and a hill or an escarpment can be obtained by linear superposition of the internal boundary layers caused by each phenomenon individually.

Different internal boundary layers are illustrated in Fig. 5.2. Finally, it should be said that no satisfactory theory has been developed to describe the flow response to step changes in surface heat flux. Therefore, we are at present unable to take this point into consideration.

5.2. The equilibrium PBL equations. Requirements for establishing the equilibrium

In the above-mentioned model studies, the upstream boundary condition was a stationary flow over homogeneous terrain, where the vertical stress gradients (the frictional force) was balanced by a departure of the surface wind from the geostrophic wind. This state of equilibrium is usually expressed as the geostrophic

drag law, and may be expressed as (following Tennekes (1973))

$$\frac{U_g}{u_{*o}} = \frac{1}{k} \ln \frac{u_{*o}}{f z_o} - \frac{B(\mu)}{k} \qquad (5.1.a)$$

$$\frac{V_g}{u_{*o}} = - \frac{A(\mu)}{k} \; . \qquad (5.1.b)$$

A and B are the Kazanski-Monin dimensionless functions and U_g, V_g the components of the geostrophic wind in a right-handed coordinate system with x-axis positive in the direction of the surface wind $\vec{V}$. The other variables were defined in Chapter 4. By use of the cross isobaric angle (shown in Fig. 5.3) Eq. (5.1.a-b) can be transformed to

$$\ln Ro = B(\mu) - \ln\left(\frac{u_{*o}}{G}\right) + \left[k^2\left(\frac{u_{*o}}{G}\right)^{-2} - A^2(\mu)\right]^{1/2} \qquad (5.2.a)$$

$$\sin \alpha = \frac{A(\mu)}{k} \frac{u_{*o}}{G} \; . \qquad (5.2.b)$$

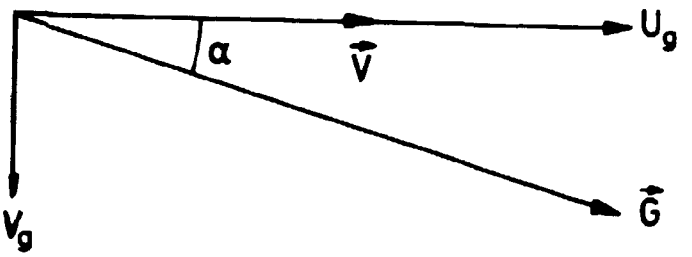

Fig. 5.3. Definition of the coordinate system and the angle α. As $\vec{G}$ is along the isobars, α is called the cross isobaric angle.

Equation (5.2.a) is the relation mentioned in Chapter 4: $u_{*o}/G = F(Ro,\mu)$. The variation in geostrophic drag coefficent with Ro is shown in Fig. 5.4 for the neutral case, i.e. $\mu = 0$. In Eq. (5.2.b) we have considered α as positive. We did it for convenience and shall follow this practice below.

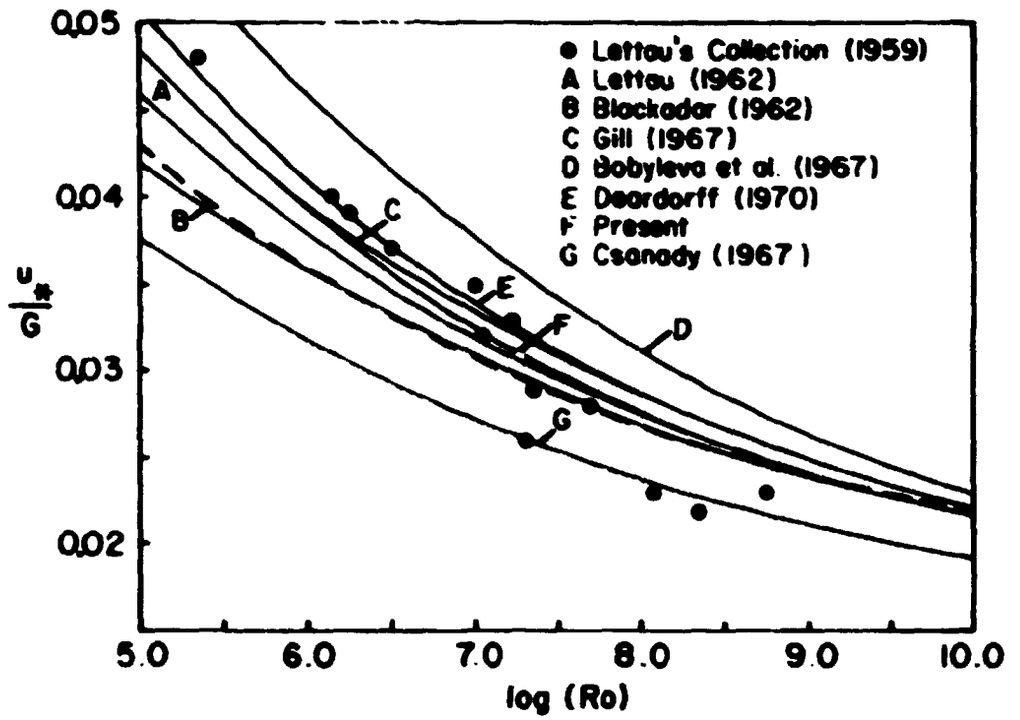

Fig. 5.4. Measured and theoretical values of the geostrophic drag coefficient u_{*o}/G for neutral stratification (after Jensen, 1978). The dashed line is the approximation $u_{*o}/G = 0.5\ (\ln Ro)^{-1}$ proposed by Jensen (1978).

The Monin-Kazanski functions, A(μ) and B(μ), are empirically determined, and due to non-ideal effects such as instationarity and baroclinicity, there is considerable scatter in their values. Figure 5.5 shows A and B from O'Neill data, from Tennekes (1973), and the scatter is obviously large. The assertion of values to A and B for the neutral case alone is uncertain also, as clearly reflected in the curves in Fig. 5.4.

From Eq. (5.2.a) u_{*o}/G can be implicitly determined only. It is, therefore, difficult to apply the equation for practical purposes. For the neutral case, Jensen (1978) determined an explicit expression,

$$u_{*o}/G = 0.5 \cdot (\ln Ro)^{-1} , \qquad (5.3)$$

which, from Fig. 5.4, is seen to be just as good a fit as the implicit expression. It is possible to generalize this expres-

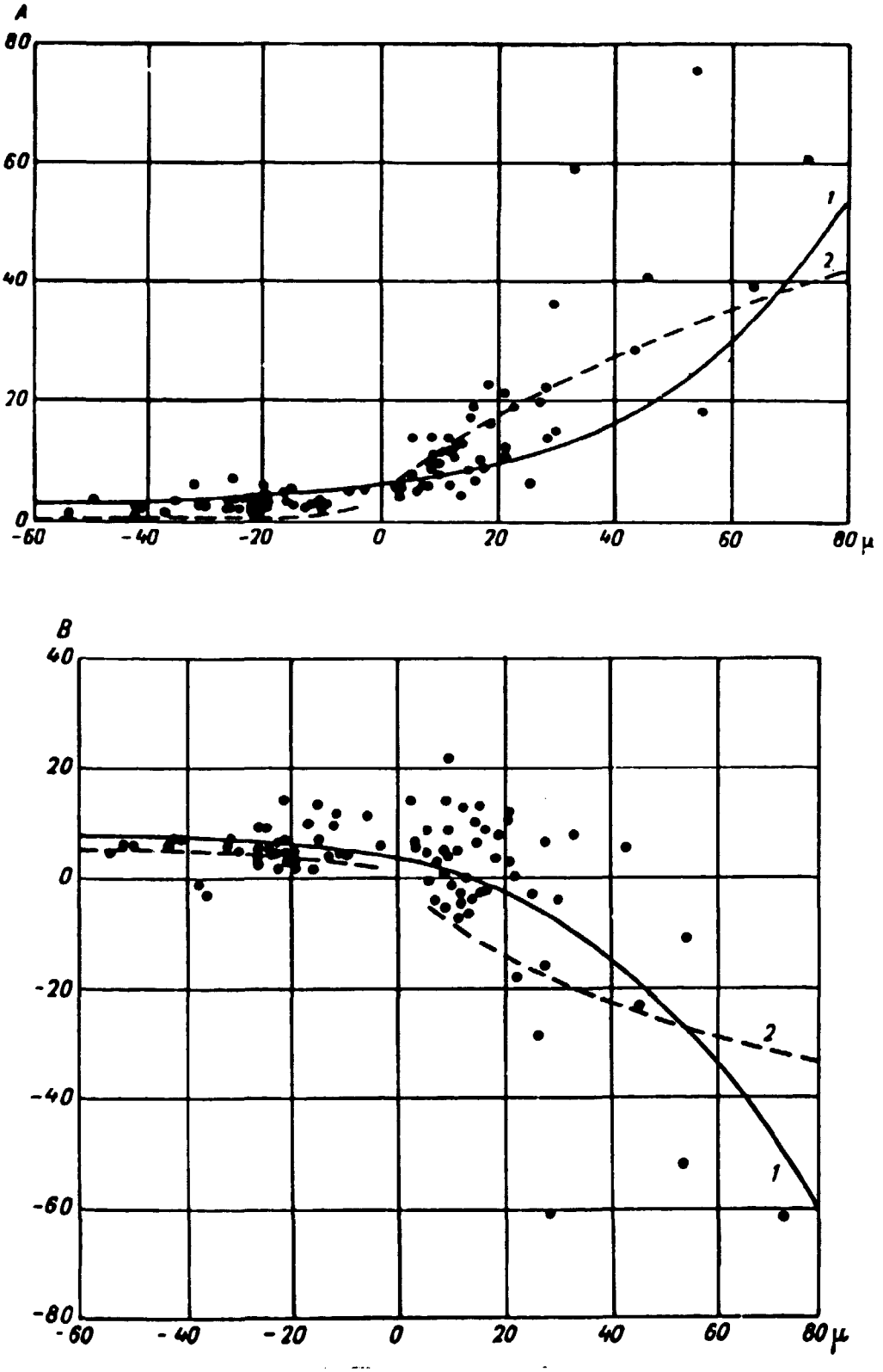

Fig. 5.5.a-b. The Monin-Kazanski functions A(μ) and B(μ) based on O'Neill data. The solid line is the best fit while the dashed line is based on theory (after Tennekes (1973)). a) A(μ), b) B(μ).

sion to include diabatic PBL's as well. Based on the best fit values of A and B from the O'Neill data, we found the following general explicit expression, valid for $\mu \in [-60,60]$:

$$u_{*_O}/G = E(\mu) \cdot (\ln Ro)^{(\frac{\mu}{60}-1)} \quad , \tag{5.4}$$

where $E(\mu) \equiv 0.54 \cdot \exp[-\mu(0.063 + 9.1 \cdot 10^{-5}\mu)]$.

Figure 5.6 shows this expression for selected values of Rossby numbers against the values derived from Eq. (5.2.a). Except for the very unstable cases, the fit is perfect, and the deviations for the unstable cases are only minor compared with the uncertainty in determining A and B.

From Fig. 5.6, the invariance with the Rossby number in the stable limit is clear. The strong dependence of u_{*_O}/G upon Ro for the low values of μ is surprising. In the free convection limit, the momentum exchange through the PBL is governed by buoyancy, and the momentum exchange in this limit should, therefore, be invariant with the Rossby number. For a PBL height of order $2 \cdot 10^3$ m we have $L \sim -30$ m for $\mu = -60$. This is moderate to strongly unstable, but not in the free convection limit. However, in the limiting case $\mu \to -\infty$, i.e. $L \to 0$, we expect u_{*_O}/G to become invariant with Ro. This effect could be included in the explicit expression for u_{*_O}/G by considering higher powers of μ. We have not considered this point further, as our main concern will be with averaged conditions with μ values close to neutral.

From the values of u_{*_O}/G as a function of stability (the dots on Fig. 5.6) together with the best fit value of $A(\mu)$ from the O'Neill data, we are able to determine the cross isobaric angle, α, as a function of PBL stability (Eq. 5.2.b). For selected Rossby numbers these curves are shown in Fig. 5.7. We have used the implicitly determined values of u_{*_O}/G (from Eq. 5.2.a) and

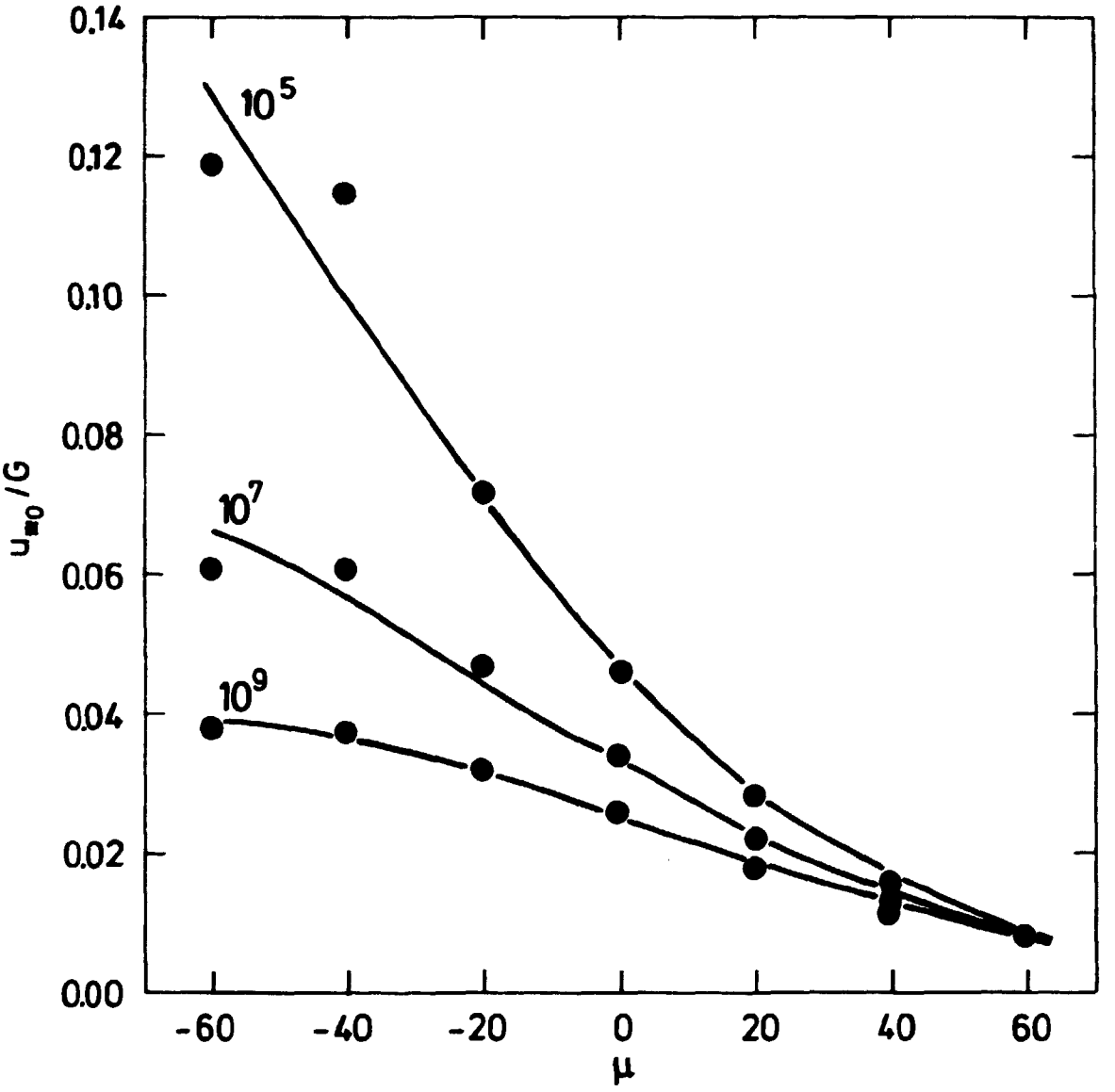

Fig. 5.6. The general explicit expression for u_{*o}/G as a function of stability for different Rossby numbers (Eq. 5.4). The dots are derived from the best fit values of A and B from O'Neill data (cf. Fig. 5.5).

not the explicit, but approximate, values given by Eq. (5.4). We have rejected the latter approach due to the sensitivity of α to even small variations in u_{*o}/G.

From Fig. 5.7 it is clear that variations in both stability and roughness (through Ro) have noticeable effects upon the cross isobaric angle, both having the largest effect for the smaller

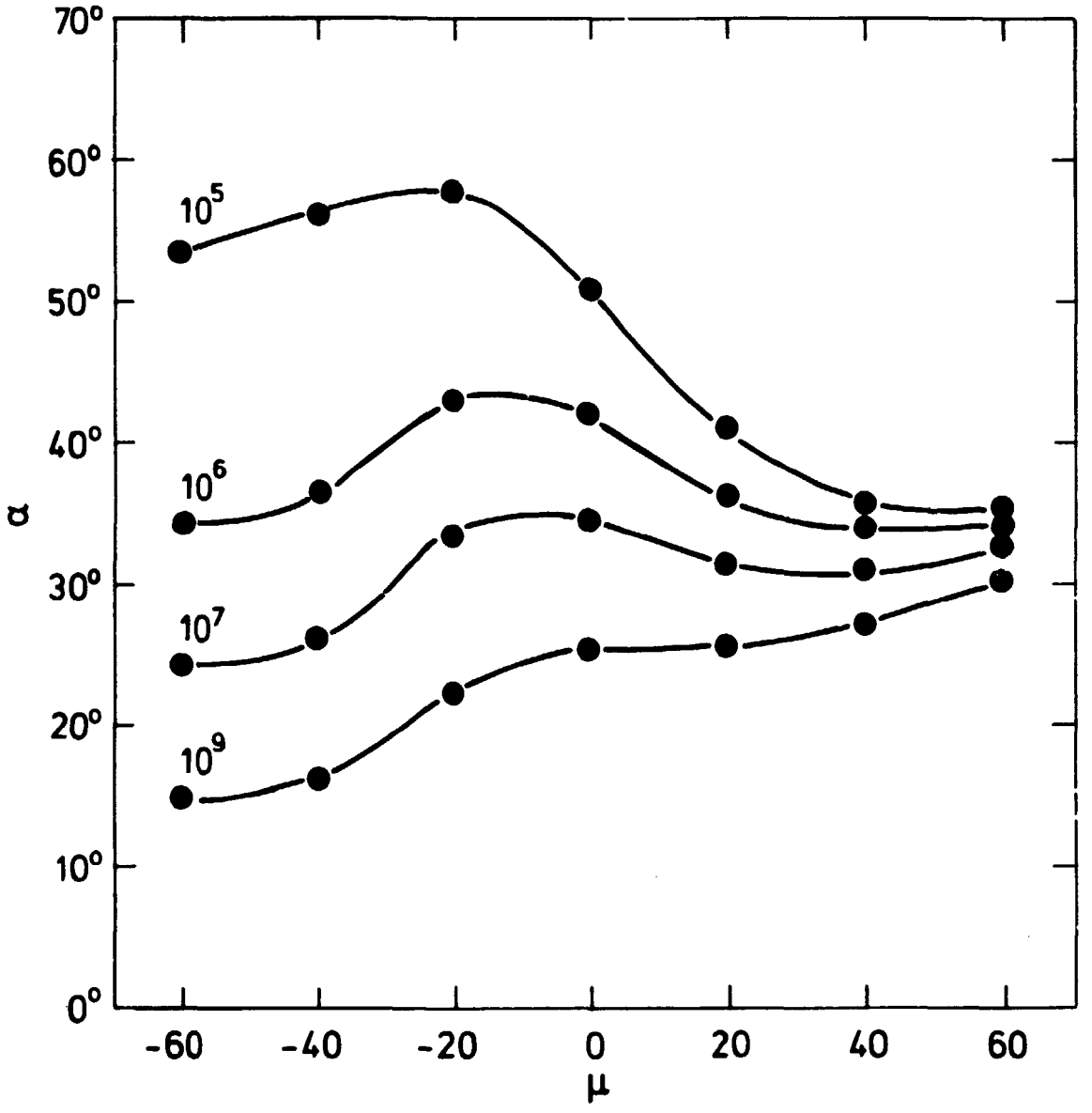

Fig. 5.7. The cross isobaric angle α as a function of stability for different Rossby numbers. Based on O'Neill best-fit values of A and B (cf. 5.5).

Rossby numbers. It is also noticeable that while α generally decreases with increasing μ for the small Rossby number (= 10^5), except for a local maximum, α generally increases with increasing μ for the higher Rossby numbers.

As A(μ) is only known poorly, and α is very sensitive to A, there exists considerable uncertainty in the α-values in Fig. 5.7 and the curves shall not be read off too minutely. But as

was the case for u_{*o}/G, the cross isobaric angle shows the expected Rossby number invariance at high values of μ. The strong dependence upon Ro for the low values of μ is also identical to that observed for u_{*o}/G, and, as in the former case, we expect α to become Rossby number invariant in the free convection limit with a value close to zero. When discussing differences in cross isobaric angle we will return to Fig. 5.7.

A change of surface roughness causes an alteration in surface stress, and thereby alters the stress distribution through the entire PBL. Because of this the cross isobaric angle also changes. According to different authors considerable downstream fetches are required before the return to equilibrium is establisned. Taylor (1969) investigated the problem of the return to equilibrium with a mixing length PBL-model and found that for both m = 0.1 and m = 10, the return to equilibrium was not reached before the downstream fetch, x, reached the value $10^8 z_{01}$. For a characteristic upstream roughness, $z_{01} \approx 10^{-2}$ m, the necessary downstream fetch required to establish equilibrium is thus of the order of 1000 km. True equilibrium of the PBL is therefore very rarely encountered over land surfaces.

The adjustment in friction velocity is characterized by an overshoot in the first few meters after the roughness change followed by a very slow return to equilibrium, which, for practical reasons, is completed at $x = 2 \cdot 10^6 z_{01}$. The adjustment in cross isobaric angle is quite different in that it is unaltered up to $x \approx 10^6 z_{01}$, followed by the transition to equilibrium over the next two decades. Half of the equilibrium turning angle was reached at $\sim 5 \cdot 10^6 z_{01}$ for both m = 0.1 and m = 10. For a characteristic $z_{01} \approx 10^{-2}$ m this corresponds to a downstream fetch at ≈ 50 km.

Jensen (1978) also treated the problem of establishing equilibrium in the surface stress after the roughness change. In the case of a water-land transition he found that at a downstream fetch, where the IBL has grown to PBL height (at x ~ 20 km), there still is an excess of ~ 20% in surface stress compared with the equilibrium value of u_{*o} determined from the

geostrophic drag law, Eq. (5.2.a). This result agrees well with those of Taylor.

The question of response time to a change in surface heat flux will be treated in Section 5.4.1.

From this short review of the variation of momentum flux and cross isobaric angle with roughness and stability, we see that we should be able to detect effects of roughness and/or stability in the Horsens fjord area provided a sufficiently detailed analysis of the measured data is made. This is especially true for wind speed changes caused by altered surface roughness as they require relatively short fetches. In Section 5.5 we will determine the equilibrium ratios of wind speeds over terrain with different roughness values. But first we will determine the equilibrium differences in cross isobaric angle due to differences in roughness or stability and possible effects of topography.

5.3. Equilibrium value of the difference in cross isobaric angle due to unequal surface roughness

In the preceding paragraph, we saw that the establishment of true equilibrium in the PBL after a change of roughness requires fetches so long that it rarely will exist over land areas. In our experimental data we do, however, observe significant differences in cross isobaric angle. There are several processes which can cause these changes. In this section we will determine the maximum change in cross isobaric angle caused by roughness change alone.

This could be done for fixed changes in Rossby number just by reading off values from Fig. 5.7, but it is possible to develop an analytical expression with the roughness change as independent variable. Let us suppose that we have two PBL's in equilibrium, with identical G and μ, but with different roughness values, z_{01} and z_{02}. The ratio of the cross isobaric angles is then, from Eq. (5.2.b):

$$\frac{\sin\alpha_2}{\sin\alpha_1} = \frac{(u_{*_o}/G)2}{(u_{*_o}/G)_1} \quad . \tag{5.5}$$

Using the explicit form of the geostrophic drag coefficent, Eq. 5.4, we get

$$\frac{\sin\alpha_2}{\sin\alpha_1} = \left[\frac{(\ln Ro_2)}{(\ln Ro_1)}\right]^{(\frac{\mu}{60}-1)} \quad . \tag{5.6}$$

Using the geometrically average Rossby number $\langle Ro\rangle \equiv (Ro_1 \cdot Ro_2)^{1/2}$ and $m = Ro_1/Ro_2$ we have that $Ro_1 = \langle Ro\rangle m^{1/2}$ and $Ro_2 = \langle Ro\rangle m^{-1/2}$. From the smallness of m compared with $\langle Ro\rangle$ we can expand the right-hand side of Eq. (5.6). The left-hand side is expanded by use of $\Delta\alpha \equiv \alpha_2 - \alpha_1$ and $\bar{\alpha} \equiv 1/2(\alpha_1 + \alpha_2)$. Expanding the right-hand side of (5.6) to first order leads to

$$\frac{\cos\bar{\alpha} \cdot \sin\frac{\Delta\alpha}{2}}{\sin\bar{\alpha} \cdot \cos\frac{\Delta\alpha}{2}} = \left|\frac{\mu}{60} - 1\right| \cdot \frac{\ln(m)}{2\ln\langle Ro\rangle} \quad ,$$

and by utilizing the condition that $\Delta\alpha$ be small, we get (in radians),

$$\Delta\alpha \approx \tan\bar{\alpha} \cdot \left|\frac{\mu}{60} - 1\right| (\ln\langle Ro\rangle)^{-1} \cdot \ln(m) \quad . \tag{5.7}$$

Apart from the dependence upon $\bar{\alpha}$, this expression is very simple. The change in cross isobaric angle is proportional to the logarithm of the roughness change, inversely proportional to the logarithm of the geometric average of the Rossby numbers and increases linearly with decreasing μ. The inclusion of $\bar{\alpha}$ alters the μ and Ro influence, but not drastically. This term can enter from the approximate relation

$$\sin\bar{\alpha} \approx \frac{A(\mu) \cdot E(\mu)}{k} \cdot (\ln\langle Ro\rangle)^{(\frac{\mu}{60}-1)} \quad ,$$

and we get for $\Delta\alpha$ (in degrees):

$$\Delta\alpha = C(\mu,\langle Ro\rangle) \cdot \log_{10} m \quad , \tag{5.8}$$

with

$$C(\mu,\langle Ro\rangle) \equiv 1.32 \cdot 10^2 \cdot$$

$$\left[\left[\frac{k}{A(\mu)\cdot E(\mu)} \cdot (\ln\langle Ro\rangle)^{(1-\frac{\mu}{60})}\right]^2 - 1\right]^{-1/2} \cdot$$

$$\left|\frac{\mu}{60} - 1\right| \cdot (\ln\langle Ro\rangle)^{-1} \; .$$

We calculated $C(\mu,\langle Ro\rangle)$ for different values of μ with $\langle Ro\rangle$ = $1.9 \cdot 10^7$, $3.3 \cdot 10^7$, and $5.0 \cdot 10^7$ corresponding to z_o = $3 \cdot 10^{-3}$ m and G = 7, 12, and 18 m/s ($f = 1.2 \cdot 10^{-4}$ s^{-1}). These values are listed in Table 5.1.

Table 5.1. Variation of the change in cross isobaric angle with μ and $\langle Ro\rangle$ for a roughness change m = 10 (see Eq. 5.8).

$\langle Ro\rangle$ / μ	$1.9 \cdot 10^7$	$3.3 \cdot 10^7$	$5.0 \cdot 10^7$
-60	10.6°	9.8°	9.3°
-40	8.5°	7.9°	7.6°
-20	8.0°	7.5°	7.2°
0	6.3°	6.0°	5.7°
+20	4.2°	4.0°	3.9°
+40	2.2°	2.2°	2.1°
+60	0.0°	0.0°	0.0°

In this limited range of geometrically averaged Rossby-numbers, the variation with $\langle Ro\rangle$ is negligible. For $\langle Ro\rangle = 3.3 \cdot 10^7$ the values of $\Delta\alpha$ against m are shown in Fig. 5.8 for different

μ values. Due to the influence of the $\bar{\alpha}$ term, the variation of $\Delta\alpha$ with μ is not strictly linear. But the nonlinearity is so small that for an ensemble the average $\Delta\alpha$ corresponds closely to the $\Delta\alpha$ at the average μ.

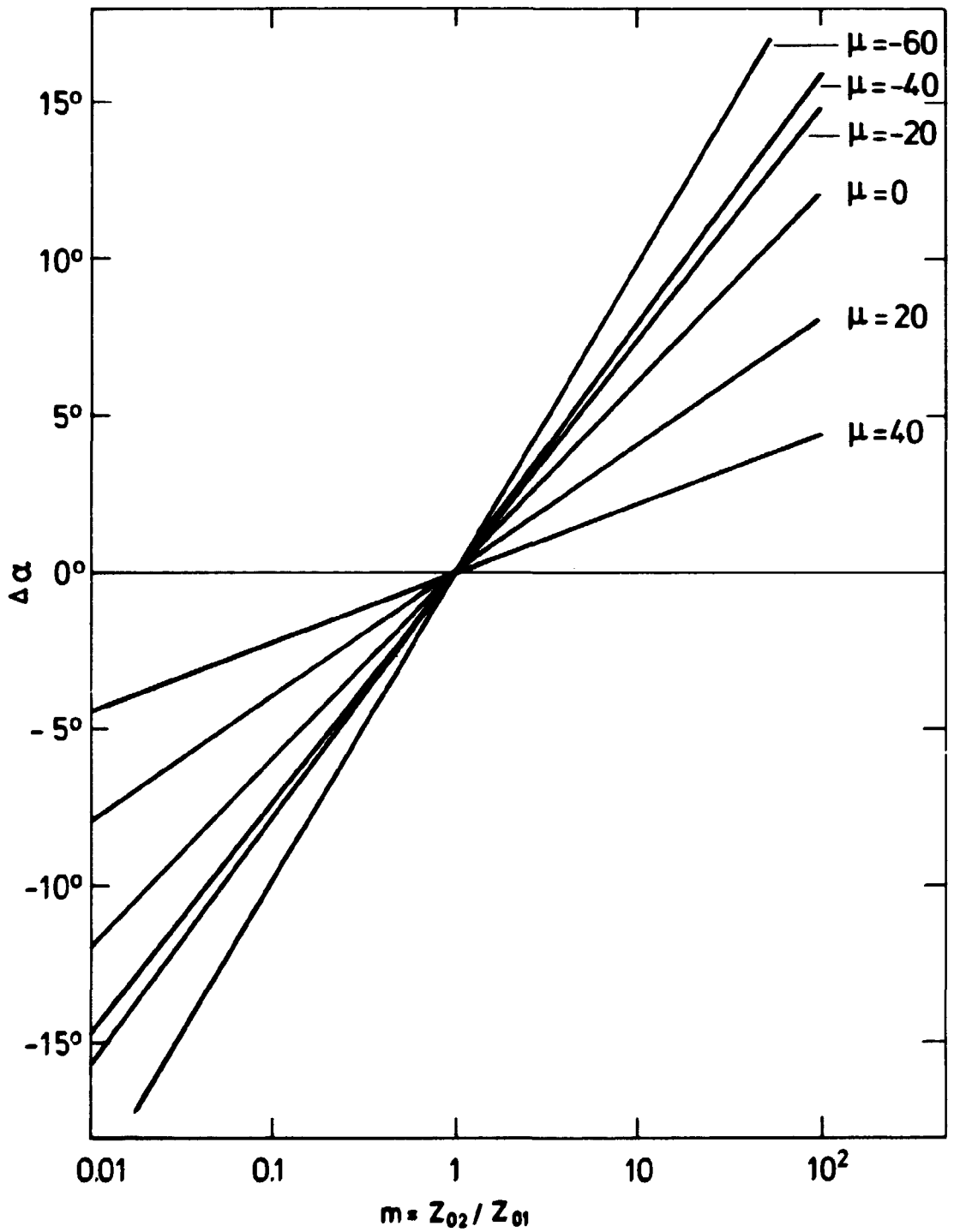

Fig. 5.8. Change in cross isobaric angle as a function of roughness change m. $\langle R_o \rangle = 3.3\ 10^7$ (see text).

As the average μ is close to neutral, and $\log_{10} m$ typically of order 1, we should expect the average values of $\Delta\alpha$ caused by roughness change alone to be in the vicinity of 6^{o}. This change is sufficient to be detected with an accurate instrumental set-up and a detailed analysis. But due to other processes that alter the wind direction, the effects of roughness change alone can easily be concealed. In the next paragraph we will look further into other processes which could be responsible for directional changes.

5.4. Changes in cross isobaric angle due to processes other than roughness change

Changes in roughness are usually accompanied by changes in other surface properties, such as albedo and heat capacity. It is therefore an idealization to consider roughness changes with unaltered μ. The inclusion of μ would, however, complicate matters considerably, but without clarifying the subject appreciably due to the inherent 3-dimensional nature of the flow in the Horsens fjord area.

Instead, we will make a semiquantitative estimate of the effects of varying μ keeping Ro constant. This estimate will be based on Fig. 5.7, where α was shown as a function of μ for different values of Ro.

The inhomogeneity of the area originating from differences in topographical heights are probably large enough to cause some changes of the flow pattern. We will develop a simple model, based on continuity considerations, to determine the changes in wind direction due to changing topographical height.

5.4.1. Differences in direction due to stability differences

The variation in α with μ can most easily be appreciated from Fig. 5.7. For all Rossby-numbers there is a local maximum for slightly unstable values of μ, but the local maximum is practically absent for Rossby-number 10^{9}. This local maximum can be

qualitatively understood as resulting from the Rosby-number invariance at both the stable and unstable limits, together with the increase in cross isobaric angle with increasing roughness at neutral stratification. But due to the uncertainty in the determination of A and B these curves are somewhat uncertain and must be considered with care.

However, even with this limitation we must conclude that moderate variations in μ can produce changes in α comparable with that of changing the roughness by one order of magnitude, i.e. on the order of 5^{o} for the Rossby-numbers encountered.

The determination of the difference in the average cross isobaric angle between two samples with different upstream surface thermal properties, is greatly complicated by the nonlinear dependence of α upon μ. Due to this we cannot use the expected average μ to determine an expected average α, but must know the distribution function of μ to determine the average cross isobaric angle. Such distributions are unavailable, however, but their effect upon the average α can be illustrated by the fact that the greater the relative frequency of the μ-distribution at the μ-value, where α has a local maximum, the greater is the average value of α, provided that the distributions have the same mean.

The most obvious case of different μ distributions would be that of trajectories of the order of 100 km over land and water. Because of water's larger heat capacity, diurnal effects there would be greatly diminshed. If we consider the radiative effects only, the μ-distribution would have its peak close to $\mu = 0$, while the land distributions would be flatter, that is, with a greater relative frequency of moderate-to-strong diabatic cases. In this case, the average cross isobaric angle for the above-water trajectories would be the greater, of the order $\sim 5^{o}$, compared with land. This is true provided the Rossby-number is unchanged. But the Rossby-number is approximately a factor of 10 smaller over land giving rise to the opposite effect, i.e. a greater average α for the land trajectories relative to water. The response time of step changes in surface heat flux is there-

fore decisive as to whether or not stability effects upon the cross isobaric angle can be detected. No satisfactory theory has yet dealt successfully with this problem, and we must therefore be satisfied with a semiquantitative estimate of the response time. This will be based on climatological tower data published by Petersen (1975). He reported the monthly average diurnal variation in directional shear from a 10-year time series from the Risø tower. As average data are close to barotropic the average geostrophic wind does not change with height; therefore, the data actually represent the time change in cross isobaric angle with height of the air masses being advected through the Risø tower at a fixed speed. This average diurnal change in cross isobaric angle is caused by the average diurnal variation in radiative balance at the surface. The heat flux changes associated are, on the average, of the same order as those experienced by an air mass which passes a water-land boundary, again in the average sense. The justification for this lies in the closeness of the water temperature in winter to the average daily maximum temperature, and the water temperature in summer to the average daily minimum temperature. It is therefore reasonable to estimate the rate of directional change associated with the heat flux changes originating from a water-land boundary by the rate of change of directional shear in the Risø tower. We will use the data from March published by Petersen (1975).

The vertical shear in average direction was close to constancy during the nighttime and daytime hours, respectively, and the change from one state to the other took place in a nearly linear fashion and lasted ~ 4.5 hours for the transition from stable (nighttime) to unstable (daytime) while the opposite lasted ~ 6 hours. The amplitude of the variation was 13^{o}. Due to the constancy of the geostrophic wind within the thin layer, we can, by a change of sign, replace direction, θ, by the cross isobaric angle, α, i.e. $\partial/\partial t(\partial\theta/\partial z) = -\partial/\partial t(\partial\alpha/\partial z)$, and we find for the night-to-day transition that $\partial/\partial t(\partial\alpha/\partial z) \simeq 0.03$ deg m^{-1} h^{-1} while for the day-to-night transition the value is $\simeq -0.02$ deg m^{-1} h^{-1}.

The linear response is not in accordance with the α variation shown in Fig. 5.7, where the α-transiton from one diabatic state to the other goes through a local maximum at the neutral point. A possible explanation for that could be that during a transition from one diabatic state to the opposite one, the neutral state will not be truly established and the local maximum in α for μ close to zero would then not show up in $\partial/\partial t(\partial\alpha/\partial z)$.

The transitions with which we are concerned are water ↔ land. The average associated stability changes are as follows:

	Day	Night
water → land:	neutral → unstable	neutral → stable
land → water:	unstable → neutral	stable → neutral

The contribution to the average stability changes is different for the seasons. For the daytime cases the contributions to the heat flux changes come mainly from the spring and summer seasons while for the nighttime cases, the heat flux changes are mainly associated with the fall and winter seasons. The reason for this lies in the previously mentioned point that the water temperature in winter is close to the average daily maximum temperature while the water temperature in summer is close to the average daily minimum temperature.

Because of the absence of the true neutral state in the diurnal variation of directional shear, the tower data will supply a lower bound estimate of the rate of directional change associated with water ↔ land trajectories during daytime conditions, while they will produce an erroneous estimate of the rate of directional change for water ↔ land trajectories during nighttime conditions (cf. Fig. 5.7). We can therefore estimate only the rate of directional change for the neutral ↔ unstable transitions. We will assume the rate of directional change in the case of neutral ↔ stable transitions to be of the same magnitude.

The diurnal variation in the shear angle is identical to the shear in diurnal variation of the cross isobaric angle. Above some height, δ, we do not expect any appreciable diurnal variation of α in the average sense, i.e. $\partial\alpha/\partial t_{|z=\delta} = 0$. We will assume that the height variation in $\partial\alpha/\partial t$ is roughly linear. The local change corresponds to advective changes, i.e. $\partial t = U^{-1}\,\partial s$, where U is the advection speed and s the distance. Combining this we get

$$\left(\frac{\partial\alpha}{\partial s}\right)_{z\sim 0} = -\delta U^{-1}\left(\frac{\partial}{\partial t}\frac{\partial\alpha}{\partial z}\right) \quad . \tag{5.9}$$

A reasonable value of δ is ~ 500 m, and for U = 10 m/s we then have, from Eq. 5.9 with $\partial/\partial t\ \partial\alpha/\partial z = 0.03$ deg m^{-1} h^{-1},

$$\left(\frac{\partial\alpha}{\partial s}\right)_{z\sim 0} = \pm\ 0.4 \text{ deg km}^{-1} \quad ,$$

where the plus sign is associated with land-to-water transitions and the minus sign with water-to-land transitions, both during average daytime conditions.

We should, therefore, be able to detect a change in cross isobaric angle due to heat flux changes with a fetch of only 5-10 km. There is then a considerable downstream distance of the order 50 km, where the effect of heat flux change on α is detectable, but where the opposing effect of the usually associated roughness change is as yet unestablished.

5.4.2. Change of direction due to chanelling

Chanelling is in general the tendency of an airflow to be aligned with larger scale topographical features such as steep sided valleys or mountains. The differences in topographical height in the Horsens fjord area are not, however, of a magnitude capable of aligning the flow in a general direction. But, on the other hand, the height differences up to ~ 100 m, could possibly cause

changes in the wind direction up to some distance downstream. In the following we will develop a simple model of the directional changes due to the momentum deficit/surplus in case of offslope/onslope flow.

We will consider straight contour lines of infinite length. The coordinate system we will use is shown in Fig. 5.9.a. The angle β is the wind direction upstream of the slope, and relative to the direction of the contour lines. β is positive counter clock-

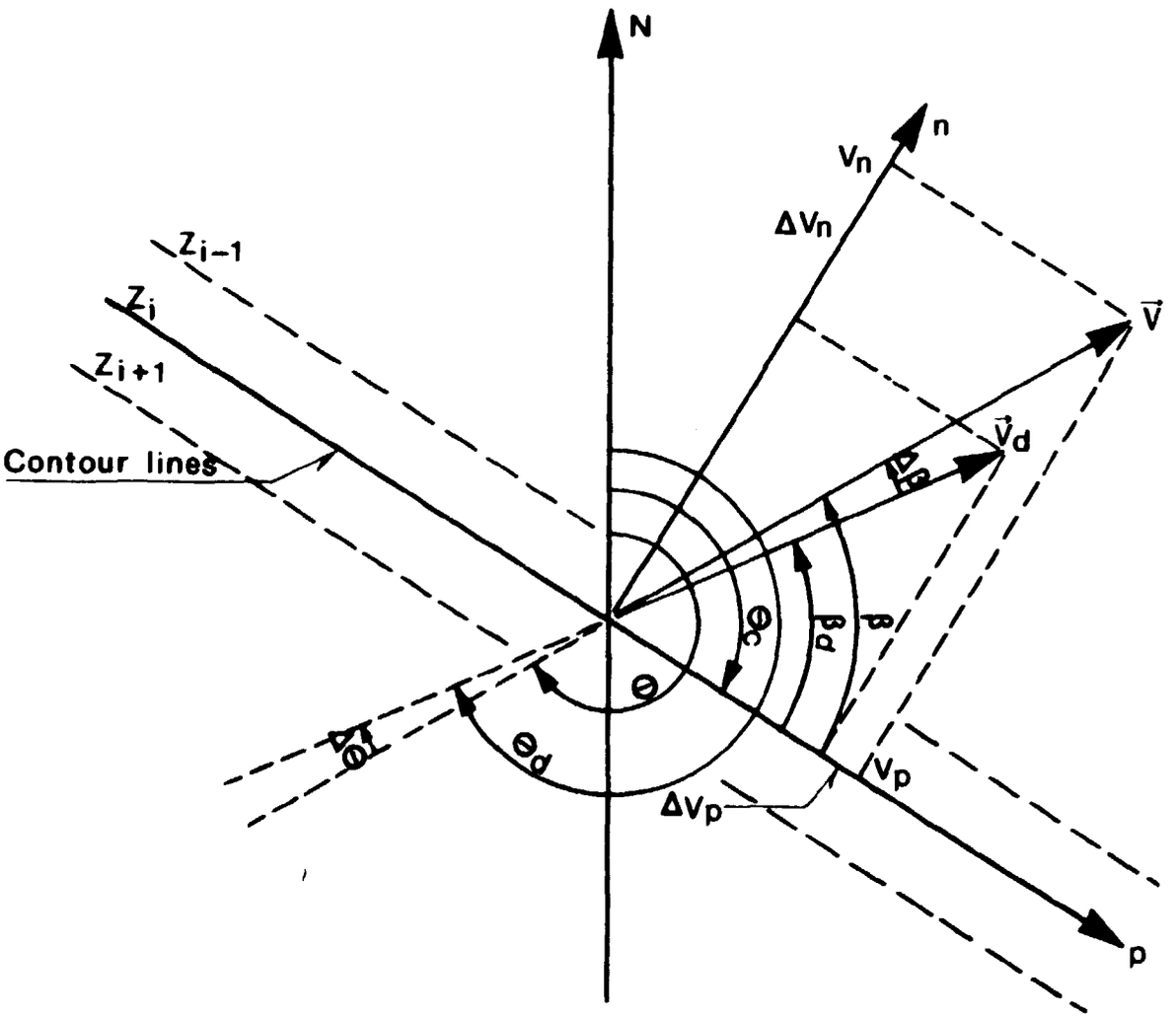

Fig. 5.9.a. The (p,n) coordinate system defined relative to the contour lines. Unsubscripted values refer to upstream conditions, subscript "d" refers to downstream values. Angles β are relative to the (p,n) coordinate system, θ are standard meteorological directions, and θ_c is the direction of the contour lines with larger heights to the left.

wise, and its relation to the standard direction θ is $\beta = \pi - (\theta - \theta_c)$, where θ_c is the direction of the contour lines, defined as the wind direction parallel to the contour lines with their higher values to the left. In case of flow parallel to the slope, i.e. $\beta = 0$ or $\beta = \pi$, we will assume the flow to be unperturbed. For $0 < \beta < \pi$ we have offslope flow, and for $\pi < \beta < 2\pi$ we have onslope flow. Figure 5.9.b shows a simple geometry of a sloping terrain. Downstream of the slope the velocity will be changed up to some height λ. The integrated effect of this velocity change from the surface up to the height λ corresponds to the momentum, ΔM, due to the component of the wind profile from 0 to slope height H perpendicular to the contour lines. In case of offslope flow this profile is hypothetical. We will not, however, introduce grave errors by setting $\Delta M = -H \cdot V \cdot \sin\beta$, where V is the wind speed, and β the direction, close to the surface (eg. the 10 m wind) upstream of the slope. We do not expect the effect of changed topography to propagate upstream in the flow.

λ is the depth, relative to the surface, of the layer with an altered velocity. This depth increases in some way with the downstream distance from the slope, and must be quite strongly dependent upon the thermal stability of the air mass. The height H must also play a part, especially for offslope flow, where H for obvious reasons is the initial value of λ. At present, however, we will not be concerned with the dependence of λ upon downstream distance as we will use λ as an independent variable.

We define the perturbation of each wind component as the downstream value minus the upstream value, always at the same height above the surface. As the absolute value of the wind components decrease downstream for offslope flow ($0 < \beta < \pi$), and increase downstream for onslope flow ($\pi < \beta < 2\pi$), we have the following signs for the perturbations in the wind components:

$$\Delta V_p: \begin{cases} < 0 \text{ for } 0 < \beta < \pi/2 \text{ and } \pi < \beta < 3\pi/2 \ . \\ = 0 \text{ for } \beta = 0,\ \pi/2,\ \pi,\ 3\pi/2 \ . \\ > 0 \text{ for } \pi/2 < \beta < \pi \text{ and } 3\pi/2 < \beta < 2\pi \ . \end{cases}$$

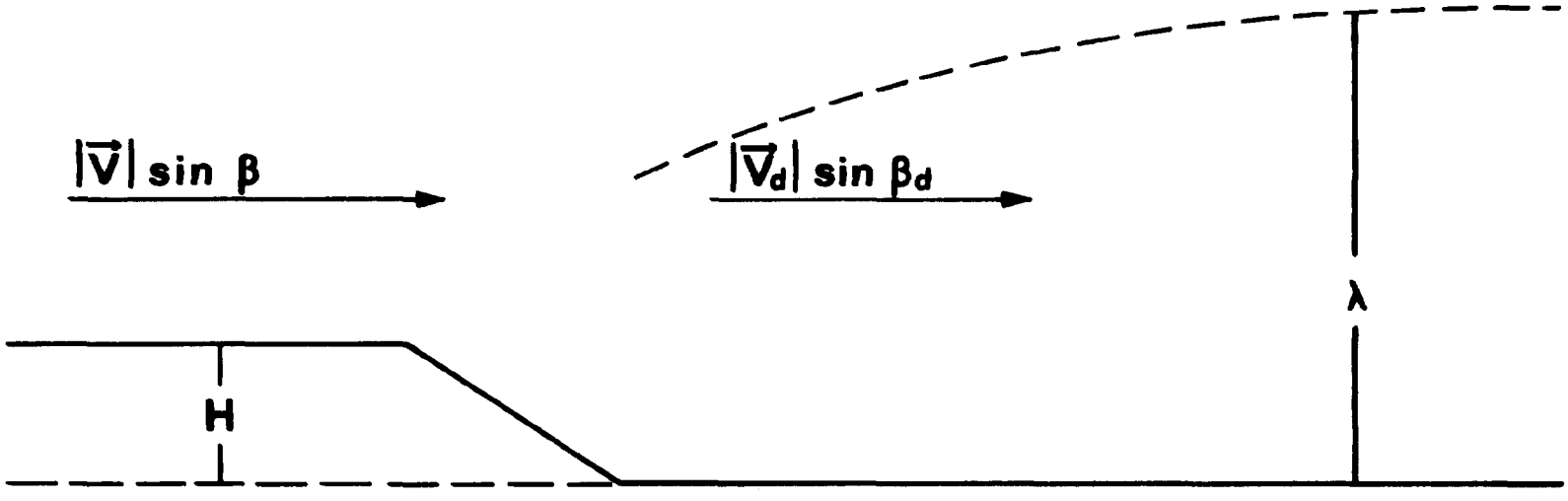

Fig. 5.9.b. The component of the flow perpendicular to the contours, here for offslope flow. H is the height difference between the two areas with fairly uniform height, and λ is the depth of the layer with perturbed wind velocities.

$$\Delta V_n: \begin{cases} < 0 \text{ for } 0 < \beta < \pi \text{ and } \pi < \beta < 2\pi \\ = 0 \text{ for } \beta = 0, \pi \quad . \end{cases}$$

The contribution from the change of each component to the momentum change, ΔM, is negative for $0 < \beta < \pi$ and positive for $\pi < \beta < 2\pi$. We thus hold the following equation for the momentum balance

$$-H \cdot V \cdot \sin\beta = \int_0^{\lambda} [\text{sign}(\cos\beta)\Delta V_p(\beta,z) + \text{sign}(\sin\beta)\Delta V_n(\beta,z)]dz$$

We now assume ΔV_j, $j = p,n$, to vary linearly with height, being nil at $z = \lambda$, and having its maximum absolute value $\Delta V_j)_s$ close to the surface. From the momentum balance equation above we obtain,

$$-\frac{2H}{\lambda}\sin\beta = \text{sign}(\cos\beta) \cdot s_p(\beta) + \text{sign}(\sin\beta) \cdot s_n(\beta) \quad , \qquad (5.10)$$

where we have defined the perturbation functions

$$s_p(\beta) \equiv \frac{\Delta V_p)_s}{V} \quad , \text{ and} \quad s_n(\beta) \equiv \frac{\Delta V_n)_s}{V} \quad .$$

From (5.10) and the sign conventions above, we hold the following special values of s_n and s_p:

a. $s_n(\ell \cdot \pi) = s_p(\ell \cdot \pi) = 0, \quad \ell = 0,1.$

b. $$\begin{cases} s_n(\ell \cdot \pi/2) = -2H/\lambda \ , \ \ell = 1,3 \quad . \\ s_p(\ell \cdot \pi/2) = 0, \ \ell = 1,3 \quad . \end{cases}$$

From symmetry considerations we further expect $|\Delta V_p(\ell \cdot \pi/4)| = |\Delta V_n(\ell \cdot \pi/4)|$, $\ell = 1,3,5,7$. This gives further the following special values:

$$c. \quad s_n(\ell\cdot\pi/4) = -H/\lambda \cdot \sqrt{2/2} \quad , \quad \ell = 1,3,5,7.$$

$$d. \begin{cases} s_p(\ell\cdot\pi/4) = -H/\lambda \cdot \sqrt{2/2} \quad , \quad \ell = 1,5. \\ s_n(\ell\cdot\pi/4) = H/\lambda \cdot \sqrt{2/2} \quad , \quad \ell = 3,7. \end{cases}$$

Functions satisfying these special values are,

$$\begin{aligned} s_n(\beta) &= -2H/\lambda\cdot|\sin^3\beta| \\ s_p(\beta) &= -2H/\lambda\cdot\sin\beta\cdot\cos\beta\cdot|\cos\beta| \quad . \end{aligned} \tag{5.11}$$

We see no reason not to use these functions as interpolators for the perturbation functions. The momentum partioning functions are then, according to (5.10), $\text{sign}(\cos\beta)\cdot s_p(\beta)$ and $\text{sign}(\sin)\beta)\cdot s_n(\beta)$, and they are, together with $\Delta M/V(\beta)$, shown in Fig. 5.9.c.

As the perturbations in the wind components were defined relative to the same height above the surface, we have

$$\Delta V_n)_s = V_d\cdot\sin\beta_d - V\cdot\sin\beta$$

$$\Delta V_p)_s = V_d\cdot\cos\beta d - V\cdot\cos\beta \quad ,$$

where V_d and β_d are speed and direction of the wind downstream of, and off, the slope. Defining $\Delta\beta = \beta_d - \beta$ as the perturbation of the wind direction close to the surface we have

$$\tan(\Delta\beta+\beta) = \frac{\sin\beta+s_n(\beta)}{\cos\beta+s_p(\beta)} \quad .$$

This equation gives $\Delta\beta$ as a function of β, using the expressions (5.11) for the perturbation functions s_n and s_p, which are functions of β for fixed parameters λ and H. For the characteristic height difference H we will use 60 m. For the depth of the layer

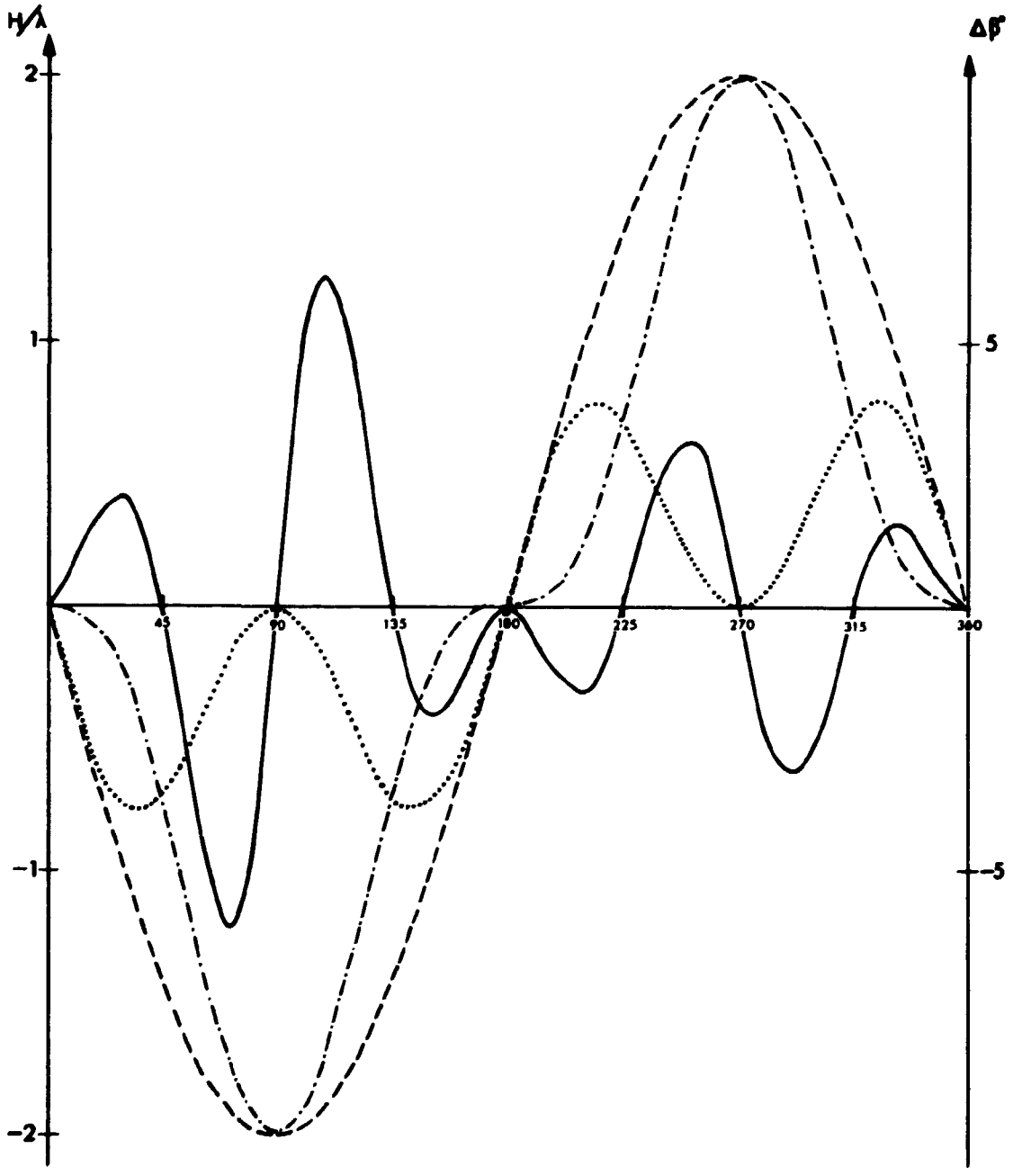

Fig. 5.9.c. The relative momentum deficit/surplus, as multipla of H/λ and as function of β, $\frac{\Delta M}{\nabla}(\beta)$: ---; the momentum partitioning functions, $\text{sign}(\cos\beta)\cdot s(\beta)$: ..... , $\text{sign}(\sin(\beta))\cdot s_n(\beta)$: -·-·- . The values of $\Delta\beta$ derived from (5.12) with H = 60 m and λ = 300 m: ———, (scale to the right).

Table 5.2. The turning angle $\Delta\beta$ as a function of β for different values of λ and with fixed H = 60 m.

Case: Offslope flow with H = 60 m.
List of $\Delta\beta$ (in degrees) for:

λ =	200	300	400	500	750	1000	1250	1500
β = 0	0.0	0.0	0.0	0.0	0.0	0.0	0.0	0.0
β = 10	0.9	0.6	0.4	0.3	0.2	0.2	0.1	0.1
β = 20	2.7	1.7	1.2	1.0	0.6	0.5	0.4	0.3
β = 30	3.5	1.2	1.5	1.2	0.8	0.6	0.5	0.4
β = 40	1.9	1.1	0.8	0.6	0.4	0.3	0.2	0.2
β = 50	-2.4	1.1	0.8	-0.7	-0.5	-0.3	-0.3	-0.2
β = 60	-7.8	-4.3	-3.0	-2.2	-1.4	-1.0	-0.8	-0.7
β = 70	-12.0	-6.1	-4.1	-3.1	-1.9	-1.4	-1.1	-0.9
β = 80	-10.7	-5.0	-3.3	-2.4	-1.5	-1.1	-0.8	-0.7
β = 90	0.0	0.0	0.0	0.0	0.0	0.0	0.0	0.0
β = 100	10.7	5.0	3.3	2.4	1.5	1.1	0.8	0.7
β = 110	12.0	6.1	4.1	3.1	1.9	1.4	1.1	0.9
β = 120	7.8	4.3	3.0	2.2	1.4	1.0	0.8	0.7
β = 130	2.4	1.4	1.0	0.7	0.5	0.3	0.3	0.2
β = 140	-1.9	-1.1	-0.8	-0.6	-0.4	-0.3	-0.2	-0.2
β = 150	-3.5	-2.1	-1.5	-1.2	-0.8	-0.6	-0.5	-0.4
β = 160	-2.7	-1.7	-1.2	-1.0	-0.6	-0.5	-0.4	-0.3
β = 170	-0.9	-0.6	-0.4	-0.3	-0.2	-0.2	-0.1	-0.1
β = 180	0.0	0.0	0.0	0.0	0.0	0.0	0.0	0.0

Case: Onslope flow with H = 60 m.
List of $\Delta\beta$ (in degrees) for:

λ =	200	300	400	500	750	1000	1250	1500
β = 180	0.0	0.0	0.0	0.0	0.0	0.0	0.0	0.0
β = 190	-0.8	-0.5	-0.4	-0.3	-0.2	-0.2	-0.1	-0.1
β = 200	-1.9	-1.3	-1.0	-0.8	-0.6	-0.4	-0.4	-0.3
β = 210	-2.2	-1.6	-1.2	-1.0	-0.7	-0.5	-0.4	-0.4
β = 220	-1.1	-0.8	-0.6	-0.5	-0.3	-0.3	-0.2	-0.2
β = 230	1.2	0.9	0.7	0.6	0.4	0.3	0.2	0.2
β = 240	3.4	2.5	2.0	1.6	1.1	0.9	0.7	0.6
β = 250	4.2	3.1	2.5	2.1	1.5	1.1	0.9	0.9
β = 260	3.0	2.3	1.8	1.5	1.1	0.8	0.7	0.6
β = 270	0.0	0.0	0.0	0.0	0.0	0.0	0.0	0.0
β = 280	-3.0	-2.3	-1.8	-1.5	-1.1	-0.8	-0.7	-0.6
β = 290	-4.2	-3.1	-2.5	-2.1	-1.5	-1.1	-0.9	-0.8
β = 300	-3.4	-2.5	-2.0	-1.6	-1.1	-0.9	-0.7	-0.6
β = 310	-1.2	-0.9	-0.7	-0.6	-0.4	-0.3	-0.2	-0.2
β = 320	1.1	0.8	0.6	0.5	0.3	0.3	0.2	0.2
β = 330	2.2	1.6	1.2	1.0	0.7	0.5	0.4	0.4
β = 340	1.9	1.3	1.0	0.8	0.6	0.4	0.4	0.3
β = 350	0.8	0.5	0.4	0.3	0.2	0.2	0.1	0.1
β = 360	0.0	0.0	0.0	0.0	0.0	0.0	0.0	0.0

with perturbed velocities, λ, we shall use different values ranging from 300 to 1500 m. The values of $\Delta\beta$ for these different parameter values are listed in Table 5.2. For λ =300 m, the results are shown graphically in Fig. 5.9.c. Recalling that $\beta = \pi-(\theta-\theta_c)$, we hold $\Delta\beta = \theta-\theta_d$, i.e. the unperturbed direction minus the perturbed direction.

Due to purely geometrical reasons, the perturbation of the direction is greater for offslope flow than for onslope flow. We should, therefore, primarily be able to detect possible changes of direction due to topography in case of flow from higher to lower height (offslope flow).

Without experimental evidence it is impossible to judge the ability of the model to predict the correct change of direction, if any, of a flow which passes a change of height of the surface. The crucial point here is a sufficiently low value of λ downstream, or in general, a sufficiently high value of the ratio H/λ. We shall return to this point when we discuss the observed differences in direction (Section 6.5).

5.5. Equilibrium ratios between wind speeds over terrains with different degrees of roughness

Decreasing surface roughness causes the surface Rossby number to increase whereby a decrease in equilibrium friction velocity (shear stress) takes place. This change requires considerable fetches over the new roughness before an equilibrium value is established. As previously cited from Taylor (1968), the equilibrium in friction velocity was not established before the fetch reached $2\cdot10^6 z_{01}$, i.e. fetches of the order 20 km.

The immediate effect of a decrease in z_o is therefore an excess of momentum due to the decrease of friction, which shows up in the IBL as an increased wind speed. Further downstream, the decrease in $u*_o$ causes the acceleration to decrease until the wind speed reaches its new equilibrium value.

An increase in surface roughness, on the other hand, causes a decrease in the Rossby number, and therefore an increase in the equilibrium value of the friction velocity (shear stress). But due to the increased friction a momentum deficit is the immidiate effect, and this shows up as a velocity decrease within the IBL. Further downstream the velocity increases due to the increase in u_{*o}.

The ratios between equilibrium values of the wind speed can be determined for the neutral case by a combination of SBL and PBL theory. We will use the approximate form of the neutral drag law, Jensen (1978), i.e.

$$\frac{u_{*o}}{G} = 0.5/\ln(Ro) \ ,$$

in combination with the logarithmic wind profile. This gives the following equilibrium value of the wind speed

$$\alpha(z) = \frac{\ln\frac{z}{z_o}}{2k \cdot \ln Ro} \cdot G \quad . \tag{5.12}$$

Except for the small influence of G upon the denominator, the surface wind is proportional to the geostrophic wind.

The equilibrium ratio between wind speeds in the neutral case for equal geostrophic winds is then

$$\frac{\bar{u}_2(z)}{\bar{u}_1(z)} = \frac{\ln\frac{z}{z_{02}} \cdot \ln Ro_1}{\ln\frac{z}{z_{01}} \cdot \ln Ro_2} \quad .$$

Using the geometric average of the roughness, $\langle z_0 \rangle$, and neglecting second- and higher-order terms in the expansion of $\ln(1+x)$ gives the following expression for the logarithm of the ratio,

$$\ln\frac{u_2(z)}{u_1(z)} = \left(\frac{1}{\ln\langle Ro\rangle} - \frac{1}{\ln\frac{z}{\langle z_o\rangle}}\right) \cdot \ln m \quad . \tag{5.13}$$

As usual, index 2 refers to downstream and 1 to upstream conditions. <Ro> is the geometric average of the upstream and downstream Rossby numbers and $m \equiv z_{02}/z_{01}$.

Due to the large magnitude of <Ro>, in practice (5.13) is independent of G for a wide range. From (5.13) it may also be seen that the equilibrium ratio decreases with increasing measuring height in the SBL. In Fig. 5.10 the equilibrium growth ratio for z = 17.5 m is shown with $\langle z_0 \rangle = 3 \cdot 10^{-3}$ m and G = 12 m/s. For a typical land-water roughness change with m = 0.1 we find an equilibrium speed ratio at approximately 1.15. In the next chapter we will consider some examples of measured speed ratios.

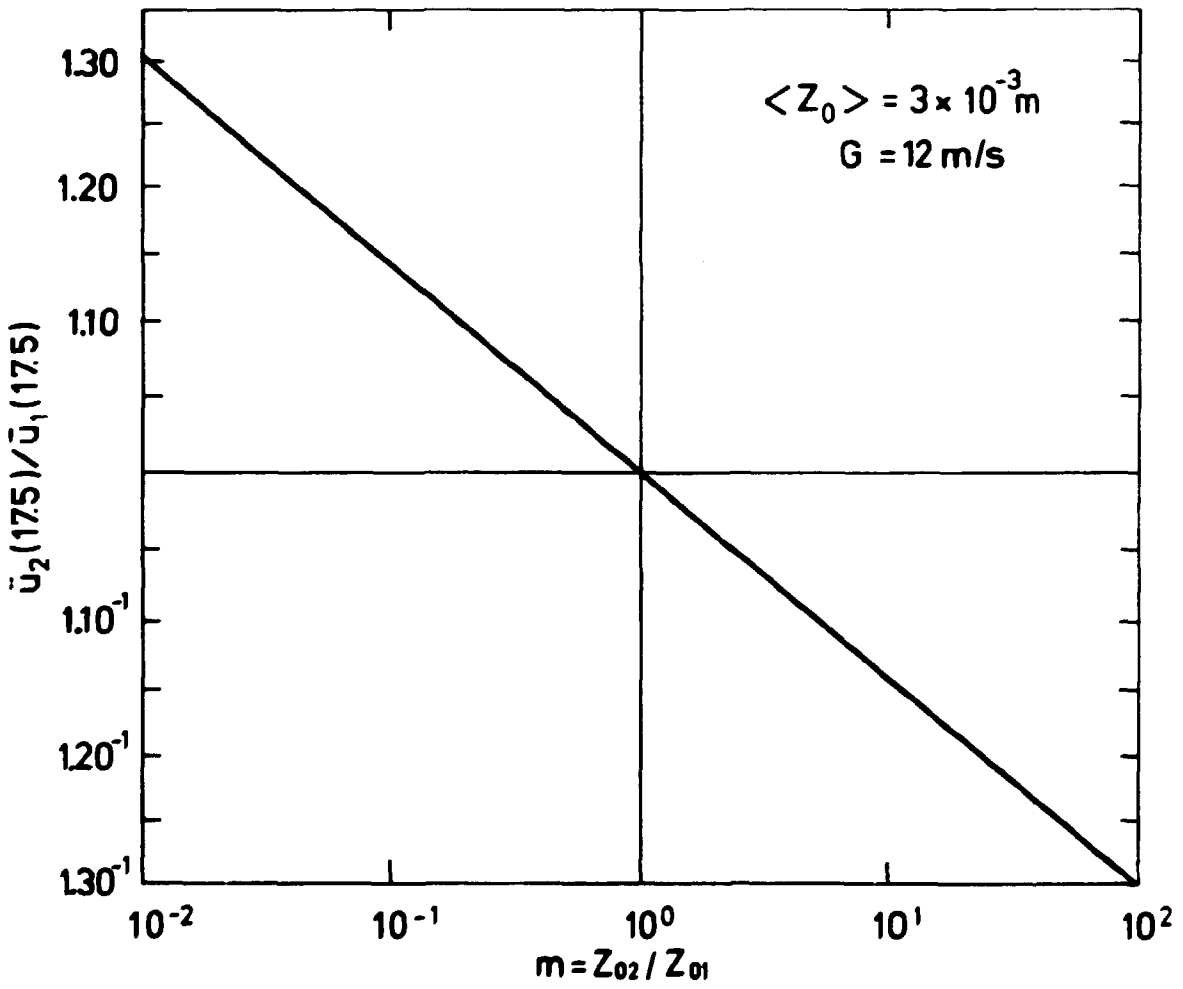

Fig. 5.10. Equilibrium values of wind speed ratios at 17.5 m as a function of roughness change m, Eq. (5.13).

5.6. Change of terrain roughness for intermediate fetches

In the former sections of this chapter we discussed various aspects of the flow response, when the surface conditions changed, and while some knowledge is available, obviously much information is still needed before a reasonably complete description can be made.

We know quite a lot about the flow response for very short fetches, up to 200 meters, say (see Section 5.1). We also know a good deal about the differences in flow conditions over two surfaces when the flow is in requilibrium with both (see Section 5.5). If we imagine a step change in surface conditions, this means that we can predict the flow behaviour for very long fetches. As discussed in Section 5.2, however, we have very little knowledge about how the flow approaches equilibrium for intermediate fetches.

In this section a simple 2-dimensional model pertaining to such fetches shall be discussed. We will consider a simple change of roughness situation, as depicted in Fig. 5.1. Our mesoscale model will be based on a simple surface layer model originally due to Miyake and described in Panofsky (1973) and Jensen (1978). We shall confine ourselves to neutral stability.

The height of the interface between the old and the new boundary layer, h, grows as

$$\frac{dh}{dt} = \bar{u}(h)\frac{dh}{dx} = A\sigma_w, \qquad (5.14)$$

where x is the fetch, $\bar{u}$ the mean velocity, and the entrainment velocity is considered proportional to the standard deviation of the vertical velocity, σ_w. A is a constant of order unity.

The variables $\bar{u}$ and σ_w are presumed to vary with height, z, as in the equilibrium boundary layer

$$\bar{u}(z) = \frac{u_{*o}}{k}\left(\ln\frac{z}{z_o} - 2\frac{z}{H}\right) \qquad (5.15)$$

$$\frac{\sigma_w}{u_{*o}} = \frac{\sigma_{wo}}{u_{*o}}\left(1 - \frac{z}{H}\right)^2 \quad . \tag{5.16}$$

Equation (5.15) is the simplest realistic extrapolation of the surface layer model in (4.3) for neutral stability. Note that (5.15) is consistent with (5.1 a) for z=H and B(0) = 2. H is the scale height, u_{*o}/f. Equation (5.16) is a simple fit to the model results by Wyngaard et al. (1974) (see Fig. 5.11). This figure also indicates that (5.15) and (5.16) show some deviations

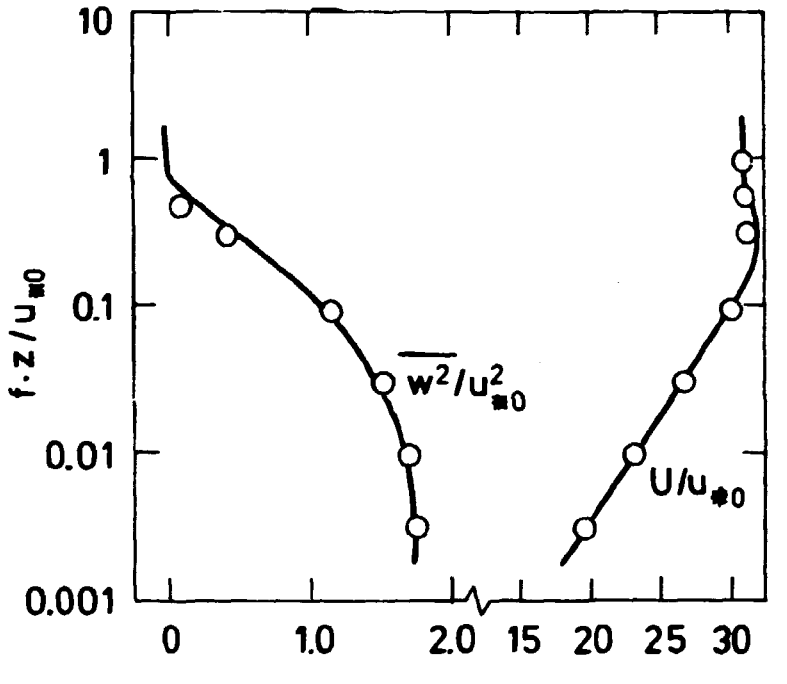

Fig. 5.11. Mean wind and turbulence profiles, neutral case, plotted against a logarithmic height scale (Wyngaard et al. (1974)). The circles show the expressions in (5.15) and (5.16), which are seen to fit the curves excellently for $zf/u_{*o} < 0.7$.

from the curves of Wyngaard et al. (1974) at the top of the boundary layer. For simplicity, however, we shall satisfy ourselves with these two equations.

By means of (5.15) and (5.16) we can integrate (5.14) to read

$$C\frac{x}{z_o} - 1 = \frac{h/z_o}{1-h/H}\left(\left(\ln\frac{h}{z_o} - 1\right) - \left[1 + \frac{H}{h}\left(1 - \frac{h}{H}\right)\ln\left(1 - \frac{h}{H}\right)\right]\right) , \quad (5.17)$$

where C is a constant of order unity. Without much loss of accuracy the terms in the square bracket can be replaced by h/H, with a maximum deviation of 0.2 for h/H ≅ 0.7.

The corresponding surface layer model is obtained by letting $H \to \infty$. Within the surface layer this model is known to work well provided one uses the z_o-value pertaining to the rougher surface (Panofsky (1973), and Jensen (1978)). It therefore seems logical in (5.17) to use both z_o and H pertaining to the rough surface, at least for the transition from smooth to rough. Therefore we shall discuss this case first.

As for the surface layer model the ratio between the surface stresses is found by matching the two velocity profiles at h(x), i.e. using the requirement that $u_1(h(x)) = u_2(h(x))$. However, in the present model we have two cases (see Fig. 5.12). In the first the internal boundary layer has not yet grown through the smooth boundary layer so both u_1, and u_2 are functions of h(x). In the second case $h > H_1$ and thus $u_1(h(x)) = U_{g1}$. Using the matching condition to find the ratio between the surface stresses we get from (5.15):

$$\frac{u_{*o2}}{u_{*o1}} = \frac{\ln\frac{h(x)}{z_{o1}} - 2\frac{h(x)}{H_1}}{\ln\frac{h(x)}{z_{o2}} - 2\frac{h(x)}{H_2}} \quad \text{for } h(x) \leq H_1 \quad , \quad (5.18)$$

and

$$\frac{u_{*o2}}{u_{*o1}} = \frac{u_2(h(x))}{U_{g1}} \cdot \frac{\left(\ln\frac{H_1}{z_{o1}} - 2\right)}{\left(\ln\frac{h(x)}{z_{o2}} - 2\frac{h(x)}{H_2}\right)} \quad \text{for } H_1 < h(x) \leq H_2, \quad (5.19)$$

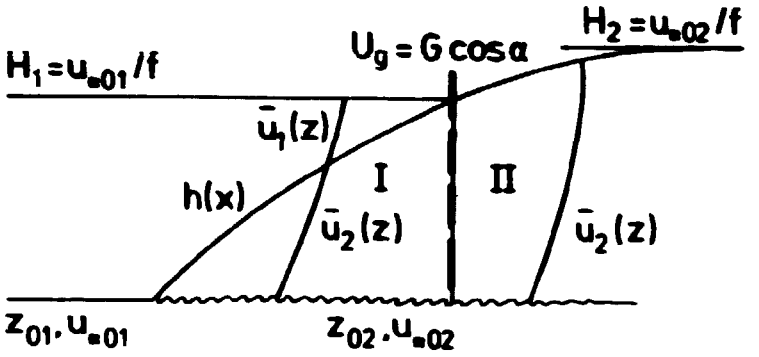

Fig. 5.12. The growth of an internal boundary layer in a two-dimensional atmospheric boundary layer and for the smooth-to-rough transition. In zone I the internal boundary layer grows against the smooth boundary layer, while in zone II it grows directly against the geostrophic wind. The figure shows the two different matching situations.

where we in (5.19) have retained the matching ratio $(u_2(h(x))/U_{g1})$. In the ideal 2-dimensional case this ratio is equal to one.

However, for $x \to \infty$ we have that $u_2(h(x)) \to U_{g2}$, and due to the turning of wind because of altered surface roughness we have $U_{g1} \neq U_{g2}$.

It is not surprising that a 2-dimensional model cannot cope with a 3-dimensional problem. In a 3-D model the velocities should have been matched vectorially, i.e. $(u_1^2(h(x))+v_1^2(h(x)))^{1/2} = (u_2^2(h(x))+v_2^2(h(x)))^{1/2}$. Such a model is extremely complicated compared to the present and is beyond the scope of this work. We found, however, that the present model describes differences in velocities surprisingly well (Chapter 6) provided we assure the correct limit values for $x \to \infty$ in (5.19). This was done by taking the turning of the wind into consideration, somewhat artificially, by setting $u_2(h(x)) = G\cos\alpha(x)$, where $\alpha(x)$ is the cross isobaric angle with the limit α_2 for $x \to \infty$. Eq. (5.19) was therefore rewritten to read:

$$\frac{u_{*o2}}{u_{*o1}} = \frac{\cos\alpha(x)}{\cos\alpha_1} \frac{\left(\ln\frac{H_1}{z_{o1}} - 2\right)}{\left(\ln\frac{h(x)}{z_{o2}} - 2\frac{h(x)}{H_2}\right)} , \qquad (5.20)$$

valid for $H_1 < h(x) \leq H_2$.

To establish an expression for $\alpha(x)$ we notice that Eq. (5.2 b) can be written

$$\sin\alpha = \frac{A(o)}{k} \frac{u_{*o}}{G} \simeq 12\, fH/G ,$$

which shows that $\alpha(x)$ will have the correct boundary values if it is determined as

$$\sin\alpha(x) = \begin{cases} 12fH_1/G \text{ for } h(x) < H_1 \\ 12fh(x)/G \text{ for } H_1 \leq h(x) \leq H_2 \end{cases} \qquad (5.21)$$

The principal working of the model, (5.14) through (5.20), is shown in Fig. 5.13, where the behaviour of the surface model also is depicted. The fact that we do not take the turning of the wind into account before h has grown above H, is qualitatively in accordance with the afore mentioned model results of Taylor (1969) in that the turning of the wind takes place last.

We shall use (5.18) to determine the value of C in (5.17). Theoretically C is found as $A \cdot (\sigma_w/u_{*o}) \cdot k \simeq A \cdot 0.44$, where the usual values for σ_w/u_{*o} and the von Karman constant, k, have been substituted. Panofsky (1973) recommends $C \simeq 0.6$, while Jensen (1978) uses $C = 1$. Figure 5.14 shows surface stress data obtained by Bradley (1968) for the smooth-to-rough and the rough-to-smooth transition. For the z_o-values given by Bradley we have further shown the predictions from (5.18) with $C = 0.5$ and $C = 1$. From this figure we conclude that $C = 0.5$ is too small, $C = 1$ is certainly usable, however, we think it appears to be a bit too large. We, therefore, have settled for $C = 0.9$

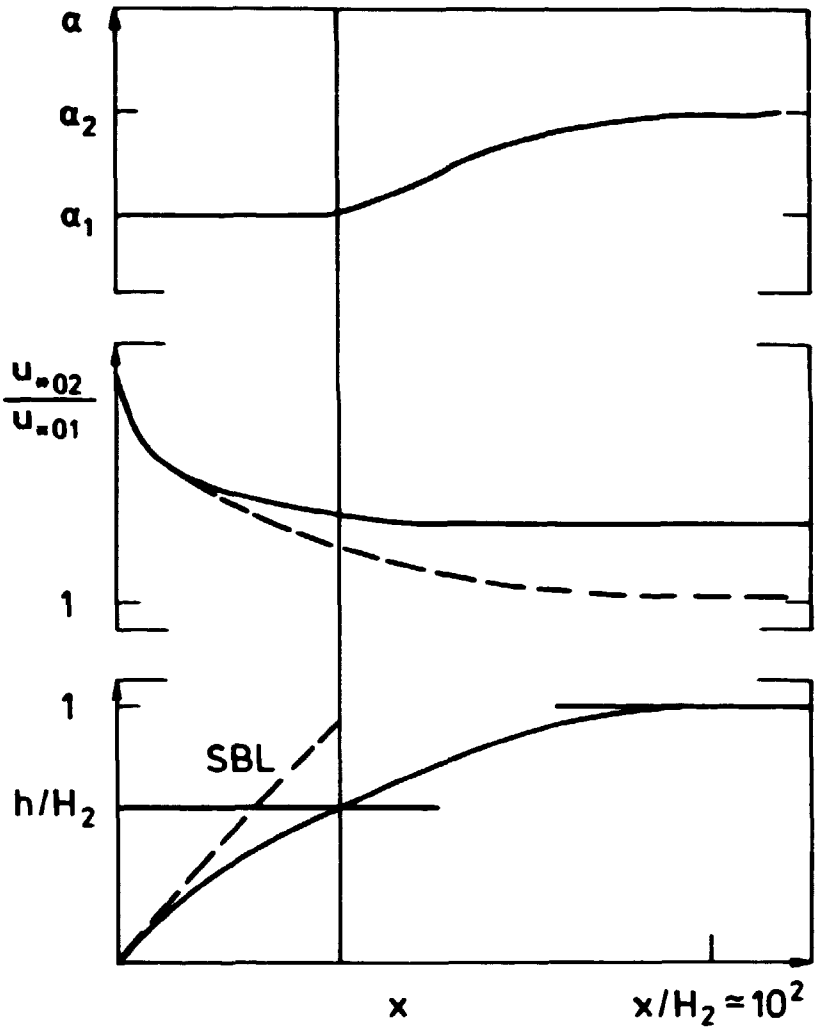

Fig. 5.13. Principal behaviour of the model in Section 5.6, with respect to the variation in the height of the internal boundary layer, h, the surface stresses, and the cross isobaric angle. Also shown for comparison is the behaviour of the surface layer model (---). The figure further illustrates that the approach to the new equilibrium situation typically is reached for $x/H_2 \approx 10^2$, $H_2 = u_{*02}/f$ being the scaling height of the new planetary boundary layer.

as the best value. The curves represent results from a second-order closure model used by Rao et al. (1974) to model the results of Bradley. For the rough-to-smooth transition they have used two different smooth z_o-values, because their model results do not describe the data when they use Bradley's z_o-values (Rao et al. 1974)).

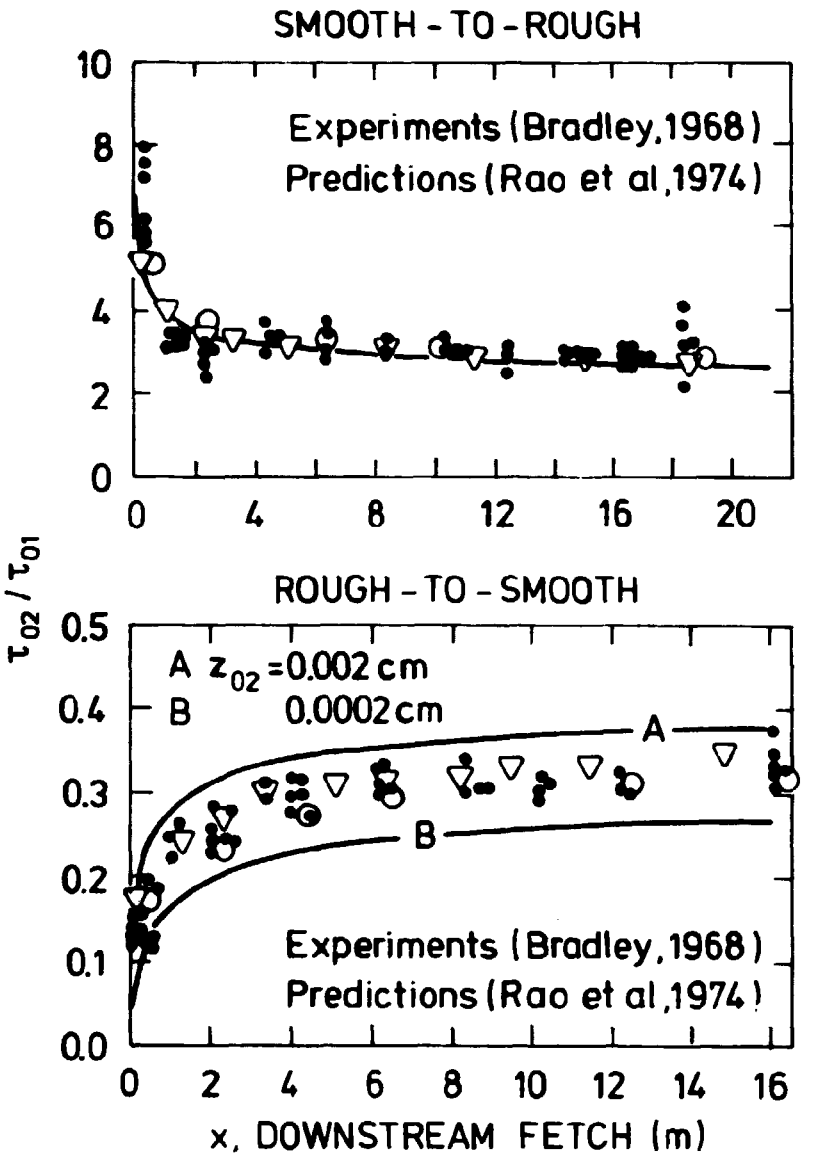

Fig. 5.14. Ratio of surface stresses for the smooth-to-rough transition and the rough-to-smooth transition. The points are data from Bradley (1968), while the curves are the model predictions taken from Rao et al. (1974). The circles correspond to the predictions of (5.17) and (5.18) with C = 0.5. The triangles pertain to the same equations but with C = 1.0. Bradley (1968) specify the rough z_o as 0.25 cm and the smooth z_o as 0.002 cm.

Finally we shall comment on the problems associated with the rough-to-smooth transition. As discussed above, we have chosen the z_o and the H values in (5.17) to pertain to the rougher

values, in accordance with the intenser turbulence of the rougher surface causing it to be dominant in the entrainment processes. Since the lifetime of the boundary layer scale eddies will be of the order $H/u_{*_0} \approx 1/f$, the rough eddies should continue to be dominant for fetches of the order of $\Box/f$, which for typical velocities will be of the order of 100 km. Therefore, it is sensible also for the rough-to-smooth transition to use $H = H_{rough}$ in (5.17). However, another constraint is that $h(x \to \infty) = H_{smooth} < H_{rough}$. As Equation (5.17) is too simple to provide information about h's final approach to H_{smooth}, the most reasonable approach for the rough-to-smooth transiton is to let $H = H_{rough}$ and to stop the development in h as soon as it reaches H_{smooth}. A more complete model should probably include both scaling heights with a lifetime in the growth formula for h(x), but so far we feel it important to keep the model as simple as possible.

6. ANALYSIS OF WIND DATA FROM DIRECTION INTERVALS

6.1. Introduction

In the previous chapter we treated the effects of inhomogeneity with respect to both wind speed and direction. These effects are sufficiently large to be detected even with a primitive instrumental set-up. But it is mandatory to analyse the data carefully so that the effects of inhomogeneity are revealed.

By using time-averaged data we partially eliminate the effects of instationarity, and we are therefore able to use the theories that are based upon stationarity of the wind field. The theories we used in the previous chapter were also based on the assumption of barotropy. In most cases this is largely fulfilled as advection of either cold or warm air generally is a transient phenomenon, that is, baroclinicity will be present only in a

limited part of the data. Furthermore, averaging will smooth the effect of baroclinicity.

To reveal the effects of inhomogeneity we truncated the direction into intervals of 6^{o}. This sector width was found sufficient to secure identical upstream conditions for each sample. The sector was determined by the wind direction at Gylling Næs, θ_G. Wind data from Gylling Næs in a specific direction interval, together with simultaneously occurring data from Alrø thus make up two samples suitable for direct comparison in that they derive from the same synoptic situations. Due to the short distance (10 km) between the two stations, this selection procedure assures equality of the geostrophic winds at the two sites. This is a very important point when we discuss any differences in wind speed and direction that may be exist between the sites. As some effects of terrain inhomogeneities are expected to be wind speed dependent, the data were furthermore subdivided into four wind speed categories based on the speed at 17.5 m at Gylling Næs. The intervals were defined as follows:

Wind speed group	0		$U < 3$ m/s
- - -	1	3 m/s $\leq U <$	6 m/s
- - -	2	6 m/s $\leq U <$	9 m/s
- - -	3	9 m/s $\leq U$	

With 60 direction intervals we thus have 240 groups of wind speed and direction at each site for direct comparison. For each of these samples mean wind speed and mean direction were computed.

Due to the selection procedure, the wind direction at Alrø exhibits a certain distribution around its mean value. For the four different wind speed groups this distribution is shown in Fig. 6.1 for sector 46 (276^{o}). The curve is a normal distribution with mean and variance as the sample. The deviation from normal is most clearly exhibited by wind speed group 0. This could be anticipated partly because the direction for small wind speeds is ill defined due to the damping of the wind vane, and partly because the wind direction at very low wind speeds

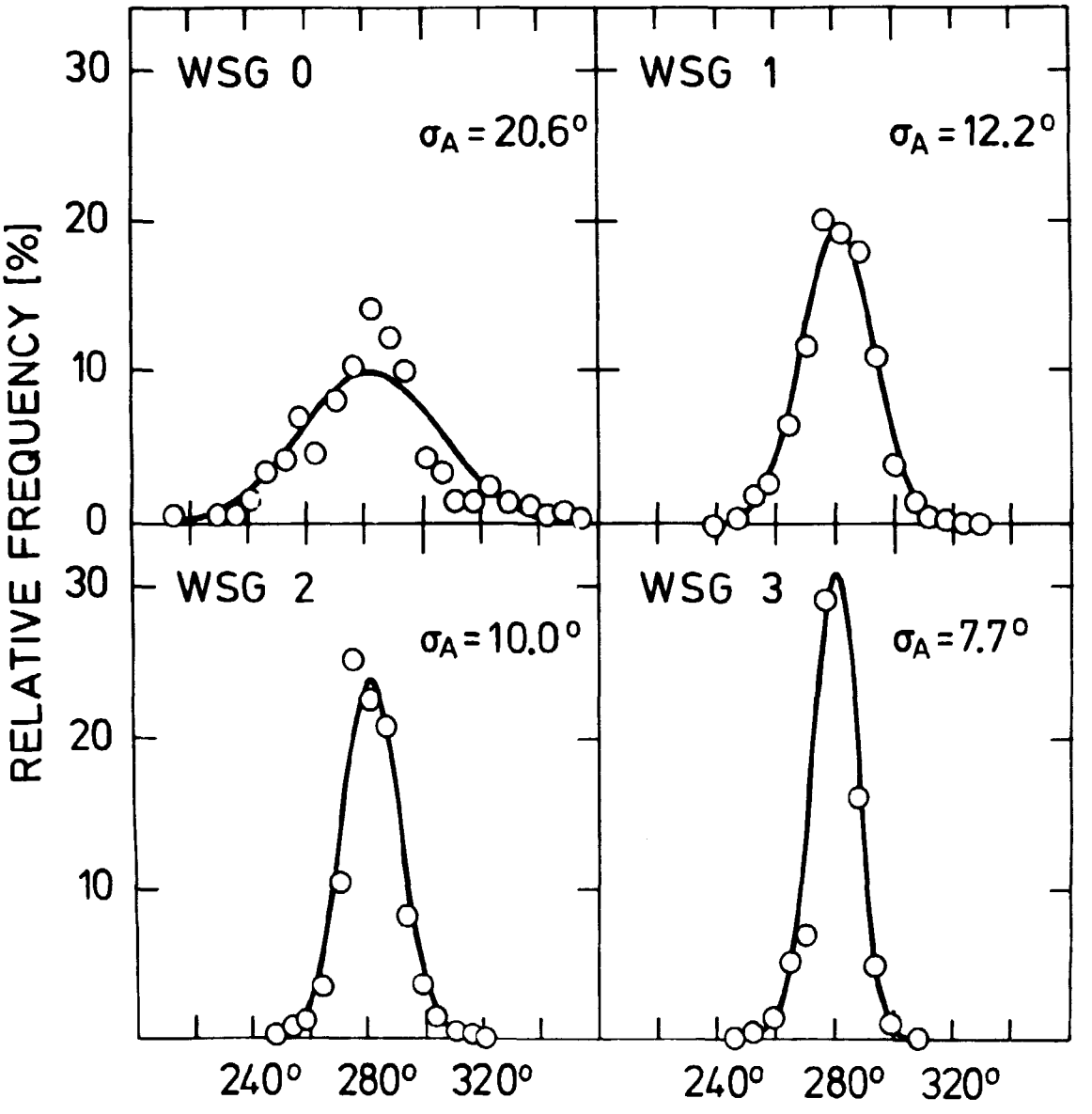

Fig. 6.1. Distribution of direction at Alrø for Gylling Næs direction in the interval 273°-279°, i.e. sector 46 for the different wind speed groups (WSG). σ_A is the standard deviation. The curves are the normal distributions with the same mean and standard deviation as the sample.

will be strongly influenced by local inhomogeneities in the neighbourhood of each tower. For this wind speed group it is therefore difficult to apply the kind of analysis tried here, and we shall not consider this group further.

For wind speeds greater than 3 m/s the distribution is close to normal, and the mean direction at Alrø is therefore a well-defined quantity. The standard deviation is, however, considerable. The main reason for this large deviation is the influence on the instantaneous direction measurement by turbulence. Sector 46 is the one with the greatest frequency of occurrence, and we shall use the standard deviation in direction distribution at Alrø for this sector to be applicable for all the sectors. The uncertainty in determining the mean direction at Alrø is thus $\sigma_A/N^{1/2}$, where N is the number of elements in the sample. Values of this number are 1.2^o, 0.8^o, 0.4^o, 0.4^o for wind speed groups 0 to 3, meaning that the mean values of the distributions in Fig. 6.1 are determined with this uncertainty. The choice of Gylling Næs as reference for subdividing into categories is of course arbitrary. The main point in this analysis is to select samples for time averaging which are derived from synoptic situations identical at the two sites. In the following paragraphs we will show how time-averaged data derived in this manner displays detailed information which otherwise could be regarded as noise.

6.2. Variation of profile curvature with direction

The existence of an internal boundary layer (IBL) usually shows up as a kink in the wind profile, lying at height δ of the IBL (cf. Chapter 5). Due to the proximity of water surfaces for both sites we therefore expect kinks to be present in the wind profiles for some directions.

As already mentioned in Chapter 4, a three-point climatologically averaged profile will exhibit a slight kink due to the curvature caused by stability. By applying Eq. (4.9) to the averaged profile for each sector and using the c(z) function determined from the averaged stability, it is possible to determine a z_o value for the lower and upper part of the profile in which the stability effect has been eliminated. We will use indices "ℓ" and "u" to distinguish the values. For the horizontal and homogeneous surface the two z_o values should be equal,

i.e. $z_{o,\ell} = z_{o,u}$. If the profile's center of curvature were downward, i.e. a kink to the left, the $z_{o,u}$ would be greater than $z_{o,\ell}$; if it were upwards and with now $z_{o,\ell}$ less than $z_{o,u}$ and a kink to the right.

An analysis for curvature in this manner is much more convenient than considering the profiles. This is so because one can easily determine which part of the profile, if any, has a physically realistic z_o value. In Figs. 6.2 a-b the $z_{o,\ell}$ and $z_{o,u}$ values are shown in a polar logarithmic plot. The most striking feature of the figures are the extreme variations in $z_{o,u}$ at both sites compared with the near constancy of $z_{o,\ell}$ (in the logarithmic sense).

In the following we shall discuss the detailed behaviour of $z_{o,u}$ and $z_{o,\ell}$ as functions of direction.

Since $z_{o,u}$ is especially heavily influenced by terrain inhomogeneities close to the masts, we shall draw upon the theories of internal boundary layers, as summarized in Section 5.1.

The positions of the masts, as well as the instrumentation configurations are shown in the figures in Section 2. However, more detailed knowledge is needed about the instrumentation and the terrain features than can be deduced from these figures. Therefore, we present below relevant parts of the site and instrumentation description extracted from the log-books of the measuring programme.

Description of the Gylling Næs site

Instrumentation:
The 17.5-m boom is along the E-W direction with the cup-anemometer in the west end and the wind vane in the east end. The lower level booms point towards 210°. The Stevenson screen is placed approximately 2 meters from the mast towards north.

Terrain:

a) The terrain generally slopes upward from the south towards north. The slope from the bottom of the bight at the south towards the mast is about 1:200. From the mast and northward the slope is somewhat less.

b) The coastline runs roughly as a circle from the east to the bottom of the bight at the south. The distance from the mast to the coast is roughly 500 m at the east decreasing to 200 meters at 150°. Furthermore, the coast includes a coastal brink roughly 3 m high at 90° and decreasing to about 1 meter at 150°.

c) At the bottom of the bight towards the south a dike is situated roughly 3 m high. The dike is covered with bushes and low trees, and subtends the angle 170°-220° as seen from the mast.

d) Behind the dike an old fjord runs towards the northwest. The terrain here appears as marsh with sparse vegetation of low trees and bushes. The distance from the foot of the dike and the old fjord, where the slope begins is roughly 200 m. This terrain feature is seen in the 220°-270° sector.

e) From 270° a living fence of bushes and low trees runs roughly SSE-NNW. At 270° the distance is roughly 100 m, retreating to about 0.5 km at 340°. Here the fence turns east until it meets the coastline at 30°. It follows the coast down to 70°-80°. In the 0-30° sectors the fence appears as very open leaving a long rather undisturbed fetch of fields similar to the one where the mast is placed. In the corner, where the fence turns east, a farm is situated in a grove, meaning that here the fence appears as both denser and nearer to the mast (~ 350 m). This configuration covers the 340°-350°.

f) The field in the neighbourhood of the mast has an estimated roughness length of approximately 1 cm.

Description of the Alrø site

Instrumentation:

The instrumentation is arranged as at the Gylling Næs site;

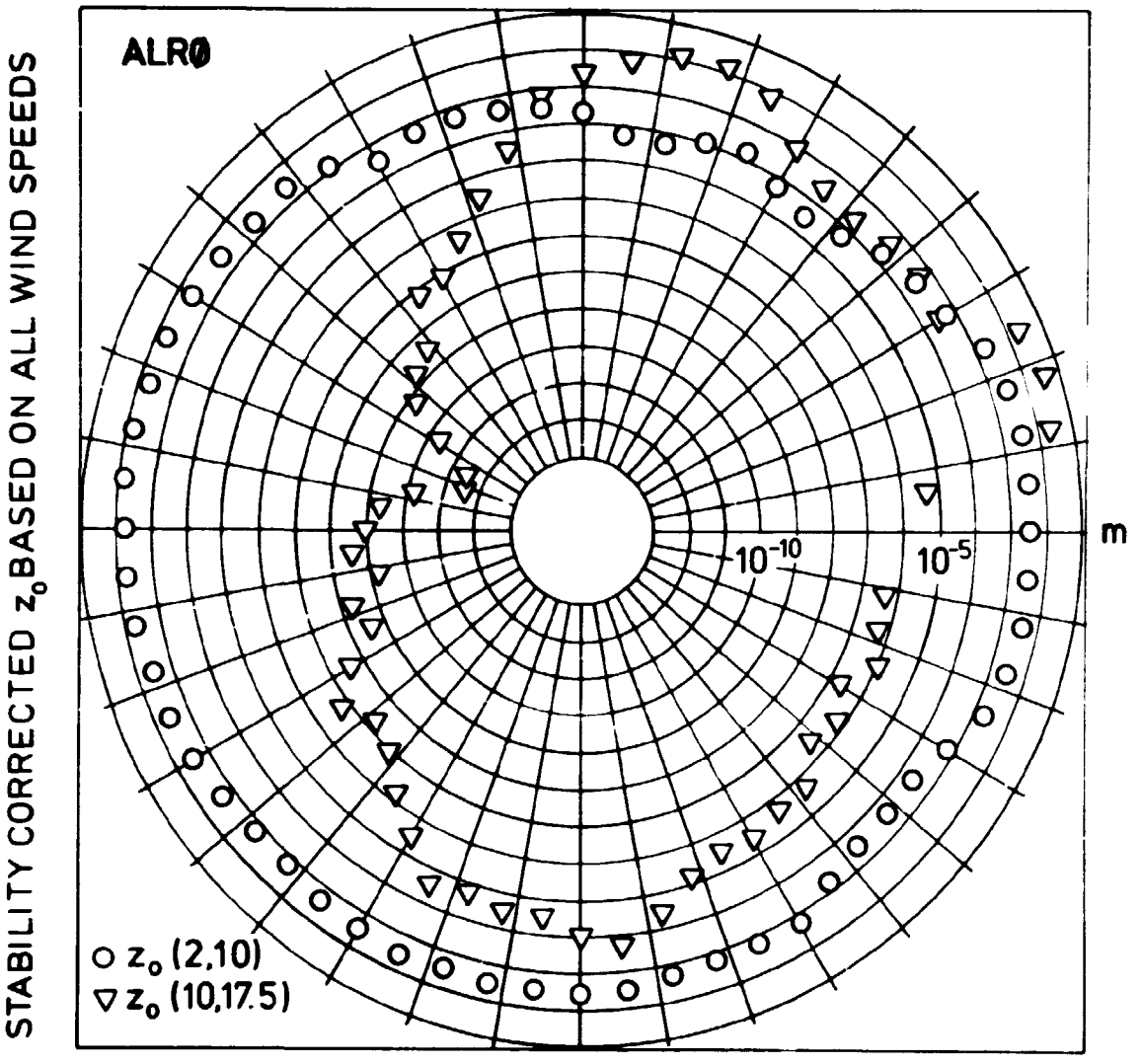

Fig. 6.2.a-b. Stability-corrected z_o based on all wind speeds as a function of direction for the two stations. The z_o values derived from the lower part of the profile (anemometers at heights 2 and 10 m) are z_o (2,10) = $z_{o,l}$ and from the upper part of the profile (anemometers at heights 10 and 17.5 m) are z_o(10,17.5) = $z_{o,u}$. a) Alrø. b) Gylling Næs.

except that the Stevenson screen is placed directly on the mast towards south at a height of two meters.

Terrain:

a) The mast is placed in a field with the same estimated roughness as for the Gylling Næs site. Furthermore, it lies in

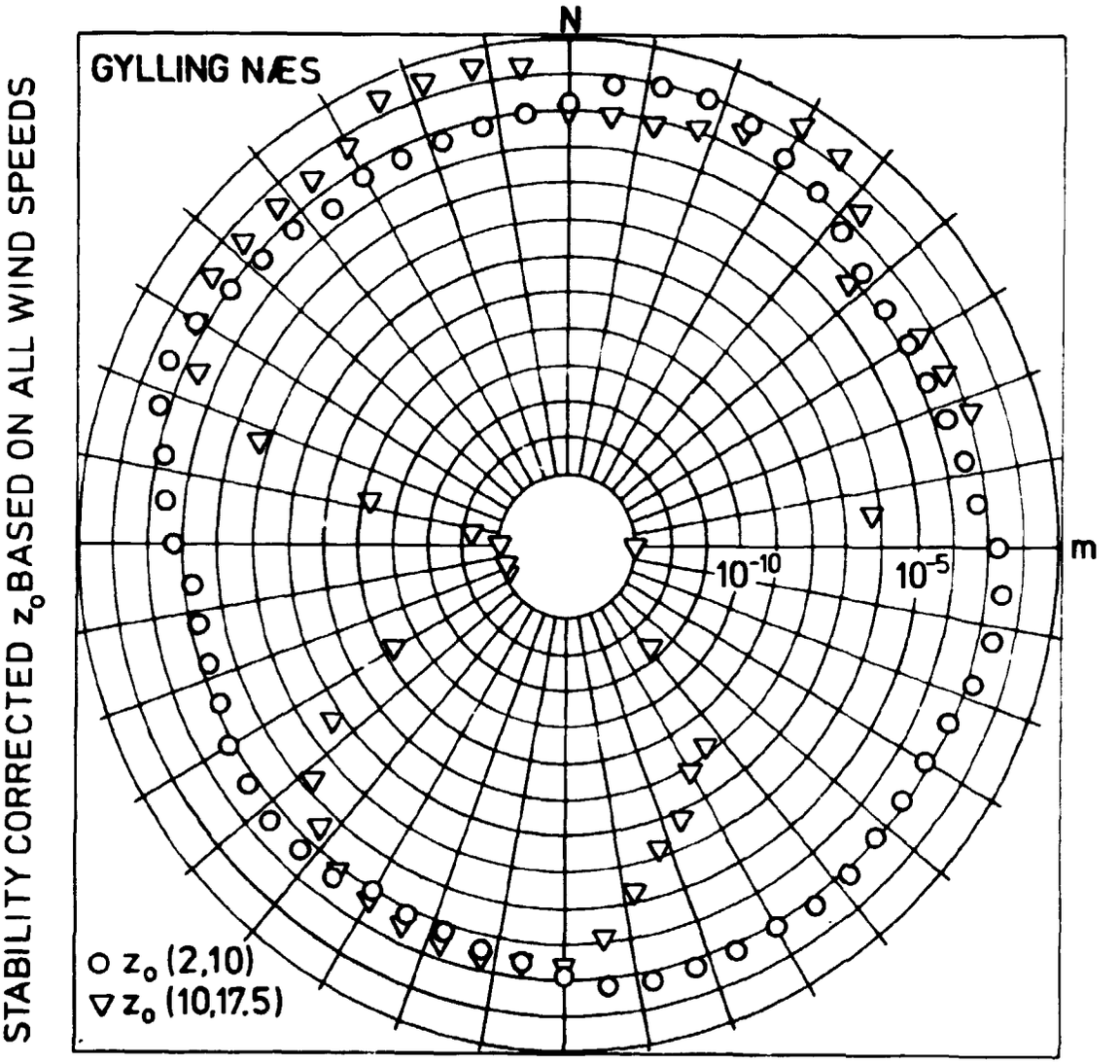

the SW corner of the island (see map in Section 2). This means that in sector 0^{o}-90^{o} the mast sees a very long and uniform fetch with a few farm buildings placed at distances of 300 m or longer as the only obstructions. The most spectacular of these is a farm in a grove 300 meters distant in the 10^{o}-20^{o} sector and a more distant (~ 1 km) small wood with fairly tall trees at 70^{o}-80^{o}.

b) From 90^{o}-180^{o} the distance to the coastline decreases until it reaches about 180 m at 140^{o}.

c) This distance is constant until roughly 290^{o} from where it increases again to several km at the north.

d) The coastline has a brink. At 90^{o} it is about 3 m in height decreasing to 2 m at 180^{o}, a height which slowly increases

to 4-5 m at the north. In front of the brink can be found a flat beach, 10-20 m in width.

e) In the 150°-270° sector the terrain slopes uniformly up to the mast with a slope of around 1:100. In the 270°-90° sector there is no slope worth mentioning, while the 90°-180° sector is characterized by a gradual increase of the slope from 0 to 1:100.

Below we shall discuss in greater detail the behaviour of the z_o's vs. direction in Figs. 6.2a and b.

Concerning the influence of the instrumentation set-up two things are worth noting:

a) For both stations $z_{o,u}$ shows a very deep and sharp minimum at 90°. This minimum is consistent with the assumption that the wind vane at the upper boom (17.5 m) shadows the cup-anemometer and thereby reduces the velocity measured at this level.

b) The second point is negative in the sense that, strangely enough, the Stevenson screen, which is fairly close to the low-level instrumentation, does not show up in $z_{o,\ell}$, where some effects would be expected for the sectors around 0° for Gylling Næs and around 70° for Alrø.

Next we turn towards the influence of terrain inhomogeneities on the wind profiles at the two masts. First, a few general remarks will be useful. We notice from the description of the sites that for both sites the typical smallest fetch that must be used to describe the height of the internal boundary layer, δ or/and δ_p (see Section 5.1), are of the order of 200 m. With the roughness length, $z_o \approx 1$ cm, the height of the internal boundary layer is around 11 m at the positions of the masts. This means that $z_{o,\ell}$ will approximately describe the roughness of the immediate surroundings to the mast. It also explains why $z_{o,u}$ in some sectors will be very small indeed, as can be seen from Fig. 5.1, where the 10- and 17.5-m levels will be situated on each side of the kink in the profile.

Although $z_{o,\ell}$ varies much less with direction than does $z_{o,u}$, it does show some variation, and it is generally somewhat smaller than the roughness length one usually asigns to this kind of surface. This can be understood in the light of the approximateness of the theories summarized in Section 5.1. The 10-m level is actually close to the smallest estimate of δ_p (and δ) and so it is conceivable that the fractional speed up, s in Section 5.1, will be less at 10 m than at the lowest instrument level 2 m, resulting in a decrease of the measured roughness length $z_{o,\ell}$, relative to the "true" aerodynamic roughness of the surface.

The $z_{o,u}$ values vary so much from sector to sector and from site to site that we shall discuss them in greater detail, presenting them separately below.

Discussion of $z_{o,u}$ at Gylling Næs

From 290^o-80^o $z_{o,u} \gtrsim z_{o,\ell}$. This is consistent with the site description in the sense that the fetch in this direction is long and bordered with trees producing a slight additional roughness length. Notice that $z_{o,u} \approx z_{o,\ell}$ for 0^o-30^o consistent with the note in the site description that the distant living fence is rather open here. Furthermore, it is seen that the farm seems to show up at 340^o-350^o in the $z_{o,u}$-curve as an increased roughness length.

In the sector 80^o-150^o three different internal boundary layers influence the mast data :1) roughness change between sea and land, 2) escarpment layer due to the coastal brink, and 3) from 90^o-150^o degrees the slope of the terrain, which increases until it reaches a value of about 1:200 at 180^o. From the discussion above we have $\delta \approx \delta_p \approx 11$ m and from Fig. 5.1 it is seen that the velocities at 10 and 17.5 m supposedly are closer to each other than would be expected from the $z_{o,\ell}$-value, a result which is reflected in the low $z_{o,u}$-values in this sector.

The 180^{o}-230^{o} sector, where $z_{o,\ell} = z_{o,u}$, so closely coincides with the 150^{o}-230^{o} sector in which the dike is seen at a distance of 200 m, that it must be concluded that the greater height and roughness of the dike nullify the influence of the slope up to the mast in this sector.

The sector between 230^{o} and 290^{o} is characterized by a sharp variation of $z_{o,u}$ with a very low minimum around 260^{o}. Physically the sector is described by an unobstructed fetch down the slope to the old fjord. With a slope length of 200 m and a roughness length $z_o \sim 1$ cm we obtain $\delta_p \sim 11$ m. Taking the height of the hill as 3 m we obtain a fractional speed up of $s \sim 2 \cdot 3/200 = 3\%$.

We now assume that the whole profile would be in equilibrium with $z_{o,\ell}$, if the pressure perturbations due to the slope were absent. Thus, we can write for neutral conditions for this hypothetical, unperturbed profile:

$$\frac{u_1}{u_2} = 1 - \frac{\ln(\frac{z_2}{z_1})}{\ln\frac{z_2}{z_{o,\ell}}} = 0.935 \quad ,$$

where $u_1 = u(z = z_1 = 10 \text{ m})$ and $u_2 = u_2(z = z_2 = 17.5 \text{ m})$.

Next we assume that the pressure perturbations influences u_2 negligibly since z_2 is above δ_p. Letting u_1 increase by 1+s, we obtain

$$(1+s)\frac{u_1}{u_2} = (1+s) \cdot \left(1 - \frac{\ln(\frac{z_2}{z_1})}{\ln(\frac{z_2}{z_{o,\ell}})}\right) = (1+s)\ 0.935$$

$$\equiv \left(1 - \frac{\ln(\frac{z_2}{z_1})}{\ln(\frac{z_2}{z_{o,u}})}\right) \quad .$$

Rearranging yields

$$z_{o,u} = 17.5 \exp\left(-\frac{0.56}{1-(1+s)0.935}\right) \quad ,$$

an equation which shows how highly variable $z_{o,u}$ may be expected to be. The resulting $z_{o,u}$ values are shown below for different s-values

s(%)	$z_{o,u}$(m)
3	$4.6 \cdot 10^{-6}$
4	$2.7 \cdot 10^{-8}$
5	$8.3 \cdot 10^{-13}$
6	$4.7 \cdot 10^{-28}$

The calculations above are based on grossly simplifying assumptions. A few of the complications are: (1) $z_{o,\ell}$ is probably too small, as argued above, meaning that 0.935 is also too small, (2) u_2 might actually be in equilibrium with the even greater roughness of the old fjord (fields with bushes and trees correspond to $z_o \sim 5$ cm), (3) the theories used here and described in Section 2 are approximate, even for ideal surfaces, (4) the flow cannot be considered two dimensional since the surface conditions from neighbouring sectors will diffuse into each other as the distances to the surface elements increase (see description of the site above), and finally, (5) u(z = 17.5 m)

is somewhat influenced by the pressure perturbation although less than u(z = 10 m) (see Fig. 5.1).

Discussion of $z_{o,u}$ for Alrø

With the similar discussion for Gylling Næs in mind the corresponding one for Alrø is simple.

In the 0°-90° sector, $z_{o,u} \approx z_{o,\ell}$ in accordance with a large and fairly uniform fetch. In the other sectors we again have three different internal boundary layers (IBL): a) an IBL due to roughness change between water and land, b) an IBL due to the coastal brink, and c) an IBL due to the sloping terrain. If we go from 90° to 180°, the land fetch and height of the escarpment decrease while the slope increases, the result is a roughly constant value of $z_{o,u}$. In the 180°-270° sector fetch and slope are constant while the escarpment height increases from around 220°, giving rise to a minimum $z_{o,u}$ around 270°. From 270° to 0° the increasing fetch and decreasing slope result in an increasing $z_{o,u}$. As for Gylling Næs, we notice that the two most spectacular roughness elements in the 0-90° sector (a farm and a wood) show up in the $z_{o,u}$-curve.

Based on the discussion above we draw the following qualitative conclusions:

a) The proper roughness for the two sites is between 10^{-2} and 10^{-3} m, as is largely reflected in $z_{o,\ell}$.
b) The behaviour of $z_{o,u}$ is strongly influenced by internal boundary layers, which intersect the masts between the 10- and 17.5-m levels and perturbs the lower level data while largely leaving the 17.5-m level data unaltered.
c) A consequence of b) is that the 17.5-m level data essentially reflects the upstream surface conditions, or more specifically at the two sites. Gylling Næs: At sector 90°-150°: the water surface at 150°-230°: the dike, and at 230°-270°: the old fjord area. Alrø at sector 90°-300°: the water surface.

d) The conclusions under c) pertain to the averaged data alone. Of course, the averaging procedure might mask differences for different stability classes, since especially extreme stable and unstable categories occur relatively infrequently and hence contribute little to the average.

6.3. Changes in wind speed due to changing terrain.

Figure 6.3 shows how the mean velocity varies at Alrø and Gylling Næs for the different velocity groups. This variation is further accentuated in Fig. 6.4, which gives the ratios between the mean velocities for the velocities in speed groups 2 and 3.

It is noticeable how similar are the velocity ratios in Fig. 6.4 for the different heights, in spite of the multitude of different internal boundary layers which influence the data at the two sites.

To explain this behaviour we must appeal to the theories in Section 5. Below we shall see that these theories taken together with nearby terrain features can explain the behaviour of the velocities in Fig. 6.3 and the velocity ratios in Fig. 6.4.

Turning to Fig. 6.4 and starting from the north we see that $U_G < U_A$ in sector 10^o-90^o. From the description of the sites it follows that in this sector Alrø has a farm in a grove at a distance of 300 m in sectors 2 and 3 (10^o-20^o), while the living fence at the Gylling site was described as very open here. Concerning the large-scale fetches, the Gylling Næs trajectories are mostly over water, while for Alrø they are mostly over land. This description is seen to be in accordance with U_G being generally larger than U_A, and that the ratio has a a local minimum at 10^o-20^o.

Around 90^o the velocities at the two sites are roughly equal corresponding to the similarity of both the shorter and the longer fetches: no slope, about the same land fetch, and the upstream trajectories lie over water.

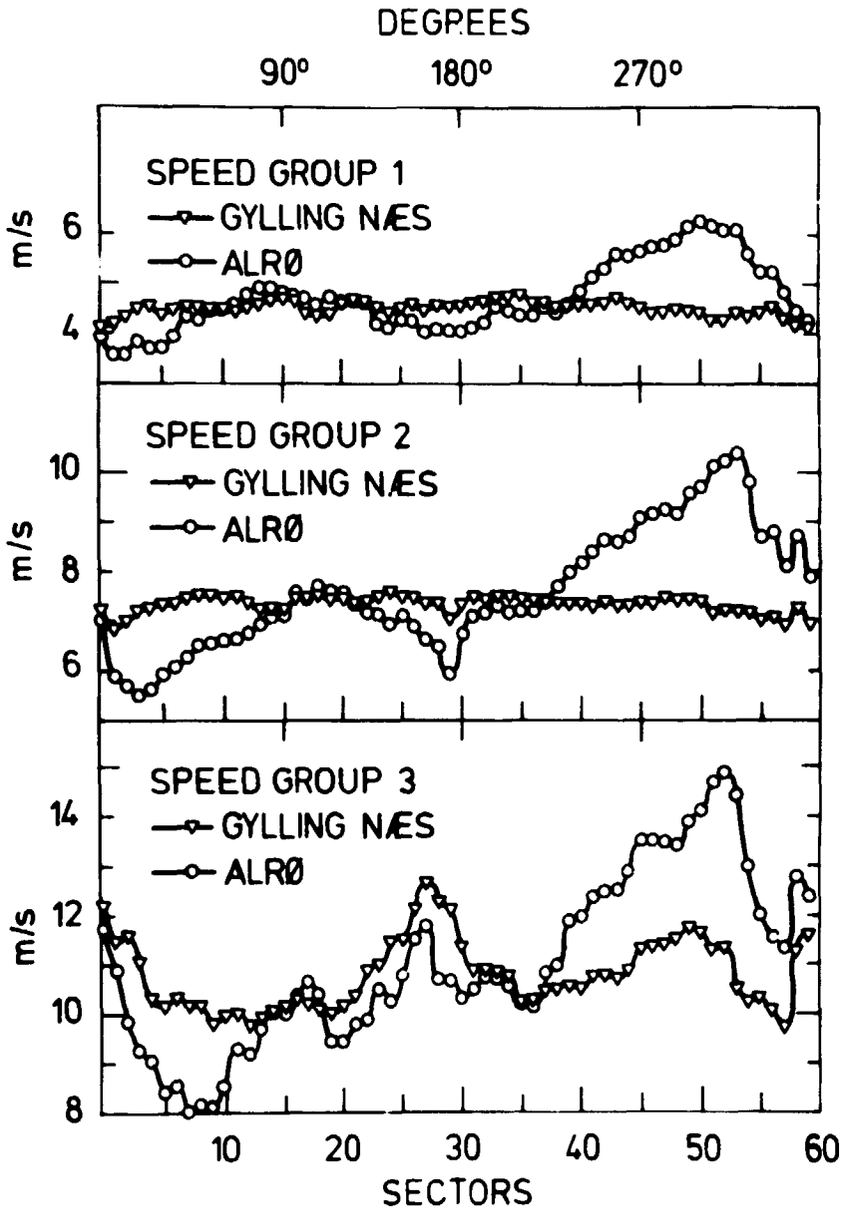

Fig. 6.3. Average wind speed at 17.5 m at the two stations as a function of the direction at Gylling Næs. The speed groups are defined in Section 6.1. For each direction and each speed group the averages are derived from simultaneous data in order to facilitate direct comparison.

Moving south from 90° to 180° we see that the short-range fetch characteristics at Alrø and Gylling Næs are very similar with respect to their increasing slope, decreasing height of the coastal brink, and fairly equal distance to the water. From sector 90°-110° (sectors 15-18), the upstream conditions are similar as well, with the trajectories coming in from the Kattegat.

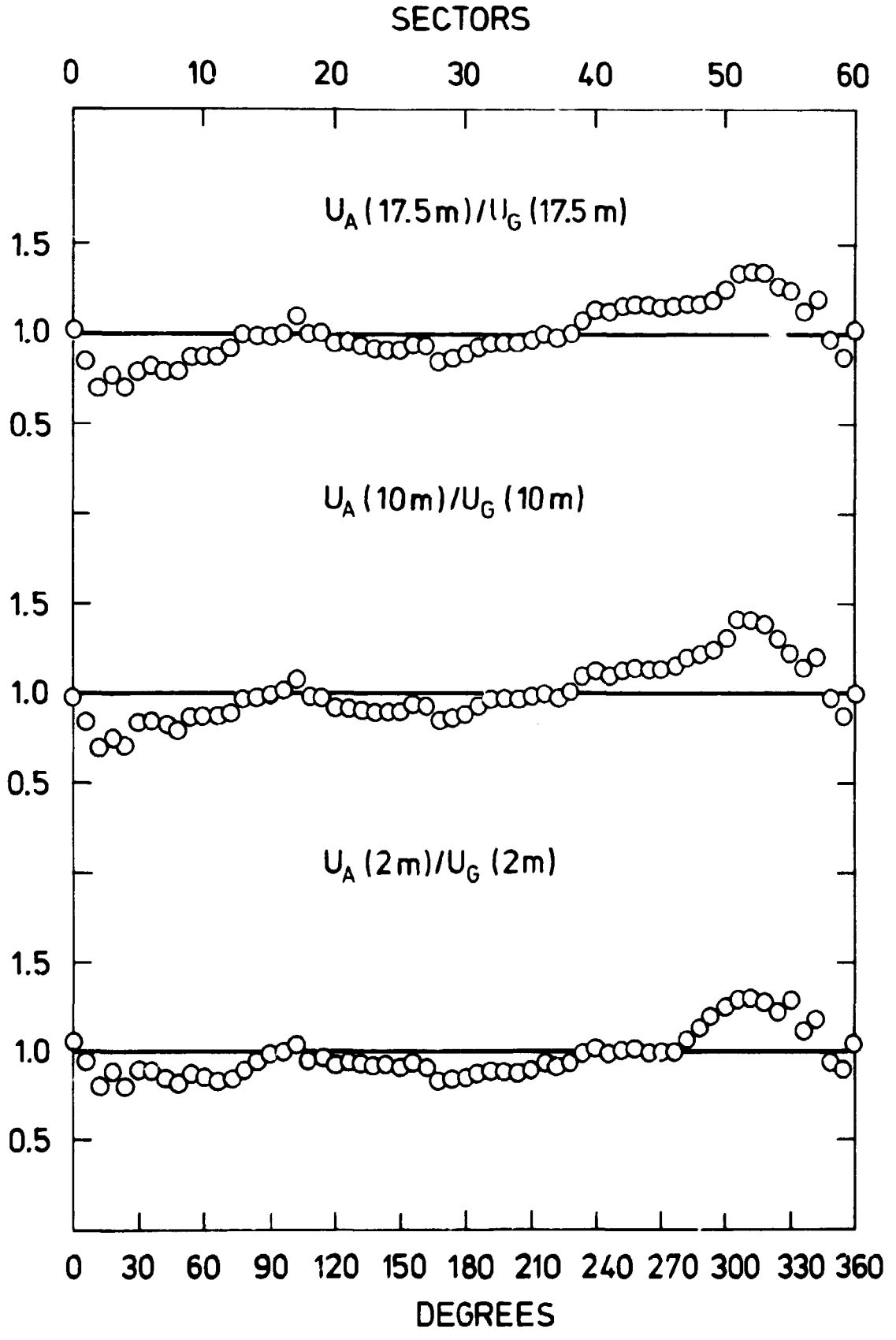

Fig. 6.4. Ratios between average wind speeds at the two stations for the three different measuring heights, based on the simultaneous data from wind speed groups 2 and 3.

From sector 20 (120°), however, the trajectory through the Alrø site starts to pass over land, while the upstream Gylling Næs trajectory remains over water. The change for the Alrø trajectory conditions are seen as a decrease in U_A/U_G in Fig. 6.4 around sector 20. An interesting point here is that U_A/U_G shows a weak but distinct local maximum at sectors 25-26 (150-156°) where the upstream trajectory to the Alrø site passes through the Hjarnø sound becoming a pure water trajectory again (see Fig. 6.14). Thereafter, until sector 29 (174°) is reached, the upstream conditions for Alrø become increasingly influenced by a land fetch, for which reason U_A/U_G starts decreasing further.

From sectors 29 to 46 the main fetch characteristics for the two measuring stations are:

At Gylling Næs, the immediate surroundings to a distance of roughly 200 m are characterized by the gently sloping field, described in Section 6.2. At slightly larger distances the land fetch suddenly increases to roughly 2 km, and the additional land fetch remains fairly uniform both in length and surface characteristics until sector 46 (see description in Section 6.2 and the map in Fig. 6.13). At even larger distances, the upstream surface boundary remains water until sector 39, where the upstream conditions include parts of the Horsens fjord and parts of the land beyond that.

At Alrø, the immediate surroundings are constituted by the 180-m long gentle slope with an escarpment. Further upstream we meet the fjord of a constant width to around sector 37, from where the water fetch increases with the sectors until sector 46. At even longer distances we now have the fairly uniform trajectories over Jutland, meaning that for these distances the upstream conditions for Alrø and Gylling Næs are the same.

Turning again to Fig. 6.4 we see how these conditions influence the velocity ratio. From Sector 30 to 39 the ratio increases toward one. In this latter sector the land-water-land fetches for the two stations must consequently result in the same velocity. From sector 39-46 the ratio increases first strongly then

only a little, reflecting largely the increased waterfetch for Alrø. The ratio at the 17.5-m level increases to about 1.15, at the 10-m level to 1.13, while at the 2-m level it is fairly uniformly 1.02.

This behaviour can be understood in the light of the description of the sites in Section 6.2 and the theories summarized in 5.1.

The 2-meter levels are completely within the internal boundary layers of the nearest 200-meter fetch, and since the surface conditions here are very similar at the two sites, the velocity ratio is around 1.

At the 17.5-m level the Alrø data are within the water boundary layer, and therefore reflect the increased water fetch. The 10-m level is just on the borderline between the two boundary layers, and the velocity at Alrø should therefore feel both layers. However, due to the pressure effects from both the slope and the escarpment the resulting velocity will be close to the velocity at 17.5-m, as seen from Fig. 5.1 and also from Fig. 6.2.b.

As the sector number increases to around 50 and higher, land surface wind trajectories for both stations become increasingly dominant. This is especially true for Gylling Næs where the trajectories become pure land from sector 48. At the same time the Gylling Næs data are undoubtedly influenced by a lee effect from the living fence which is fairly close to the mast in these sectors (see site description in Section 6.2). Therefore, it is not surprising to see that the velocity ratio increases in this sector interval.

In the remaining sectors, 50-60, the lee effect at Gylling Næs decreases due to increasing distance to the trees, probably interrupted by the farmhouse in sector 57, and consequently the velocity ratio seeks back to unity.

The flow conditions in this sector interval are expected to be fairly complicated as reflected by the fine structure of the velocity ratios in Fig. 6.4. The most complicating factor is

probably the flow structure at Alrø, where the flow comes from the fairly high-level coast (60-80 m) north of Horsens fjord, continues over water, and runs fairly parallel with the coast of Alrø. Note, however, the local maximum at sector 57, probably reflecting the farmhouse at Gylling Næs.

In this section, the discussion has been based on Fig. 6.4 rather than on 6.3, since the mean velocities themselves, as seen in 6.3, reflect not only differences in surface conditions, but also that different synoptic situations have been dominant in different sectors. However, in addition, the velocity ratios do differ for the various velocity groups, as will be shown in the next section, where we shall separately treat the ratios in sectors 40-50 for the different velocity groups.

6.4. Wind speed ratios as function of fetches over water

As noted in Section 6.3, in sectors 37-47 the behaviour of the velocity ratios in Fig. 6.4 can largely be ascribed to the in-increasing water fetch for the Alrø station. However, as seen from Figs. 2.1 and 2.2, winds blowing across the Horsens fjord area will encounter quite a number of surfaces changes, the distribution of which will vary with wind direction. Figure 6.5 illustrates this for winds from the west.

Below we shall show that all the complex terrain features shown in Fig. 6.5 have to be taken into account if some of the details in the velocity ratio data are to be explained. We will show this by using different models of increasing complexity. We will start by trying simply to interpret the data in terms of the water fetch for the Alrø station, employing a characteristic roughness for the water surface. As next step we shall see the consequences of letting the water roughness be fetch dependent, and finally we shall try to model the multiple roughness changes depicted in Fig. 6.5.

First, we shall see how much of the behaviour of the velocity ratio we can explain only in terms of the increase in water

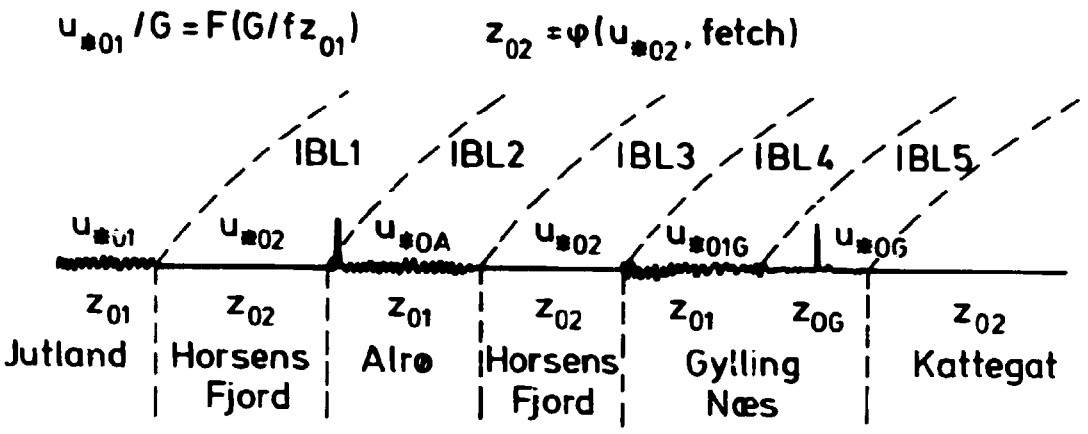

Fig. 6.5. Schematic drawing of the different internal boundary layers influencing the Alrø-Gylling Næs data. Also the relations relating u_{*1} to the geostrophic wind and the water roughness z_{02} to surface stress and fetch are indicated. The distribution of IBL's varies with wind direction; the scetch pertains to winds from the west.

fetch for the Alrø station. To study this point further, in Fig. 6.6 we plotted U_A/U_G for velocity group 3 data both measured at $z = 17.5$ m, as a function of an estimated effective water fetch for the Alrø station (the circles in Fig. 6.6). The curves, on the other hand, represent our theoretical estimates to which we shall return. We concentrate on velocity group 3 data because our model in Section 5.6 pertains to neutral conditions only, and the high velocity data of velocity group 3 are most likely to be dominated by mechanically generated turbulence.

We start by describing the meaning of the concept "effective water fetch". We wish to interpret Fig. 6.6 as the ratio of the over-water to over-land (upstream) velocity within the framework of the theory described in Section 5.6. However, the Gylling Næs data neither represents fully over-land trajectories, in that the trajectories pass over a mixture of land and water surfaces for intermediate fetches, nor is it upstream of Alrø, Furthermore, although the Alrø data at 17.5 m cannot be considered within the internal boundary layer of Alrø, it can neither be considered completely as representing the undisturbed

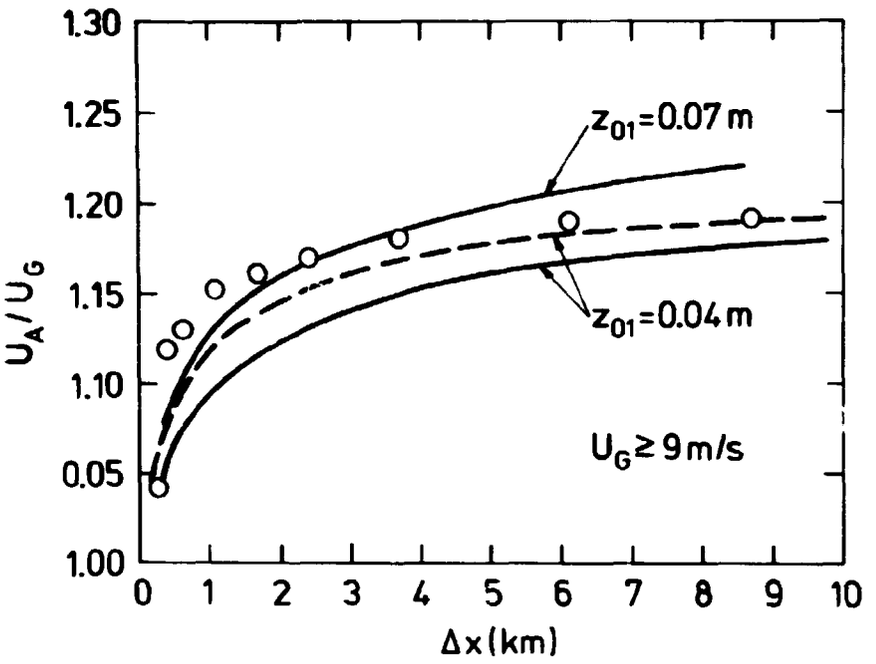

Fig. 6.6. The ratio $U_A(17.5\ m)/U_G(17.5\ m)$ for velocity group 3 in sectors 37-47 plotted as a function of the estimated effective water fetch for the Alrø station. The circles are measurements. The solid curves show the model predictions with a constant z_{02} given by (6.3) and the z_{01}-values indicated, while the broken curve correspond to a fetch dependent z_{02} as given by Table 6.2.

overwater boundary layer of Horsens fjord (see the discussion in Sections 6.1-6.3).

These nonidealities of the data set are reflected in the fact that the ratio U_A/U_G is one in sectors where the water fetch for the Alrø station is in the range of 1.5-2 km.

Owing to the nature of the nearby land surfaces around the stations (see Sections 6.1-6.3), it makes some sense to assume that the influence of the nonidealities on the velocity ratios does not change with wind direction in the sector interval of interest. To get a well-defined fetch to use in the comparison with the model in Section 5.6, we therefore define the fetch for which $U_A = U_G$ to be zero. The effective water fetch is

therefore to be understood as the actual water fetch for Alrø minus the fetch where $U_A = U_G$. For velocity group 1 the zero effective water fetch appears in sector 39, while for groups 2 and 3 it is in sector 37.

The curves in Fig. 6.6 describe predictions based on the model discussed in Section 5.6. However, establishing these predictions involves more considerations and assumptions than do the simple models described in Section 5.6.

Equations (5.15) through (5.21) allow us to determine the ratio between the up- and the downstream surface stresses, from which the corresponding velocity ratio can be calculated as

$$u_2(z)/u_1(z) = \frac{u_{*o2}\left(\ln\frac{z}{z_{o2}} - 2\frac{z}{H_2}\right)}{u_{*o1}\left(\ln\frac{z}{z_{o1}} - 2\frac{z}{H_1}\right)} \quad . \qquad (6.1)$$

To use the relevant equations in Section 5.5 and (6.1) we must specify (z_{o2}, H_2, z_{o1}, H_1). We know the velocity and the surface roughness at Gylling Næs, which we shall take as z_{oG} = 0.5 cm (compare Fig. 6.2.b). In keeping with that the model in Section 5.5 is for neutral stability only; u_{*oG} is determined from (4.3) as

$$u_{*oG} = U_G\,(17.5\text{ m}) \cdot 0.4/\ln(17.5/0.005) \quad .$$

In (6.1) z_{o1} and H_1 are the equilibrium length scales for the boundary layer established over eastern Jutland. Clearly z_{oG} is too small to be z_{o1}, which must be considered to be of the order 5 to 10 cm (rolling farmland, with dispersed forests, living fences, and cities). As discussed in Section 6.2, z_{oG} characterises the rather smooth field just around the Gylling Næs mast. The area on Gylling Næs adjacent to this field is precisely of the type that can be described by the aforementioned roughness length, 5-10 cm (see Fig. 2.2.b and 6.5). As a simplified model we shall, therefore, consider z_{oG} as descrip-

tive for a small subarea imbedded in the general land area described by z_{o1}. The distance to the change in roughness is ~ 300 m. This estimate is based on Fig. 6.2.b, which shows that the internal boundary layer height at the position of the Gylling Næs mast must be larger than ~ 20 m, since the z_{oG}'s determined from the lower two measuring heights and the upper measuring heights coincide in the sector interval considered. On the other hand, the description of the sites in Section 6.2 indicates that the roughness change cannot take place much farther away from the mast than 200 m.

Using the above mentioned knowledge of the subarea surrounding Gylling Næs we are now able from U_G and u_{*oG} to determine the proper u_1 and u_{*o1} to be applied in (6.1). We use

$$\frac{u_{*oG}}{u_{*o1}} = 1 + \frac{\ln(m)}{\ln(h/z_{oG})} \quad , \; m = \frac{z_{oG}}{z_{o1}}$$

$$\frac{U_G(17.5m)}{U(17.5m)} = \left(\frac{u_{*oG}}{u_{*o1}}\right)/\left(1 + \ln(m)/\ln\left(\frac{17.5}{z_{oG}}\right)\right) \quad , \tag{6.2}$$

which is just the surface layer forms of the equations described in Section 5.6, and where we take h ≈ 25 m.

With assumed values for z_{o1} and the given values of z_{oG} and u_{*oG}, Eq. (6.2) now allow us to determine u_{*o1} and H_1 and thereby through (5.1) the geostrophic wind G.

Next, we need to determine z_{o2} and H_2, i.e. the parameters pertaining to the over-water conditions. No satisfactory theory exists for the roughness length of a confined water surface, as Horsens fjord. We will start by applying the Charnock relation

$$z_o = \alpha \, u_{*o}^2/g, \tag{6.3}$$

where g is the acceleration due to gravity and we will use $\alpha = 1.5 \cdot 10^{-2}$.

In summary: In the model calculations, the transfer is believed to take place between z_{o1} and z_{o2}, while the data obtained refer to z_{oG} and z_{o2}. Figure 6.5, schematically, shows how the various parameters enters into the problem.

Our remaining problem is that although we know the approximate range of values for z_{o1}, we do not know which actual value to use. Therefore, the U_A/U_G behaviour was calculated as dependent on Δx assuming different z_{o1}-values. Table 6.1 shows relevant parameters for different choices of z_{o1}. The resulting U_A/U_G-

Table 6.1. Shows relevant model parameters for different choices of z_{o1}, when $z_G = 5 \cdot 10^{-3}$ m and $u_{*oG} = 0.56$ m/s. G is determined from (5.1), u_{*o2} from (5.1) in connection with (6.3). The ratio U_1/U_G is a factor with which the model predicted U_A/U_1 must be multiplied for comparison with the U_A/U_G data points. The value for u_{*oG} is obtained from (6.2) by use of U_G averaged over all velocity group 3 situations.

z_{o1}[m]	10^{-2}	$2\ 10^{-2}$	$4\ 10^{-2}$	$7\ 10^{-2}$	10^{-1}
u_{*oG}[m/s]	0.56	0.56	0.56	0.56	0.56
u_{*o1}[m/S]	0.61	0.67	0.74	0.81	0.86
H_1[m]	5083	5575	6175	6750	7167
U_1/U_G	0.997	0.992	0.986	0.979	0.976
G[m/s]	18.5	19.36	20.46	21.5	22.6
u_{*o2}[m/s]	0.49	0.52	0.55	0.58	0.61
z_{o2}[m]	$3.7 \cdot 10^{-4}$	$4.0 \cdot 10^{-4}$	$4.5 \cdot 10^{-4}$	$5.0 \cdot 10^{-4}$	$5.6 \cdot 10^{-4}$
H_2[m]	4083	4333	4583	4833	5083

ratios are shown for two values of z_{o1} in Fig. 6.6, from where it is seen that $z_{o1} \sim$ 4-6 cm seems to predict the measured values of U_A/U_G for large effective fetches. However, the comparison shows as well that the model estimates of U_A/U_G increases more slowly with fetch than the data indicates.

A possible reason for this phenomenon is that for a confined water surface the water roughness increases with fetch. Only for large fetches the z_o-value will be in equilibrium with the wind field. Therefore, the measured points on Fig. 6.6 corresponds to a situation where z_{o2} increases with fetch until it reaches the "equilibrium" value given by (6.3), while the solid curves correspond to model predictions with a constant z_{o2}.

Kitaigorodskiy (1973) and Hedegaard (1975) suggest the following model for this approach to equilibrium:

In wave growth theories the height, z_i, at which the wind speed equals the phase speed of the wave, c, plays an important role, Kitaigorodskiy (1973).

Consider a wave travelling with the wind at frequency, ω, and phase speed $c(\omega)$. For such a wave we can estimate an associated $z_i(\omega)$ and $z_o'(\omega)$ from:

$$c(\omega) = (u_{*o}/k)\ln(z_i(\omega)/z_o'(\omega)) \quad ,$$

or

$$z_o'(\omega) = z_i(\omega)\exp(-k \cdot c(\omega)/u_{*o}) \quad . \tag{6.4}$$

Next, we assume that $z_i(\omega)$ is related to the wave spectrum, $S(\omega)$, as

$$z_i^2(\omega)d\omega \propto 2S(\omega)d\omega \tag{6.5}$$

leading to

$$z_o'^2(\omega)d\omega \propto 2S(\omega)\exp(-2k \cdot c(\omega)/u_{*o})d\omega \quad . \tag{6.6}$$

We now use the deep water approximation to $c(\omega)$, and integrate over ω to obtain z_o;

$$c(\omega) = g/\omega$$

$$z_o = (\int_o^\infty z_o'^2(\omega)d\omega)^{1/2} \propto 2(\int_o^\infty S(\omega)\exp(-2kg/\omega u_{*o})d\omega)^{1/2}. \quad (6.7)$$

To integrate (6.7) we need an expression for $S(\omega)$ (Kitaigorodskiy (1973)),

$$S(\omega) = \begin{cases} \beta\, g^2\, \omega^{-5} & \omega > \omega_o \\ 0 & \omega < \omega_o \end{cases}, \quad (6.8)$$

where β is a constant.

In (6.8) ω_o is known to be fetch dependent. From Hasselmann et al. (1973) the following relation is used by Hedegaard (1975)

$$\tilde{\omega}_o = 2\pi \cdot 1.3\, \tilde{x}^{-0.33}, \quad (6.9)$$

with

$$\tilde{\omega} = \omega \cdot u_{*o}/g \text{ and } \tilde{x} = x \cdot g/u_{*c}^2 .$$

From (6.3) through (6.9), Hedegaard (1975) arrives at

$$z_o = \alpha \frac{u_{*o}^2}{g} F(\tilde{\omega}_o), \quad (6.10)$$

with

$$\alpha \propto \frac{\sqrt{3\beta}}{2k^2} .$$

$$F(\tilde{\omega}_o) = (1 - \exp(-2k/\tilde{\omega}_o)(1 + \frac{2k}{\tilde{\omega}_o} + \frac{1}{2}(\frac{2k}{\tilde{\omega}_o})^2 + \frac{1}{6}(\frac{2k}{\tilde{\omega}_o})^3))^{1/2}$$

$F(\tilde{\omega}_o)$ is plotted versus $\tilde{\omega}_o$ in Fig. 6.7, which shows that for small $\tilde{\omega}_o$ (i.e. for large fetches and/or small u_{*o}) z_o will ap-

proach its equilibrium value given by (6.3). We shall, therefore, assume α to be $1.5 \cdot 10^{-2}$.

As we estimated z_{o2} before by iteration from (6.3) and (5.1), we can do the same now by specifiying $z_{o2}(x,u_{*o2})$ through (6.10) and specify $u_{*o2}(x,z_{o2})$ from the model in Section 5.6, when u_{*o1} and z_{o1} are specified.

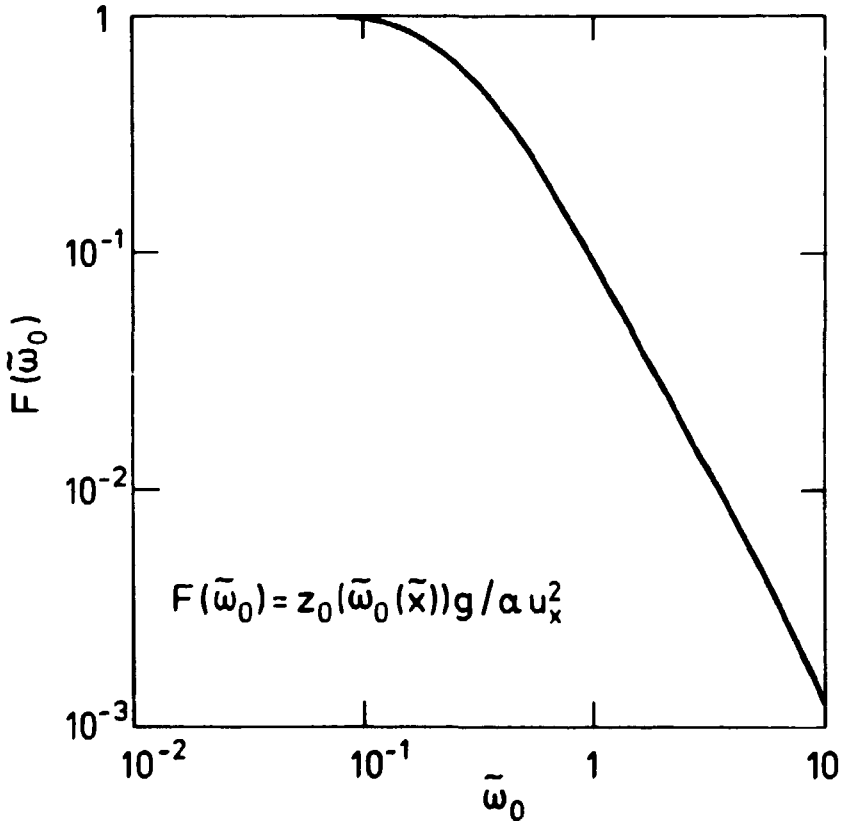

Fig. 6.7. The normalized z_o-value for water for finite fetches relative to the value for infinite fetches, plotted versus $\tilde{\omega}_o$, the nondimensional peak frequency for the wave spectrum.

Results of the iteration schemes are displayed in Table 6.2 with $z_{o1} = 0.04$ m and $u_{*o1} = 0.74$ m/s, and the resulting $z_{o2}(x)$ is shown in Fig. 6.8.

It is important to realize that we do not really have a theory that describes the change of terrain roughness situation when

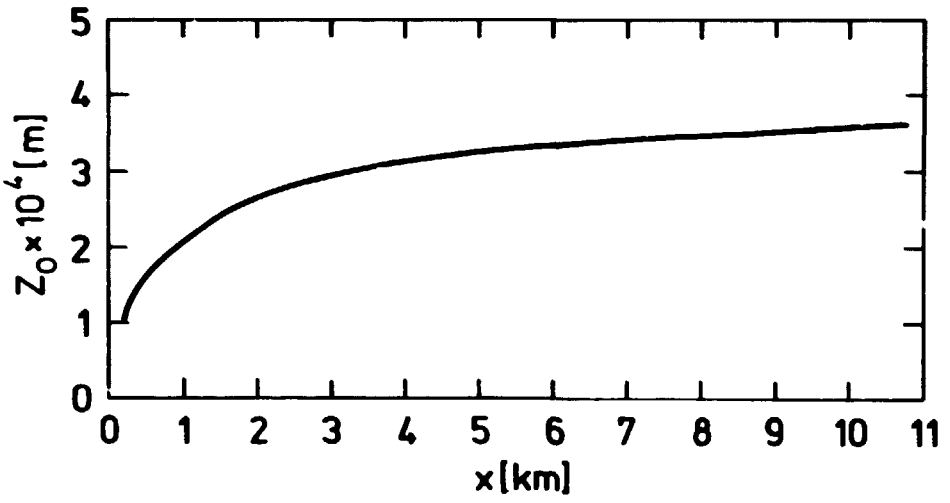

Fig. 6.8. The figure shows the fetch dependency of z_o for water if z_o is assumed to be determined by (6.10) and the stress on the water is assumed to be in equilibrium with z_o, and obtained through the matching equation of roughness change (6.1). The figure is based on Table 6.2.

the downstream roughness is stress and fetch dependent. The suggested values of z_{o2} and u_{*o2} in Table 6.2 must be considered output from a reasonable but nonproven combination of a change of roughness theory and a theory for the roughness of a water surface.

If we use the simple roughness change models for a water surface we would expect that for the water roughness length we would have to use a characteristic value pertaining to the fetch we are studying. What a characteristic value is, of course, is not well specified. In Table 6.2 we have shown the resulting U_A/U_G values when the characteristic z_{o2}-value is taken as $z_{o2}(x)$ and $z_{o2}(x/2)$, where x is the fetch at which U_A/U_G is estimated. It is seen that the two sets of estimates differ very little.

Finally, the broken curve in Fig. 6.6 shows the effect of using $z_{o2}(x/2)$ to determine U_A/U_G (x) with $z_{o1} = 0.04$ m.

From Fig. 6.6 it is seen that explaining the U_A/U_G values in terms of a water fetch change for the Alrø station only has the following drawbacks:

Table 6.2. Estimates of fetch-dependent water z_o-values for velocity group 3 data with z_{o1} = 0.04 m. The first 6 columns are the results found when z_{o2} is determined through Charnock's formula (6.3) and $u_{*o2}(x\to\infty)$ The following 4 columns show the results of using (6.10) using $z_{o2}(x)$ instead. The two last columns finally show the effects of and $z_{o2}(x/2)$ as characteristic water fetch when U_A/U_G is modelled (see also Fig. 6.5). $\Delta x = x - x(U_A=U_G)$, corresponding to the effective fetch.

x [m]	Δx [m]	h(x) [m]	U_{AL}/U_{GYL}	u_{*o2} [m/s]	$z_{o2}\cdot 10^4$ [m]	$\tilde{\omega}_o$	$F(\tilde{\omega}_o)$	$z_{o2}\cdot 10^4$ [m]	u_{*o2} [m/s]	U_A/U_G ($z_{o2}(x)$)	U_A/U_G ($z_{o2}(x/2)$)
192.8	111	30.9	1.023	443	4.5	0.361	0.44	1.00	0.390	1.030	1.034
435	354	61.8	1.06	0.460	4.5	0.290	0.57	1.52	0.421	1.074	1.078
1560	1480	185	1.116	0.484	4.5	0.202	0.77	2.46	0.461	1.130	1.134
2834	2750	309	1.158	0.491	4.5	0.170	0.85	2.91	0.478	1.151	1.155
6485	6400	618	1.186	0.505	4.5	0.132	0.92	3.38	0.495	7.177	1.181
8542	8460	772	1.195	0.509	4.5	0.123	0.93	3.51	0.50	1.185	1.188
10750	10670	926	1.202	0.512	4.5	0.114	0.95	3.66	0.507	1.191	1.194
-	-	4583	1.404	0.548	4.5	-	1	4.50	0.548	-	-

Table 6.3. The table shows measured (Meas.) and modelled (Md.) ratios of U_A/U_G for the 3 velocity groups under the assumption of several roughness changes. The last 5 columns give distance from the masts indicated to the roughness changes, lw means land → water and wl vice versa. GYL 1 is the distance to mainland Jutland, GYL2 is the distance to the farther coasts of Alrø or Hjarnø (compare Fig. 2.1), GYL3 to the nearest coast of these islands and GYL4, to the coast of Gylling Nas. For sector 40 U_A/U_G is modelled with/without considering the Hjarnø land surface, owing to the fact that the trajectory just follows the edge of Hjarnø.

	$U_A \longrightarrow$ 1		$U_A \longrightarrow$ 2		$U_A \longrightarrow$ 3		Distances from masts to surface changes				
Sector	U_G Meas.	Md.	U_G Meas.	Md.	U_G Meas.	Md.	Alrø,lw [m]	GYL,wl 1,[m]	GYL,wl 2,[m]	GYL,wl 3,[m]	GYL,wl 4[m
36	0.94	1.02	0.97	1.04	0.99	1.02	1400	45000			2000
37	0.97	1.03	1.00	1.06	1.03	1.03	1500	40000			2100
38	0.98	1.10	1.04	1.08	1.04	1.07	1500	14800			2100
39	1.01	1.15	1.09	1.14	1.12	1.12	3600	12400			2200
40	1.06	1.19/ 1.17	1.11	1.17/ 1.16	1.13	1.17/ 1.13	4000	9600	8500/-	6600/-	2500
41	1.12	1.20	1.15	1.17	1.17	1.17	4500	9600	9000	7100	2500
42	1.14	1.21	1.17	1.16	1.15	1.15	5200	11600			2600
43	1.18	1.17	1.17	1.17	1.17	1.16	6400	13400			2700
44	1.21	1.20	1.19	1.18	1.18	1.17	7600	16200			3000
45	1.25	1.23	1.23	1.21	1.17	1.17	10400	20000			3000
46	1.30	1.25	1.25	1.23	1.19	1.19	10800	14400			3400

a) The increase in the modelled velocity ratio with fetch is too slow even when the fetch dependency of z_{owater} is included.
b) The best fitting value for z_{o1} = 0.04 m is a bit less than one would expect.

The most likely explanation for point a) is that the change in water fetch for the Gylling Næs station also influences the data. As described above, the small effective fetches in Fig. 6.6 correspond roughly to sectors 36-40. Figures 6.13 and 6.14 show that in this sector interval the water fetch between the Gylling Næs coast and main land Jutland reduces strongly from about 50 km to 10 km.

In Table 6.3 the distance from the two masts to the main surface changes are summarized. It is further indicated when the change is of the type land → water or water → land.

To use this information, we notice that our change of roughness model can be used for multiple roughness changes without violating any of the assumptions for its derivation. This means that if the air blows across n step-changes in roughness, then we can find U_n/U_1 as

$$U_n/U_1 = \prod_{i=1}^{n-1} U_{i+1}/U_i \qquad (6.11)$$

Based on the model and the fetch information we can therefore determine U_A/U_G as $U_A/U_J \cdot (U_G/U_J)^{-1}$ where U_J stands for the velocity at 17.5 m above mainland Jutland. Figure 6.5 shows schematically how the different surface changes influences our data.

As before z_{o1} is unknown and we have to try a number of plausible values. As discussed above, it is also fairly uncertain how the characteristic roughness length over water must be estimated. Based on Fig. 6.8 we have chosen to estimate the characteristic value as z_{o2} as ~ $z_{o2}(x=\infty) \cdot 0.7$ corresponding to a water-

fetch of the order of 6 km. With this choice, z_{o1} is the only unknown remaining. It is determined by calibrating the model U_A/U_G against the measured values for sector 45, velocity group 3, resulting value is $z_{o1} = 0.07$ m. The parameter values used for the three velocity groups are summarized in Table 6.4.

Table 6.4. Parameter values used to calculate the velocity ratios in Table 6.3 and Fig. 6.10. $z_{o2}(\infty)$ was estimated for infinitely l[illegible]ater fetches; based on a fetch behaviour of z_{o2} as depicted in Fig. 6.8, the characteristic z_{o2} was estimated as $\sim 0.7 \cdot z_{o2}(\infty)$ and u_{*o2} was calculated accordingly. The values for G and u_{*o1} were estimated on basis of the average U_G for the different velocity groups, including the roughness change around the Gylling Næs mast.

Velocity group	z_{o1} [m]	u_{*o1} [m/s]	z_{ow} [m]	u_{*ow} [m/s]	$u_{*ow}(\infty)$ [m/s]	$z_{ow}(\infty)$ [m]	G [m/s]
1	0.07	0.32	$4.5 \cdot 10^{-5}$	0.19	0.20	$5.8 \cdot 10^{-4}$	7.8
2	0.07	0.54	$1.4 \cdot 10^{-4}$	0.35	0.36	$1.9 \cdot 10^{-4}$	13.8
3	0.07	0.81	$3.5 \cdot 10^{-4}$	0.57	0.58	$5.0 \cdot 10^{-4}$	21.5

To estimate the resulting velocity ratios we now assume that all water surfaces in the problem have the water roughness as given in Table 6.4 and all land roughness values equal 7 cm, aside from the subarea around the Gylling Næs mast, of course, which still has $z_{oG} = 0.5$ cm.

Figure 6.9 shows how the velocity ratios vary with fetch for the land → water and the water → land situations for velocity group 3.

Based on Fig. 6.9 and the corresponding curves for the other velocity groups we can estimate the velocity ratios sector by sector and compare with measurements. This is done in Table 6.3 and in Fig. 6.10 for the velocity group 3 data as well.

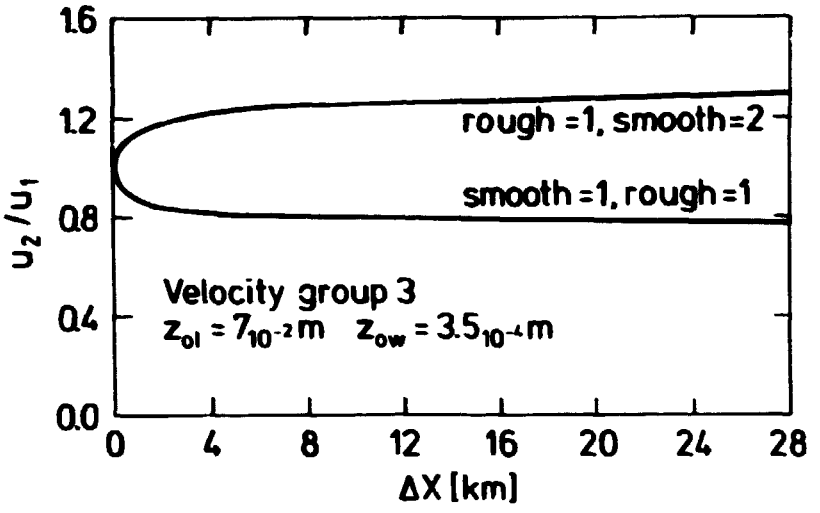

Fig. 6.9. The ratio between the downstream (2) and upstream (1) velocity 17.5 m above terrain for roughness length values pertaining to the velocity 3 data (Index w means water and index l means land).

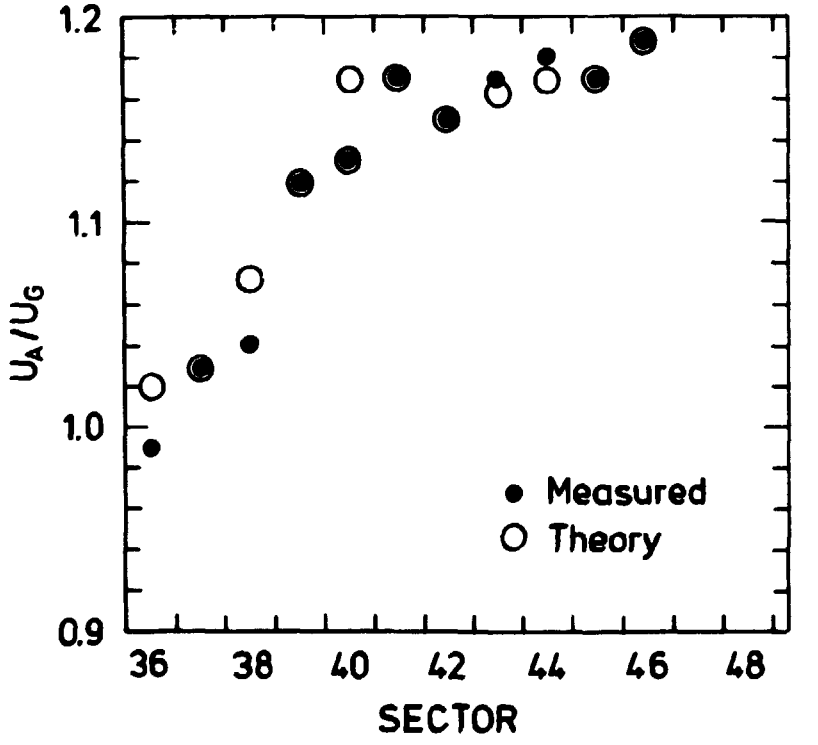

Fig. 6.10. The theoretical and measured values for U_A/U_G for velocity group 3 data. The figure is based on Table 6.3.

From this comparison we conclude the following:

a) For the velocity group 3 data the agreement with theory is good. Note the ambiguity in sector 40. This is due to the running over the far east coast of Hjarnø of the Gylling Næs trajectory (see Fig. 6.14). The high value in Fig. 6.10 corresponds to the assumed passing over Hjarnø in this sector of the trajectory; the low value which fits the measurements, corresponds to that the trajectory does not see Hjarnø.
b) For velocity group 3 data it is further seen that the model values tend to be above the measured values for sectors 36-38. From Table 6.3 it is seen that this tendency is enhanced for the low velocity group data. It is difficult to give a good explanation for this phenomenon, especially for the low velocity data, where diabatic processes may be of importance, in contrast to the model's assumption of neutrality. However, it is worth noticing that if the model reaches an equilibrium condition over the new surface at fetches of the order of 20-30 km rather than at fetches of the order 100 km then the difference between data and model would be reduced. The reason for this is that the long water fetches from sector 36-39 for the Gylling Næs area would then increase the modelled U_G sufficiently to reduce U_A/U_G. At present, however, the complexities associated with the data and simplicity of the model precludes any firm conclusion.
c) The ability of the model to describe the detailed behaviour of the measured data for velocity group 3 in Figure 6.10, indicates that the model works well for fetches that are not too long, say 30 km. It further shows that the approach for handling multiple roughness changes used here is applicable in practise.

6.5. Differences in cross isobaric angle

In Chapter 5 we discussed, from a more theoretical point of view, some effects which could be responsible of the differences in wind direction between two measuring sites, being suf-

ficiently close to be exposed to the same synoptic conditions. The effects mentioned can be separated into two groups. a: Differences in surface characteristics upstream of the two sites, causing the structure of the PBL to be different at the two sites. This in turn causes differences in the cross isobaric angle as determined by the resistance laws for the planetary boundary layer. b: Differences in topography causing excess/deficit of momentum, and a resulting change of wind direction downstream of the topography change due to the redistribution of the momentum change among the two wind components, one along the isolines of topography, the other one perpendicular to.

A major question concerning the effects "a" was that of the fetches required before a change in surface conditions would result in a measurable change in cross isobaric angle. This point is crucial as the fetches with different upstream surface conditions usually are short, of the order 5 to 50 km. As mentioned in Section 5.4.1, it is an interesting point to note that the change in cross isobaric angle by change of surface roughness is usually opposite to that caused by a change in the thermal properties of the surface, which usually accompanies a change in surface roughness. But while the change associated with the former effect required fetches of the order 50 to 100 km to be measurable, as estimated from models, the latter effect seemed to be able to create measurable changes in cross isobaric angle with fetches of only 5 to 10 km. In the fetch range 5-50 km of different conditions, there should thus be a measurable change in cross isobaric angle due to altered thermal properties of the surface. For fetches greater than ~ 50 km an opposite change in the cross isobaric angle would take place due to the associated roughness change, thus leaving the cross isobaric angle largely unaltered for larger fetches.

The effect of changing topography "b", was treated in Section 5.4.2, and was seen to produce measurable changes in wind direction, primarily for offslope flow, and only for cases with a depth of the perturbed velocity layer less than 500 to 600 m. We, therefore, expect this effect of changing the wind direction

only to be active for relatively short distances downstream of the slope.

We now turn to the observed differences in the average wind directions. These are shown in Fig. 6.11 as $\Delta\bar{\theta} \equiv \bar{\theta}_G - \bar{\theta}_A$, as a function of $\bar{\theta}_G$, where subscript "G" refers to Gylling Næs, "A" to Alrø. Figure 6.12 shows the interpretation of $\Delta\bar{\theta}$ with respect to average cross isobaric angles. Here $\vec{G}$ is the geostrophic wind

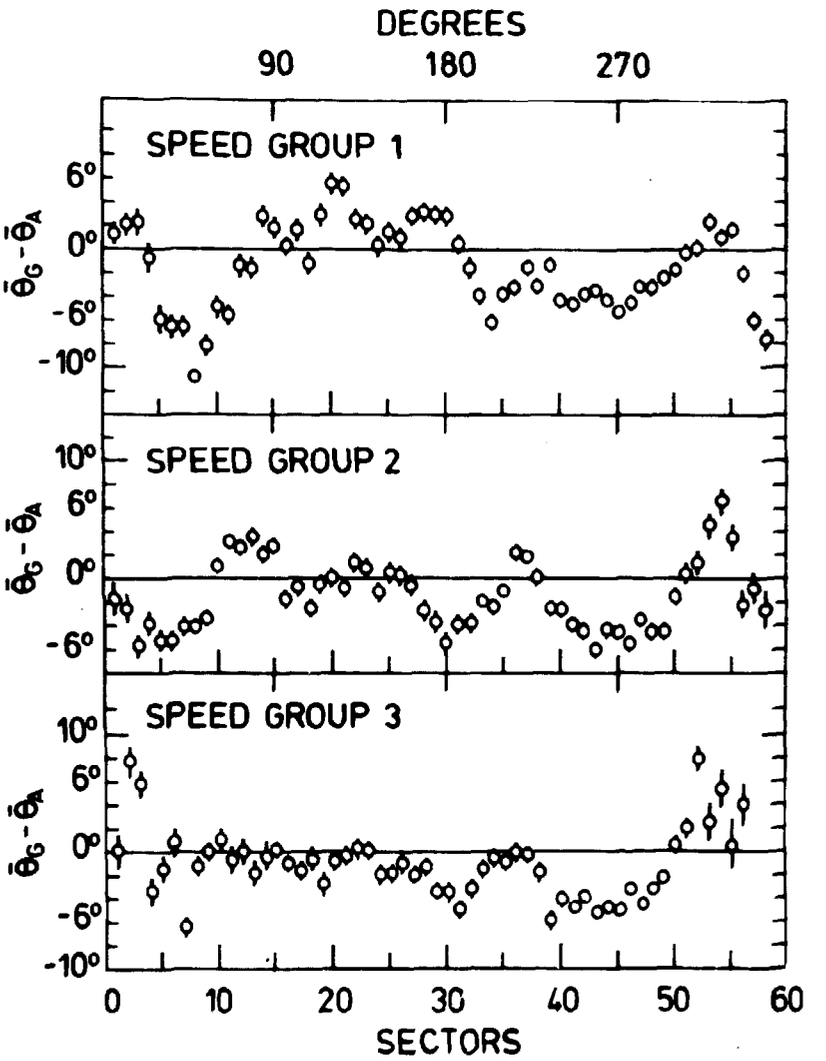

Fig. 6.11. Difference in mean wind direction between Gylling Næs and Alrø as a function of the direction at Gylling Næs. $\bar{\theta}_G$ is the mean direction at Gylling Næs, $\bar{\theta}_A$ at Alrø. The uncertainty in determining the mean is shown as a vertical bar (cf. Fig. (6.1)).

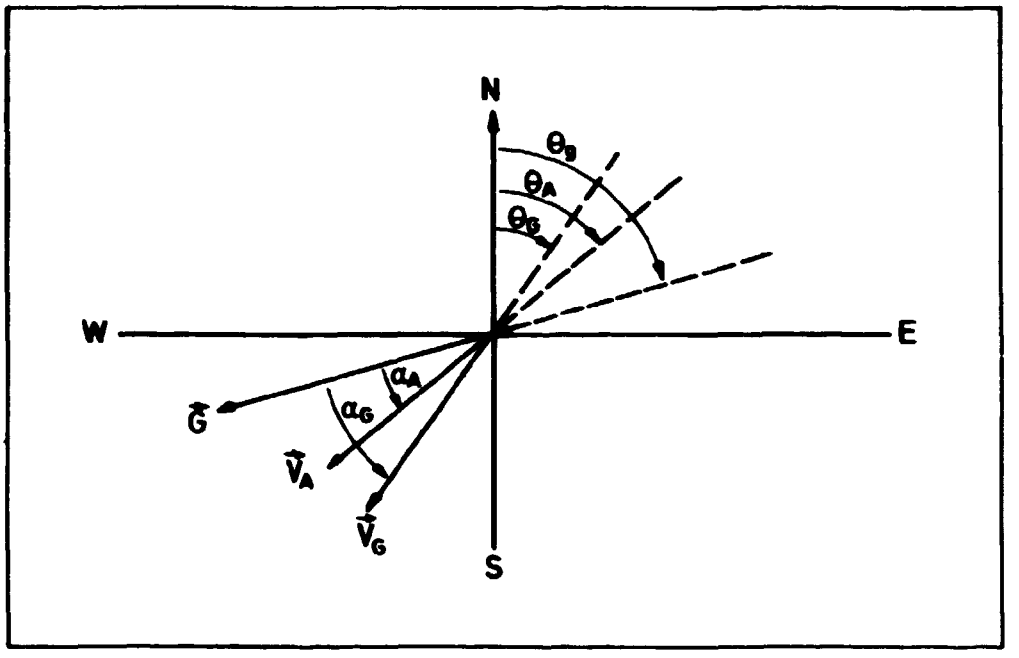

Fig. 6.12. Interpretation of the directional difference $\Delta\bar{\theta}$. (For explanation, see text).

with direction θ_g, and the average cross isobaric angles are defined as $\bar{\alpha}_i = \bar{\theta}_g - \bar{\theta}_i$, i = A,G. We thus have $\Delta\bar{\alpha} \equiv \bar{\alpha}_G - \bar{\alpha}_A = \bar{\theta}_A - \bar{\theta}_G = -\Delta\bar{\theta}$, where we have used the identity of $\bar{\theta}_g$ at the two sites. This means that when $\Delta\theta$ is positive, then Alrø has the greater cross isobaric angle, and when $\Delta\theta$ is negative, then the cross isobaric angle at Gylling Næs is the greatest.

In Figs. 6.13, 6.14, and 6.15 we have collected some topographical information from the area. Figures 6.13 and 6.14 are maps of the area with different scales, while Fig. 6.15 shows the major contour lines with intervals at 25 m.

From Figs. 6.13 and 6.15 we see that for the approximate direction interval (90°, 156°), the upstream surface conditions are much alike, and there should, therefore, be no turning due to stability effects. Also, the differences in heights are small, less than 25 m. Nonetheless, for wind speed group 1 we see from Fig. 6.11 values of $\Delta\bar{\theta}$ as high as ~ 6° in this interval, while for the other two speed groups the values of $\Delta\bar{\theta}$ are small, generally less than ~ 2°. The observed differences for the small

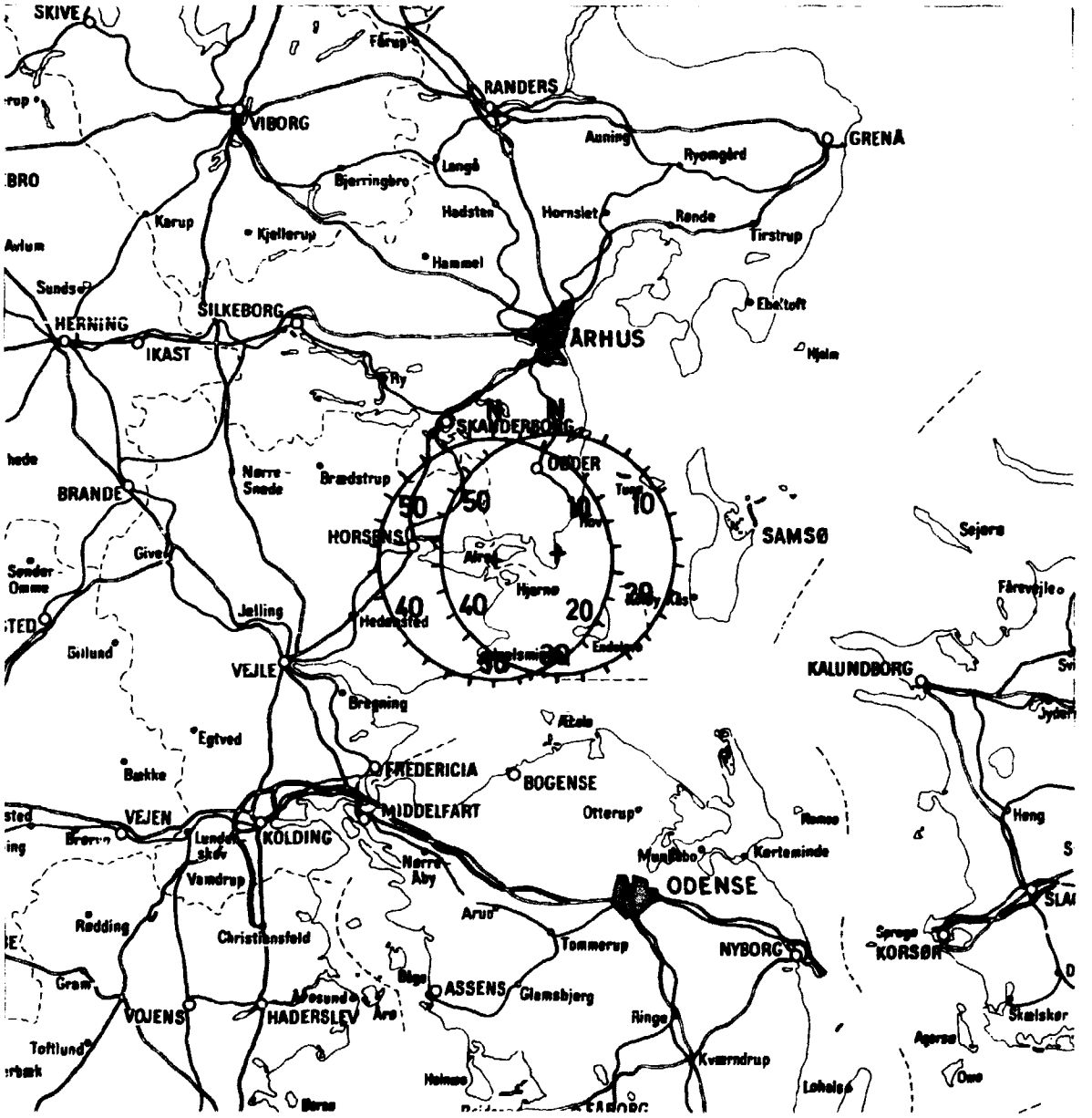

Fig. 6.13. Map of the area covering distances of about 100 km from the measuring sites. The scale is 1:1.000.000. The measuring positions are marked with crosses. The sector rose around each station is indicated.

wind speeds must be caused by topographical effects due to the island Hjarnø, and perhaps Alrø itself. These effects are not of the type discussed in Section 5.4.2, which should also be present for higher wind speeds. For the sectors 17 and 25, where the flow passes through the two sounds, there is neither any ap-

Fig. 6.14. Magnification of the map in Fig. 6.13 enlarged to a scale of 1.200.000.

preciable turning of the wind for wind speed group 1, which is in accordance with our expectations.

From Fig. 6.11 we see more or less regular patterns in wind direction changes. For some intervals they are close to being sinusoidal, and, therefore, it is natural to attempt an explanation of the observed phenomena by using the simple model developed in Section 5.4.2. The contour lines, as shown in Fig. 6.15, are irregular, but we do not expect irregular deviations from straight contour lines to be damaging to the model concept provided we consider directions some distance downstream. In Fig. 6.15 we have drawn the average direction of three major 50-m

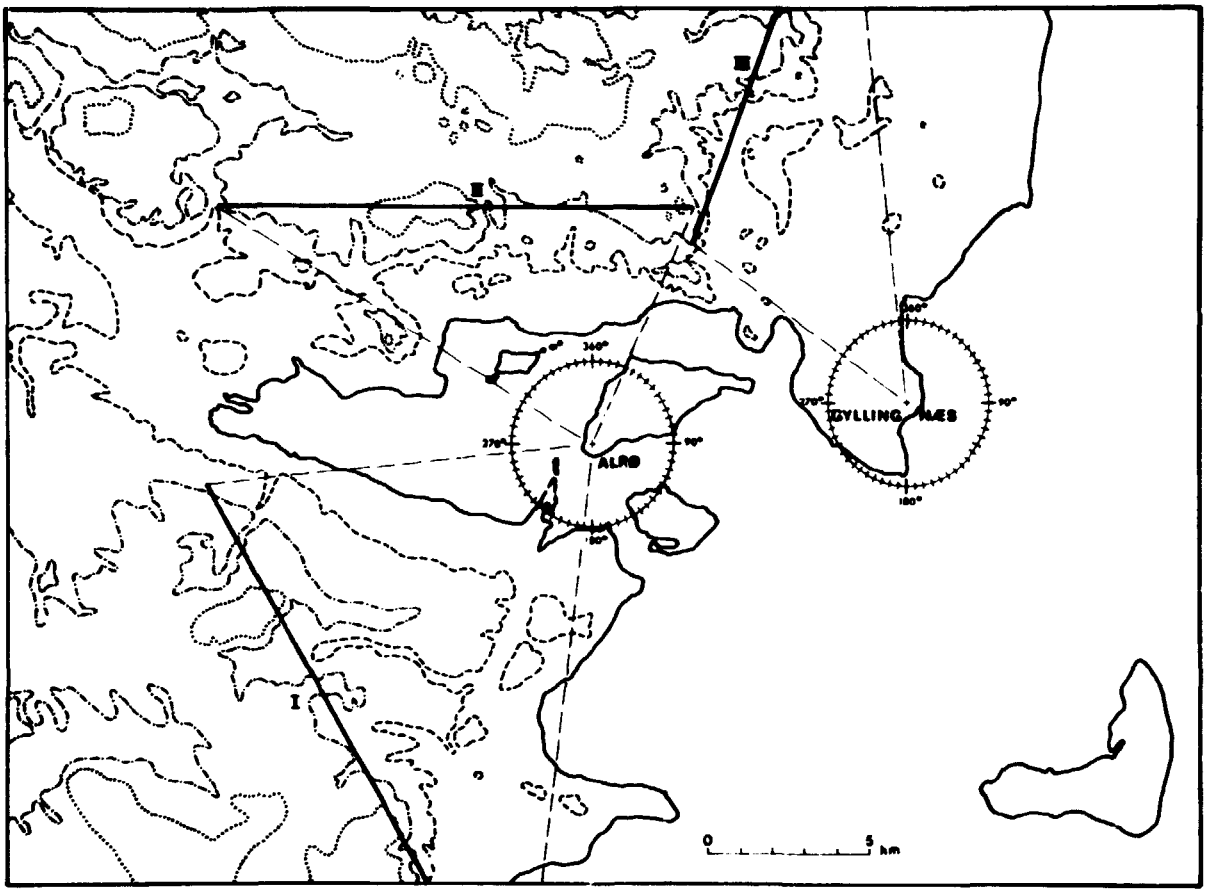

Fig. 6.15. The major contour lines in the Horsens fjord area. Mean sea level: ——; 25 m: ---; 50 m: -·-·-; 75 m: ····. The generalized directions of the contour lines in the three major areas with sloping terrain are shown as heavy lines with the directions: I: $\theta_c = 150^o$; II: $\theta_c = 270^o$; III: $\theta_c = 200^o$. The subtending sectors are shown as dashed lines.

contour lines, indicated as lines I, II, and III. Inland from these idealized contour lines the height generally rises to above 75 m, in some cases up to above 100 m. As the measuring sites, and their surroundings, are close to mean sea level, we have a net height decrease which corresponds well to the 60 m used in the model (Section 5.4.2).

The directions of the generalized contour lines are: I: $\theta_C = 150^o$, II: $\theta_C = 270^o$, III: $\theta_C = 200^o$. Alrø is downstream of line I for directions in the interval (186^o, 264^o), and downstream from line II for directions in the interval (300^o, 24^o).

For both direction intervals, the Gylling Næs site is downstream of the generalized contour lines only for a small fraction, and for these directions it is about twice as far downstream as compared to Alrø. For the remaining part of the intervals, the flow at Alrø has not passed the generalized contour lines. Except for the interval (306^{o}, 354^{o}), we shall consider Gylling Næs to be unperturbed by topographical effects, and shall consider it as a proper reference direction for the conditions upstream of the topographical height change influencing Alrø. In the above interval Gylling Næs is situated downstream of generalized contour line III at a distance comparable to the distance of Alrø downstream of contour line II. By using the model on Gylling Næs for contour line III in the interval (306^{o}, 354^{o}) we are able to calculate an upstream unperturbed direction for Alrø.

We have compared the model predictions for $H = 60$ m and $\lambda = 300$ m (cf. Section 5.4.2) with the observed turning angles for wind speed group 2, Fig. 6.11. In Fig. 6.16 we have plotted these observed values against the predicted model values from the intervals (186^{o}, 264^{o}) and (300^{o}, 24^{o}). Except for the interval (306^{o}, 354^{o}) we consider $\bar{\theta}_G$ as the unperturbed direction upstream, equivalent to $\bar{\theta}$ in Section 5.4.2. For the interval (306^{o}, 354^{o}) we use for the unperturbed direction $\bar{\theta} = \bar{\theta}_G + \Delta\beta_G$, and thus hold

$$\Delta\bar{\theta} = \bar{\theta}_G - \bar{\theta}_A = \bar{\theta} - \Delta\beta_G - \bar{\theta}_A = \Delta\beta_A - \Delta\beta_G ,$$

where $\Delta\beta_i$, $i = A,G$, is the directional change downstream of the topographical height change at the two sites.

The model-direction change in Fig. 6.16 generally predicts the phase correctly, while there are some differences between amplitudes. It is dissatisfying that we are unable to use the model to bridge the gap in the interval (270^{o}, 296^{o}), where the observed regularity of the directional change indicate that an identical process to that operating outside this interval is responsible for the directional change also in this interval. From Fig. 6.11 we also see that the negative values of $\Delta\theta$ for wind speed group 2 extends below 180^{o}, down to directions close

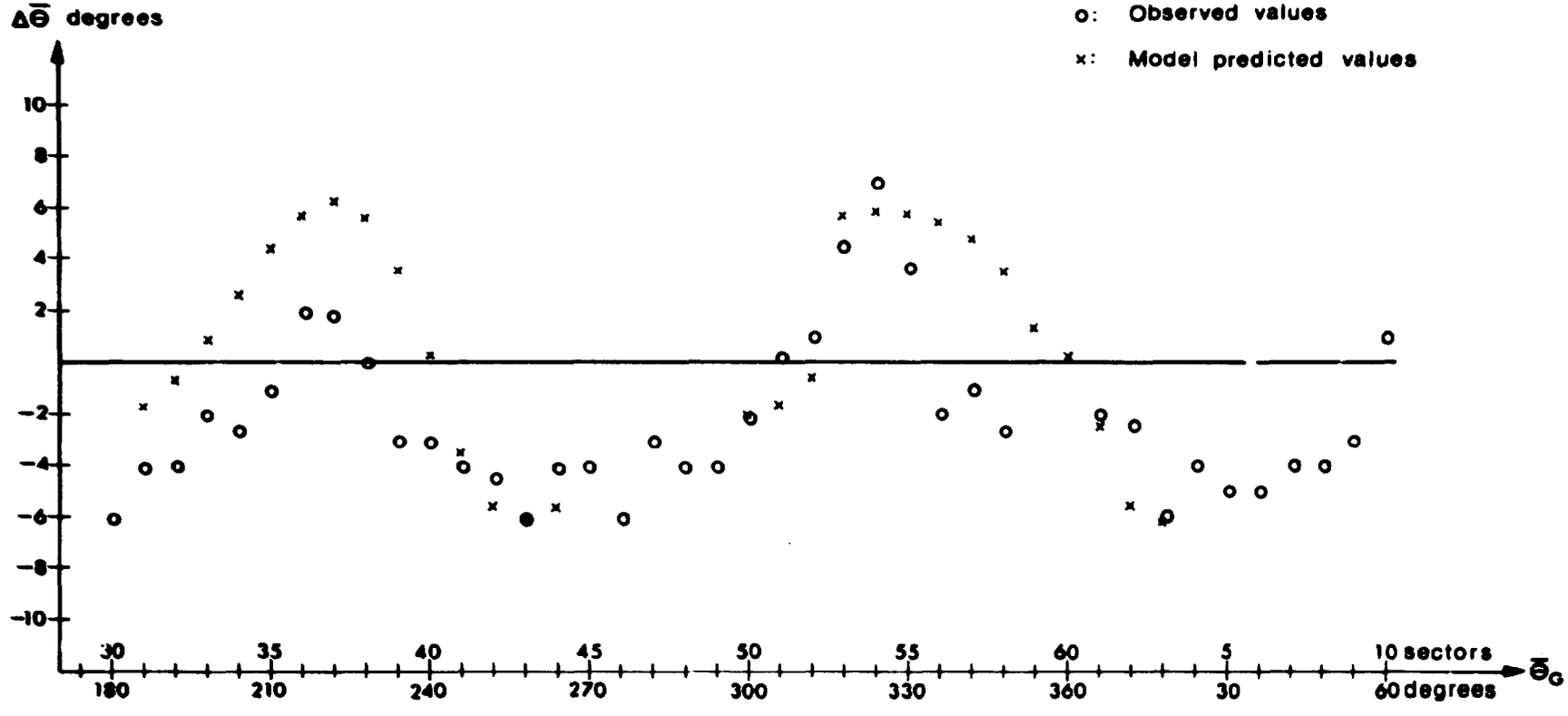

Fig. 6.16. Observed and predicted directional changes for wind speed group 2 shown against the direction at Gylling Næs. For details on the model of directional change due to topography, see Section 5.4.2. The model was applied with H = 60 m, and λ = 300 m, with the θ_c directions shown in Fig. 6.15.

to 160°. It is difficult to explain the directional change in this interval, (162°, 186°), by the present model, cf. Fig. 6.15. It should, however, be noted that wind speed group 1 does not have negative $\Delta\overline{\theta}$ values in this interval. Also, it should be pointed out that the upstream surface characteristics at the two sites are much alike for this interval, so stability must be ruled out as a cause of directional change in the interval.

Other points showing the inability of the model to predict all the observed directional changes can easily be found. Considering the crudeness of the model and the complexity of the area, we are not too much alarmed by that. Recalling our previous discussions, the only effect which could cause directional change in the intermediate fetch range ~ 5 to ~ 50 km was stability differences. We have, of course, applied stability as the cause of the observed directional differences, but we found it impossible to formulate any comprehensive explanation of the directional differences based on stability alone. This, by no means, rules out stability as a cause of the directional change. This is even more so as the model of directional change due to topography is dependent upon stability in that the relation between λ and downstream distance most likely is dependent upon stability, cf. Section 5.4.2.

We shall bring forward one case where it is unlikely that stability differences could be the cause of the directional change, but where the topographical model works well for all three wind groups. This is the interval (300°, 330°), where the only difference in upstream fetch is the 4-5 km fetch of water upstream of Alrø. Recalling the estimates in Section 5.4.1 on the transition rates, this fetch seems to be too short to produce the observed turning, even if the sign is predicted correctly.

We shall draw the following conclusion on the observed directional differences and their possible causes. a: There are clear indications of topographical influences upon the wind direction, different from the effects described by the model in Section 5.4.2 (wind speed group 1, direction interval (90°, 156°)). b: The model developed in Section 5.4.2 seems capable of describing

the directional change in a case where stability most likely must be ruled out as a cause (all wind speed groups, direction interval (300^{o}, 330^{o})). c: Neither the present model of topographical direction change, nor stability, seems capable of describing very clear directional differences (wind speed groups 2 and 3, directional interval (162^{o}, 186^{o})).

Concludingly we shall again point out the extreme complexity of the area with regard to the varying upstream conditions for nearly all directions concerning both surface characteristics and topographical height. Bearing this in mind, it is satisfying that we are able to explain some of the observed directional differences with relatively simple model concepts.

7. CONCLUSION

The purpose of this work has been to study the influence of surface inhomogeneities on a meteorological data series from two neighbouring sites. As such, to a great extent it has been an exercise in applying the different laws that have been established for the flow over both homogeneous and inhomogeneous surfaces.

Our data were not collected primarily for such a detailed study. For this reason the data set has a number of deficiencies compared with one obtained from more specialized meteorological measuring programmes: The terrain around the sites is too complex, making it difficult to sort out the different forces acting on the flows; furthermore, important parameters were measured with too low an accuracy,and some were not measured at all. Our tools for sorting out the different forces acting have been a) make careful studies of maps of the area, b) always work with simultaneous data from the two measuring stations, and c) selectively average data according to wind direction and speed classes. With respect to the missing data, of which the most import-

tant are simultaneous measurements of stability over land and water areas, we have had to hypothesize.

Based on our study we arrived at a number of conclusions:

a) Although in many respects the data are quite similar for the two stations, they do show surprising differences in some gross statistics such as in the distribution of mean and eddy flux of momentum, as is shown in Section 3.4.
b) We have been able to explain the variation in the ratio between the mean velocities from the two stations by use of theories for both the neutral planetary boundary layer and the surface boundary layer. Furthermore, we have been able to describe the change in wind velocity in response to changes in surface roughness for fetches between zero and 30 km.
c) Although for neutral stability the theories describing roughness change were efficient in yielding the average differences between wind speeds at the two stations, these theories could not explain the observed differences in wind direction. The reason for this is that we found that roughness changes demand longer fetches (20-50 km) than are available to produce changes in wind direction.
d) To describe the differences in wind direction, we studied the resistance laws for diabatic planetary boundary layers and the response times associated with change in heat flux. These effects are able to produce directional changes of the observed order, but we found it impossible to describe the observed directional differences by effects of stability alone.
e) We developed a simple model, based on continuity considerations, to describe change of direction due to changing typography. We found this model able to describe some of the observed differences in direction.

8. ACKNOWLEDGEMENT

We wish to acknowledge ELSAM, the electric utility cooperative in Jutland and Fyn which took the intitiative to and payed for the measurements used in this report. We further acknowledge useful discussions and support from Drs. N.O. Jensen (Risø) and L.J. Mahrt (Oregon State University). Last but not least, we wish to express our gratitude to Mr. Gunnar Jensen for his careful compilation and quality control of the data obtained.

REFERENCES

BRADLEY, E.F. (1968). A micrometeorological study of velocity profiles and surface drag in the region modified by a change in surface roughness. Q. J.R. Meteorol. Soc., 94, 361-379.

BUSINGER, J.A. (1973). Turbulent transfer in the atmospheric surface layer. In Workshop on Micrometeorology ed. D.A. Haugen: (American Meteorological Society, Boston 67-100.

GOLDER, D. (1972). Relation among stability parametres in the surface layer. Boundary-Layer Meteorol., 3, 47-58.

HEDEGAARD, K. (1975). Momentum flux and roughness length determined from measurements in the Kattegat. M.Sc.-Thesis, Institute of Meteorology, University of Copenhagen.

HEDEGAARD, K. (1982). "Wind vector and extreme wind statistics in Greenland". Weather Service Report No. 1, Danish Meteorological Institute, Copenhagen, 106 pp.

JACKSON, P.S. and HUNT, J.C.R. (1975). Turbulent wind flow over a low hill. Q. J.R. Meteorol. Soc., 101, 929-955.

JENSEN, N.O. (1978). Change of surface roughness and the planetary boundary layer. Q. J.R. Meteorol. Soc., 104, 351-356.

JENSEN, N.O. and PETERSON, E.W. (1978). On the escarpment profile. Q. J.R. Met. Soc., 104, 719-728.

JUSTUS, C.G., HARGRAVES, W.R. and YALCIN, A. (1976). Nationwide assessment of potential output from wind-powered generators. J. Appl. Meteorol., 15, 673-678.

KITAIGORODSKIY, S.A. (1973). The physics of air-sea interaction. (Israel program for scientific translations, Jerusalem). 237 pp.

LARSEN, S.E. and KRISTENSEN, L. (1980) Radiation errors on temperature measurements. In: Physics Department, Annual progress Report, Risø-R-441, 153-155.

PANOFSKY, H.A. (1973). Tower climatology. In: Workshop on Micrometeorology. ed. D.A. Haugen (American Meteorological Society, Boston) 151-176.

PETERSEN, E.L. (1975). "On the kinetic energy spectrum of atmospheric motions in the planetary boundary layer". Risø-R-285, 104 pp.

PETERSEN, E.L., TROEN, I., FRANDSEN, S., and HEDEGAARD, K. (1981). Windatlas for Denmark. Risø-R-428, 229 pp.

RAO, K.S. (1975). Effect of thermal stratification on the growth of the internal boundary layer. Boundary-Layer Meteorol., 8, 227-234.

RAO, K.S., WYNGAARD, J.C. and COTÉ, O.R. (1974). The structure of the two-dimensional internal boundary layer over a sudden change of surface roughness. J. Atmos. Sci., 31, 738-746.

TAYLOR, P.A. (1969). The planetary boundary layer above a change in surface roughness. J. Atmos. Sci., 26, 432-440.

TENNEKES, H. (1973). Similarity laws and scale relations in planetary boundary layers. In Workshop on Micrometeorology. ed. D.A. Haugen (American Meteorological Society.Boston) 177-216.

WYNGAARD, J.C., COTÈ, O.R. and, RAO, K.S. (1974). Modelling the atmospheric boundary layer. In: Turbulent diffusion in environmental pollu'.ion. Proceedings of a symposium held at Charlottesville, Virginia, April 8-14, 1973. Edited by F.N. Frenkiel and R.E. Munn, (Academic Press, New York) 193-211.

APPENDIX

ANALYSIS OF WIND VECTOR DISTRIBUTIONS

Different authors have shown methods by which directional preference in a wind vector distribution can be detected objectively (see, for example, Petersen (1975)). These methods are convenient tools to determine a wind-speed-independent local influence upon the wind climatology. In this appendix we present a general method for such an analysis.

Local effects that are mainly effective for certain speed intervals are, however, often concealed by this method. When applying the analysis it is therefore recommended to consider the 2-dimensional probability distribution as well in order to detect wind speed-dependent local effects.

A.1. Rotation of the coordinate system

Let $\vec{V}(t)$ be the time-dependent wind vector with magnitude $V(t)$ and direction $\phi(t)$. Its components in the eastward and northward directions are $u(t)$ and $v(t)$. The components in the rotated coordinate system through angle ϕ_o counterclockwise, are $u_r(t)$ and $v_r(t)$ (see Fig. A.1).

The vector components in the rotated coordinate system are given by

$$u_r(t) = u(t)\cos\phi_o + v(t)\sin\phi$$

$$u_r(t) = v(t)\cos\phi_o - u(t)\sin\phi_o \quad ,$$

which, in short, can be expressed by

$$\begin{Bmatrix} u_r(t) \\ v_r(t) \end{Bmatrix} = \begin{bmatrix} \cos\phi_o & \sin\phi_o \\ -\sin\phi_o & \cos\phi_o \end{bmatrix} \begin{Bmatrix} u(t) \\ v(t) \end{Bmatrix} .$$

By moving the origin of the coordinate system to the coordinates (u,v) of the time-averaged wind vector, we see that a similar relation holds for the deviation from the time average, i.e.

$$\begin{Bmatrix} u_r'(t) \\ v_r'(t) \end{Bmatrix} = \begin{bmatrix} \cos\phi_o & \sin\phi_o \\ -\sin\phi_o & \sin\phi_o \end{bmatrix} \begin{Bmatrix} u'(t) \\ v'(t) \end{Bmatrix} ,$$

where the prime denotes deviation from the time average, i.e. $u'(t) \equiv u(t) - \bar{u}$, etc.

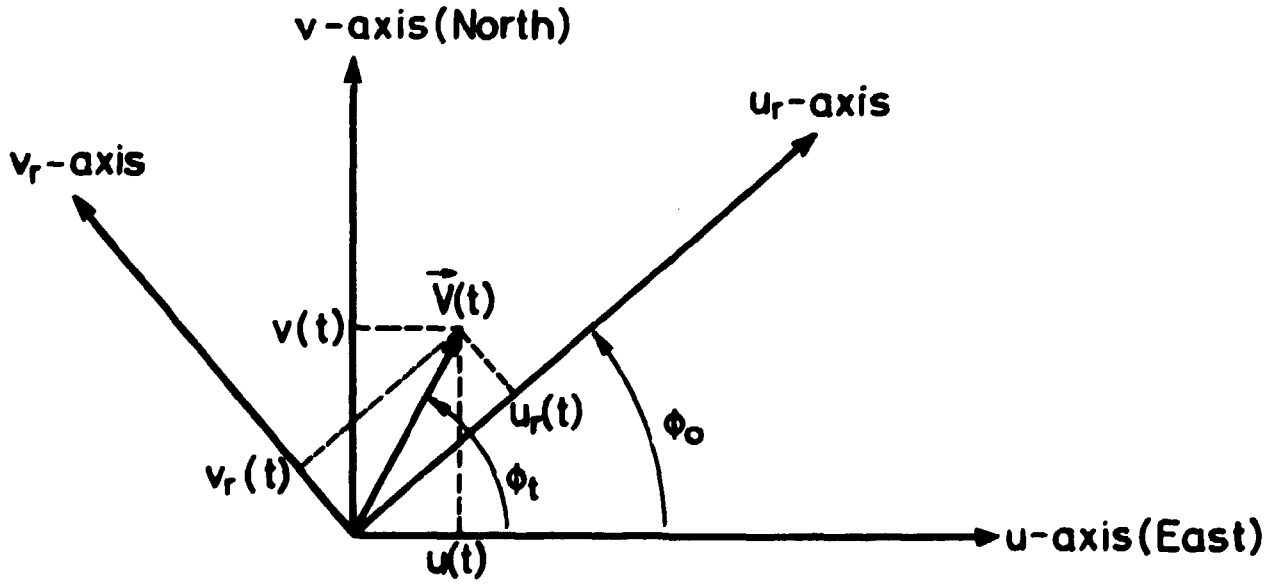

Fig. A.1. The coordinate system rotated the angle ϕ_o counter-clockwise in relation to the basic coordinate system.

For the time-averaged component kinetic energies, $\overline{u_r^2}$ and $\overline{v_r^2}$, and the time-averaged momentum flux $\overline{u_r v_r}$, we get by multiplication and time averaging

$$\overline{u_r^2} = \overline{u^2}\cos^2\phi_o + \overline{v^2}\sin^2\phi_o + \overline{uv}\sin 2\phi_o \qquad \text{(A.1.a)}$$

$$\overline{v_r^2} = \overline{u^2}\sin^2\phi_o + \overline{v^2}\cos^2\phi_o - \overline{uv}\sin 2\phi_o \qquad \text{(A.1.b)}$$

$$\overline{u_r v_r} = \overline{uv}\cos 2\phi_o - \frac{\overline{u^2-v^2}}{2}\sin 2\phi_o \quad . \qquad \text{(A.1.c)}$$

Equivalent expressions are valid for the time-averaged eddy kinetic energies $\overline{u_r'^2}$ and $\overline{v_r'^2}$, and the time-averaged eddy momentum flux, $\overline{u_r'v_r'}$.

By using the identity

$$ab + cd = \frac{a+c}{2}(b+d) + \frac{a-c}{2}(b-d) \ ,$$

and several trigonometric identities, Eqs. A.1 a-c can be rearranged to

$$\overline{u_r^2} = \frac{\overline{u^2+v^2}}{2} + \left[\overline{uv}\sin 2\phi_o + \frac{\overline{u^2-v^2}}{2}\cos 2\phi_o\right]$$

$$\overline{v_r^2} = \frac{\overline{u^2+v^2}}{2} - \left[\overline{uv}\sin 2\phi_o + \frac{\overline{u^2-v^2}}{2}\cos 2\phi_o\right]$$

$$\overline{u_r v_r} = \overline{uv}\sin\left(2\phi_o+\frac{\pi}{2}\right) + \frac{\overline{u^2-v^2}}{2}\cos\left(2\phi_o+\frac{\pi}{2}\right) \ .$$

This can be shortened by use of the identity

$$a\sin\alpha + b\cos\alpha = A\sin(\alpha+\beta) \ ,$$

where

$$A \equiv (a^2+b^2)^{1/2} \text{ and } \beta \equiv \text{Arctan}\left(\frac{b}{a}\right) + \frac{\pi}{2}(1-\text{sign}(a)).$$

Following this we get the expressions for time-averaged kinetic energy and momentum flux in the coordinate system rotated through angle ϕ_o counterclockwise,

$$\overline{u_r^2} = \frac{\overline{u^2+v^2}}{2} + A_t \sin(2\phi_o+\beta_t) \qquad \text{(A.2.a)}$$

$$\overline{v_r^2} = \frac{\overline{u^2+v^2}}{2} - A_t \sin(2\phi_o+\beta_t) \qquad \text{(A.2.b)}$$

$$\overline{u_r v_r} = A_t \sin(2\phi_o+\beta_t+\tfrac{\pi}{2}) \quad , \qquad \text{(A.2.c)}$$

with

$$A_t \equiv \left[(\overline{uv})^2 + \left(\frac{\overline{u^2-v^2}}{2}\right)^2\right]^{1/2} \text{ and}$$

$$\beta_t \equiv \text{Arctan}\left(\frac{\overline{u^2-v^2}}{2\overline{uv}}\right) + \frac{\pi}{2}(1-\text{sign}(\overline{uv})) \quad .$$

Similarly, we get for the time-averaged eddy kinetic energy and eddy momentum flux

$$\overline{u_r'^2} = \frac{\overline{u'^2+v'^2}}{2} + A_e \sin(2\phi_o+\beta_e) \qquad \text{(A.3.a)}$$

$$\overline{v_r'^2} = \frac{\overline{u'^2+v'^2}}{2} - A_e \sin(2\phi_o+\beta_e) \qquad \text{(A.3.b)}$$

$$\overline{u_r'v_r'} = A_e \sin(2\phi_o+\beta_e+\frac{\pi}{2}) \quad , \qquad \text{(A.3.c)}$$

with

$$A_e \equiv \left[\overline{(u'v')^2} + \left(\frac{\overline{u'^2 - v'^2}}{2}\right)^2\right]^{1/2} \quad \text{and}$$

$$\beta_e \equiv \text{Arctan}\left(\frac{\overline{u'^2 - v'^2}}{2\overline{u'v'}}\right) + \frac{\pi}{2}(1 - \text{sign}(\overline{u'v'})) \quad .$$

The kinetic energies in the rotated coordinate system are the sum of a constant part, which is half the total kinetic energy, and a harmonic part in the angle of rotation. The momentum flux is a pure harmonic in this angle.

Equations (A.3.a-c) can be considered from a statistical point of view as well. u' and v' are two variates with zero mean value. By rotating the coordinate axes new variates u_r' and v_r' are formed as linear combinations of u' and v'. From Equations (A.3.a-b) we see that for a certain rotational angle ($\phi_{oe} = \pi/4 - \beta_e/2$), the variance in one component is maximised while that in the other is minimized. The variates in the coordinate system rotated through this angle thus transfer as much as possible of the total variance into one component, and this part of the total variance is the maximum which can be explained by variations in one component.

A.2. Preferred directions

When viewing wind vector distributions we must keep in mind that the physical processes causing a directional preference of the wind vector could be speed dependent. Analysing for preferred directions based on all speeds could therefore conceal the effects of physical processes present only for certain wind speed intervals.

By rotating the coordinate system, we see from Eq. (A.2.a) that there is a rotational angle for which the u_r component contains a maximum of kinetic energy. From Eqs. (A.2.b-c) we find that for this rotation angle $\phi_{ot} = (\pi/4 - \beta_t/2)$, the kinetic energy in the v_r component is at a minimum, and $\overline{u_r v_r} = 0$. This means

that there is no mean momentum flux across the axis determined by ϕ_{ot}. This direction is obviously the preferred one of the wind vector and it is further significant in that it is the axis of zero mean momentum flux.

The degree of directional preference is given by $p_t \equiv A_t/(\overline{u^2}+\overline{v^2})$. The number $(0.5+p_t)$ is the fraction of the total mean kinetic energy that is confined to the u_r direction.

An equivalent analysis can be carried out for the mean eddy kinetic energy $\overline{u_r'^2}$. For rotation angle $\phi_{oe} \equiv (\pi/4 - \beta_e/2)$, $\overline{u_r'^2}$ is at maximum, $\overline{v_r'^2}$ at minimum, and the flux of mean eddy momentum is zero. The amount of directional preference of the eddy wind vector is given by $p_e \equiv A_e/(\overline{u'^2}+\overline{v'^2})$.

The significance of the rotation angle (ϕ_{ot} or ϕ_{oe}) obviously depends upon the degree of preference given by p_t or p_e. On the other hand, a small integral preference does not mean that directional preference is absent for all wind speeds. Different preferences for different speed intervals may cancel in an integral analysis. Analyses of this kind shall therefore be viewed critically, preferably together with the 2-dimensional probability distribution.

Sales distributors:
Jul. Gjellerup, Sølvgade 87,
DK-1307 Copenhagen K, Denmark

Available on exchange from:
Risø Library, Risø National Laboratory,
P.O.Box 49, DK-4000 Roskilde, Denmark

ISBN 87-550-0861-5
ISSN 0106-2840